Quantitative nanoscale imaging of synaptic protein organization

Lara Laparra Cuervo

ICFO – Institut de Ciències Fotòniques

Unversitat Politècnica de Catalunya

Barcelona, 27th March 2018

Quantitative nanoscale imaging of synaptic protein organization

Lara Laparra Cuervo

under the supervision of

Professor Melike Lakadamyali

Unversitat Politècnica de Catalunya

Barcelona, 27th March 2018

Thesis supervisor

Prof. Melike Lakadamyali (Perelman School of Medicine, Pennsylvania, USA)

Thesis Committee members

- Prof. Michael Krieg
  (ICFO – The Institute of Photonics Sciences, Spain)
- Prof. Josep Dalmau
  (IDIBAPS, Spain)
- Dr. Francesca Cella Zanacchi
  (IIT- Italian Institute of Technology, Italy)
- Prof. María García Parajo
  (ICFO – The Institute of Photonics Sciences, Spain)
- Prof. Raúl Estévez Povedano
  (Faculty of Medicine, IDIBELL- Universitat de Barcelona, Spain)

An Claudia, meine Lebenspartnerin i a la Nolis, ma mare, els dos pilars en aquesta tesi

Acknowledgements

My gratitude for the accomplishment of this thesis goes to the uncountable number of people who crossed my life path. It is due to their small contribution that now I have reached this point.

I would like to start thanking the people with whom I have shared all these years at work, my lab colleagues. Despite the current spread all over the world of our group, I still feel connected to them in a particular way.

I still remember the first day I came to this group. I crossed a woman on the stairs who, without knowing it, was going to be my mentor for the following years. Nela introduced me to the basic research world. She was extremely kind and patient to show me all the insights of the lab and the imaging setup. When I think back, I cannot imagine how unexperienced and naive I was. I shared with Nela not only professional knowledge but also personal stories, which made the uncountable long days in the darkness more feasible. I also would like to especially thank the other lab members who had tones of patience to introduce me to the neuro world, the neurodudes! Laurent and Jesús showed me the wonders and the disappointments to work with neurons. Despite their complexity, I sort of developed a certain respect for this kind of cells and I learned incredibly interesting things, not necessarily related to my work, about them thanks to the neuro people.

Of course, I could not forget Joe and Angel, who were of extreme help in my project for the software and the sample preparation respectively, and the roomies in my office. Ana, Jason and also Johnny before, together with Nela and Laurent have made my days, especially before going home, where the creative part of our brains was in effervescence. They kindly helped me with my stupid questions and also a big thank you for always being there when I was under stress.

. Finally, I would like to thank all the other members, Stefan, Ione, Guillaume, Nitin, Maury, Fra, Shreya and all the rest that stayed a short period but also added their grain in this whole story for their important discussions and support.

A special thank goes to my supervisor, Melike Lakadamyali. She believed in me and showed me how impressive this research world can be. She also showed me how rewarding can persistence and hard work be and how to hold on when it is not. I will keep this lessons in the future, not only in the professional career.

Zooming out a bit, there is a lot of people that were not from my group but also played an important role. I would like to thank the Single Molecule Biophotonics group at ICFO for their meaningful discussions and confessions and sweets and cakes. Being so close to each other felt like following a parallel path. I also met incredible people with whom I shared a lot of experiences, like my former Erasmus Mundus Master colleagues, especially thank you to Gabi, for sharing hours and hours of chatting and advice. We all started together and we more or less have come to an end together. And many other icfonians that will always be part of my enjoyable memories from my time at ICFO.

Ja fora d'ICFO també he d'agrair a una multitud de gent que han participat en la seva manera en tot aquest temps que ha durat la tesi. Vull començar agraint a les "drugas", les inseparables companyes de la uni, Gemma, Ana, Cristina, Maria i Paula, pel el seu suport i consells. Malgrat la distancia, tenir vides paral·leles fa que sigui més fàcil trobar punts en comú. Elles m'han mostrat que és possible acabar el doctorat i també que hi ha vida més enllà. També a la resta dels "machos", Sergio, Cristian, Albert i especialment a la Cristina, per treure'm diversos vespres de l'enclaustrament quan portava dies sense sortir de casa escrivint aquesta tesi. També vull donar les gràcies a n'Alba. Tot i estar

lluny sempre hi és present. Aquest any serà un any molt important per a totes dues!

Finalment, aquesta tesi no hauria estat possible sense l'ajuda incondicional de la meva família. Vull donar les més caloroses gràcies a la meva àvia Gene. Ella em recorda tot que ha fet possible que jo hagi arribat a aquest punt de la meva carrera. També donar les gràcies a mon pare Toni i l'Alícia, per ser un suport fonamental, als meus germans Carles i Pablo, a la Susana i al membre més nou de la família, en Phuc, per ser un cop d'aire fresc aquests últims mesos tan esgotadors. I també a la Cookie i a la Snow, per la seva companyia durant tot aquest temps.

Una menció especial ha d'anar a les dues persones que més bé em coneixen i que no tinc prous paraules per mostrar-los el meu agraïment. A la Nolis, ma mare, per estar sempre a punt per a qualsevol cosa, sé que sempre puc comptar amb tu! I a la Claudia, meine Lebenspartnerin, por haber aguantado, por apoyarme, por soportarme, por animarme, por hacerme reír y por querer seguir compartiendo tantas y tantas experiencias. Aun siendo un año complicado para las dos, ¡lo hemos conseguido! Vielen, vielen Dank!

To all this people and everyone else I have forgotten, all my most sincere gratefulness.

Table of Contents

Abstract

Fluorescence microscopy has evolved immensely in the last decade. The arrival of super-resolution techniques has driven researchers to explore biological areas that were unreachable before. Such techniques not only allowed the improvement of spatial resolution in images but also the possibility to perform quantitative measurements at the single-molecule level. The interest in that particular field has been growing over the years and new and more sophisticated tools have been developed.

Neuroscience has been a traditionally technology driven field, with methods such as patch clamp and 2-photon microscopy revolutionizing our understanding of how the cells of the brain functions. It is therefore no surprise that neuroscience has been one of the first fields to adapt and benefit from super-resolution microscopy. These techniques opened a new window of opportunity to reveal spatial organization of the neuronal cytoskeleton and the molecular organization and dynamics of the synapse, structures below the spatial resolution limit of conventional light microscopy.

Protein organization and stoichiometry is central for synaptic transmission in neurons. Knowing the absolute numbers of proteins playing a key role in diseases can be of extreme interest in order to understand the mechanisms that lead to such neurological disorders.

In this thesis we exploited the super-resolution techniques to develop a pioneering method for quantitative single-molecule measurements and to unravel the organization of a synaptic protein complex that was never visualized before with nanoscale spatial resolution.

Chapter 1 puts in context the field of neuroscience at the nanoscale level. The main parts of the neurons are introduced and the importance of knowing the molecular stoichiometry in synaptic protein complexes is explained. In Chapter 2, the super-resolution fluorescence microscopy techniques are described, emphasizing their most relevant characteristics. Additionally, different examples of these techniques implemented in neurons are explained. Some of the methods used in this thesis have been adapted from these examples.

Chapter 3 shows a novel method that we developed in order to quantify the photoactivation efficiency of different photoswitchable fluorescent proteins commonly used in super-resolution experiments, such as PALM. We used the glycine receptor as a template because of its well-known stoichiometry. Taking advantage of this model, we tagged eight different photoswitchable fluorescent proteins (mEos2, 3.1 and 3.2, Dendra2, mClavGR2, mMaple, PA-GFP and PA-mCherry) to the α- and β-subunits of the glycine receptor and transiently transfected them to *Xenopus* oocytes. The fact that the fluorescent proteins are genetically encoded make them highly suitable for quantitative single-molecule counting. The photoactivation efficiency, which is the percentage of a fluorescent protein that photoactivates into a fluorescently detectable form, plays a critical role in properly interpreting quantitative measurements.

Chapter 4 is focused on super-resolution imaging of a synaptic protein complex, called LGI1 complex. This ensemble of proteins is one of the main key players involved in different neurological disorders. Leucine rich glioma activated 1 (LGI1) is a neuronal protein that forms a trans-synaptic bridge linking pre- and postsynaptic transmembrane proteins (ADAM22 and ADAM23) and helps to organize a multimeric complex at the synapse including AMPA receptors and voltage-gated potassium channels (VGKC). LGI1

autoimmune encephalitis is a severe neuropsychiatric disorder related to epilepsy where the patients produce autoantibodies against LGI1, which alter synaptic plasticity. However, the molecular mechanisms that lead to the observed problems in patients still remain largely unknown.

Using well-characterized synaptic markers (Homer and Bassoon) as molecular standards, we determined the positioning of LGI1 and the other related proteins within the synaptic space at nanoscale resolution by means of multi-color STORM. Further, the comparison of this molecular architecture in healthy neurons versus neurons treated with antibodies from patients suffering from LGI1 autoimmune encephalitis showed that LGI1 autoantibodies impact the nanoscale organization of pre-synaptic proteins. These results suggested a loss of LGI1 interaction with pre-synaptic proteins upon antibody binding and gave further insight into early changes in pathology.

Chapter 5 summarizes all the results achieved in this thesis and gives an insight to possible future directions in order to complement the achieved results or provide new ideas to solve the new open questions derived from our results.

Resumen

La microscopía de fluorescencia ha evolucionado enormemente en la última década. La llegada de las técnicas de super-resolución ha llevado a los investigadores a explorar áreas de biología, anteriormente inalcanzables. Estas técnicas han permitido no solo mejorar la resolución espacial en imágenes sino que también la posibilidad de realizar medidas cuantitativas al nivel de una sola molécula. El interés en este campo ha ido creciendo a lo largo de los años y se han desarrollado nuevas técnicas, cada vez más sofisticadas.

La neurociencia ha sido un campo tradicionalmente dirigido por las nuevas tecnologías, con métodos como técnica de fijación de membranas y la microscopía de excitación de dos fotones que han revolucionado nuestro entendimiento de cómo funcionan las células del cerebro. Por ello, no es sorprendente que la neurociencia haya sido uno de los primeros campos en adaptarse y beneficiarse de la microscopía de super-resolución. Estas técnicas han abierto una nueva ventana de oportunidades para revelar la organización espacial en el cito esqueleto neuronal y la organización molecular y dinámica de la sinapsis, ambas estructuras por debajo del límite de resolución espacial de la microscopía de luz convencional.

La organización de las proteínas y su estequiometria es clave para la transmisión sináptica en neuronas. El conocimiento de los números absolutos de proteínas que juegan un papel crucial en enfermedades puede ser de enorme interés para entender los mecanismos que llevan a tales disfunciones neurológicas.

En esta tesis hemos explotado las técnicas de super-resolución para desarrollar un método pionero para medidas cuantitativas de una sola molécula y para desvelar la organización de un complejo de proteínas

sinápticas que no se había visualizado hasta la fecha con resolución espacial a nanoescala.

El capítulo 1 pone en contexto el campo de la neurociencia al nivel nanométrico. Se introducen las partes principales de las neuronas y se explica la importancia de conocer la estequiometría molecular en complejos proteínicos sinápticos. En el capítulo 2 se describen las técnicas de microscopía de fluorescencia en super-resolución, enfatizando sus características más relevantes. Adicionalmente, se explican diferentes ejemplos de estas técnicas implementadas en neuronas. Adaptaciones de estos ejemplos son algunos de los métodos usados en esta tesis.

El capítulo 3 muestra un método novedoso que hemos desarrollado para cuantificar la eficiencia de fotoactivación de diferentes proteínas fluorescentes fotoconmutables, usadas de manera común en los experimentos de super-resolución como PALM. Usamos el receptor de glicina como modelo por su conocida estequiometria. Aprovechando este modelo, etiquetamos ocho proteínas fluorescentes fotoconmutables (mEos2, 3.1 y 3.2, Dendra2, mClavGR2, mMaple, PA-GFP y PA-mCherry) a las subunidades α y β del receptor de glicina y las transfectamos a ovocitos de *Xenopus*. El hecho que las proteínas fluorescentes están codificadas genéticamente las hace especialmente adecuadas para cuantificar proteínas individualmente. La eficiencia de fotoactivación, es decir, el porcentaje de una proteína fluorescente que se fotoactiva a una forma fluorescente detectable juega un papel crucial para una correcta interpretación de medidas cuantitativas.

El capítulo 4 está centrado en la obtención de imágenes en super-resolución de un complejo proteínico sináptico, llamado complejo de LGI1. Este conjunto de proteínas es uno de los actores principales involucrados en ciertos trastornos neuronales. Leucine rich glioma activated 1 (LGI1) es una proteína neuronal que forma un puente trans-sináptico uniendo proteínas de

membrana pre- y post-sinápticas (ADAM22 y ADAM23) y ayuda en la organización de un complejo multimérico en la sinapsis que incluye receptores AMPA y canales de potasio dependientes del voltaje (VGKC). La encefalitis autoinmune de LGI1 es un severo trastorno neurosiquiátrico relacionado con epilepsia en que los pacientes producen anticuerpos contra LGI1, alterando la plasticidad sináptica. Sin embargo, los mecanismos moleculares que desembocan a los problemas observados en pacientes aún son bastante desconocidos.

Usando marcadores sinápticos que han sido altamente caracterizados (Homer y Bassoon) como estándares moleculares, hemos determinado la posición de LGI1 y las otras proteínas relacionadas en el espacio sináptico en resolución a nanoescala gracias al uso de la técnica de STORM en multi-color. Además, la comparación de esta arquitectura molecular en neuronas sanas y neuronas tratadas con anticuerpos de pacientes con encefalitis autoinmune de LGI1 mostró que dichos anticuerpos causan un impacto en la organización de las proteínas pre-sinápticas. Estos resultados sugieren una pérdida de la interacción de LGI1 con proteínas pre-sinápticas a causa de los anticuerpos enlazados y dan una visión más clara en los primeros cambios en la patología.

El capítulo 5 resume todos los resultados logrados en esta tesis y muestra una visión de las direcciones futuras posibles para complementar los resultados conseguidos o proporcionar ideas nuevas para resolver las nuevas cuestiones derivadas de nuestros resultados.

Resum

La microscòpia de fluorescència ha evolucionat enormement en l'última dècada. L'arribada de les tècniques de super-resolució ha portat als investigadors a explorar àrees de la biologia que eren inabastables anteriorment. Aquestes tècniques han permès no només millorar la resolució espacial en imatges sinó també la possibilitat de realitzar mesures quantitatives al nivell d'una sola molècula. L'interès en aquest camp ha anat creixent al llarg dels anys i s'han desenvolupat noves tècniques, cada cop més sofisticades.

La neurociència ha sigut un camp tradicionalment dirigit per les noves tecnologies, amb mètodes com la tècnica de la fixació de membranes i la microscòpia d'excitació de dos fotons que han revolucionat la nostra manera d'entendre el funcionament de les cèl·lules del cervell. Per això, no es sorprenent que la neurociència hagi sigut un dels primers camps en adaptar-se i beneficiar-se de la microscòpia de super-resolució. Aquestes tècniques han obert una nova finestra d'oportunitats per a revelar l'organització espacial al citoesquelet neuronal i l'organització molecular i dinàmica de la sinapsi. Totes dues estructures estan per sota del límit de resolució espacial de la microscòpia de llum convencional.

L'organització de les proteïnes i la seva estequiometria son clau per a la transmissió sinàptica en neurones. El coneixement dels nombres absoluts de proteïnes que juguen un paper crucial en malalties pot tenir un interès enorme per a entendre els mecanismes que porten a disfuncions neurològiques.

En aquesta tesi hem explotat les tècniques de super-resolució per a desenvolupar un mètode pioner per a mesures quantitatives d'una sola

molècula i per a revelar l'organització d'un complex de proteïnes sinàptiques que no s'havia visualitzat fins llavors amb resolució espacial a nanoescala.

El capítol 1 posa en context el camp de la neurociència al nivell nanomètric. S'introdueixen les parts principals de les neurones i s'explica la importància de conèixer l'estequiometria molecular en complexes proteínics sinàptics. Al capítol 2 es descriuen les tècniques de microscòpia de fluorescència en super-resolució, emfatitzant les seves característiques més rellevants. Addicionalment, s'expliquen diferents exemples d'aquestes tècniques implementades en neurones. Adaptacions d'aquests exemples són alguns dels mètodes emprats en aquesta tesi.

El capítol 3 mostra un mètode nou que hem desenvolupat per a quantificar l'eficiència de fotoactivació de diferents proteïnes fluorescents fotocommutables, utilitzades de forma habitual als experiments de super-resolució com PALM. Vam utilitzar el receptor de glicina com a model per la seva estequiometria ja coneguda. Aprofitant aquest model, vam etiquetar vuit proteïnes fluorescents fotocommutables (mEos2, 3.1 i 3.2, mclavGR2, mMaple, PA-GFP i PA-mCherry) a les subunitats α i β del receptor de glicina i les vam transfectar a oòcits de *Xenopus*. El fet que les proteïnes fluorescents estiguin codificades genèticament les fa especialment adequades per a quantificar proteïnes individualment. L'eficiència de fotoactivació, és a dir, el percentatge que una proteïna fluorescent es fotoactivi a una forma fluorescent detectable, juga un paper crucial per a la correcta interpretació de mesures quantitatives.

El capítol 4 està centrat en l'obtenció d'imatges en super-resolució d'un complex proteínic sinàptic, anomenat complex de LGI1. Aquest conjunt de proteïnes és un dels actors principals involucrats en certs trastorns neuronals. Leucine rich glioma activated 1 (LGI1) és una proteïna neuronal que forma un pont trans-sinàptic unint proteïnes de membrana pre- i post-sinàptiques

(ADAM22 i ADAM23) i ajuda en l'organització d'un complex multimèric en la sinapsi que inclou receptors AMPA i canals de potassi dependents del voltatge (VGKC). L'encefalitis autoimmune de LGI1 es un trastorn neuropsiquiàtric sever re relacionat amb epilèpsia en que els pacients produeixen anticossos contra LGI1, alterant la plasticitat sinàptica. Tanmateix, els mecanismes moleculars que desemboquen als problemes observats en pacients encara són bastant desconeguts.

Fent servir marcadors sinàptics que han estat altament caracteritzats (Homer i Bassoon) com estàndards moleculars, hem determinat la posició de LGI1 i les altres proteïnes relacionades a l'espai sinàptic en resolució a nanoescala gràcies a la tècnica de STORM en multi-color. A més, la comparació d'aquesta arquitectura molecular en neurones sanes i neurones tractades amb anticossos de pacients amb encefalitis autoimmune de LGI1 va mostrar que aquests anticossos causen un impacte en l'organització de les proteïnes presinàptiques. Aquests resultats suggereixen una pèrdua de la interacció de LGI1 amb proteïnes presinàptiques a causa dels anticossos enllaçats i donen una visió més clara en els primers canvis en la patologia.

El capítol 5 resumeix tots els resultats assolits en aquesta tesi i mostra una visió de les direccions futures possibles per a complementar els resultats aconseguits o proporcionar idees noves per a resoldre les noves qüestions derivades dels resultats.

Chapter 1

Introduction to neuroscience

The field of neuroscience has evolved exponentially since the original neuroanatomical works performed by the Nobel laureate Santiago Ramón y Cajal in the late 19th century. Understanding the functioning of the brain has been defined as one of the key challenges of modern science. Neuroscience has heavily relied on the advent of new technologies from patch clamp to two photon microscopy to study the molecular, cellular, developmental, structural, functional and clinical aspects of the nervous system. Fluorescence microscopy has particularly played an important role in advancing our understanding of how the brain works at multiple levels ranging from the molecular to the tissue level. The main focus of this thesis is the application of the novel super-resolution techniques to visualize the organization of synaptic protein complexes at the nanoscale level.

1.1. Introduction to neuronal transmission

The nervous system of all animals in composed by an ensemble of nerve cells called neurons. Ramón y Cajal was the first one to discover the neuron doctrine and demonstrate that the nervous system is not a continuous tissue but is formed by individual set of interconnected neurons. The essential role of neurons is to transfer information encoded in electrical signals to other neurons. Neurons have unique morphologies compared to other cell types in which dendritic and axonal processes extend out from the cell soma (Cajal, 1899). The information is transmitted down the axon by means of an electric wave of membrane depolarization called action potential and transmitted to other neurons via synaptic connections between axons and dendrites (Alberts et al., 2008).

Neuronal transmission is fundamental to the correct functioning of the brain. The average neuron forms about 1 000 synaptic connections and can receive as many as 10 000 connections. Synapses are thus the key functional units of neurons. Synapses are densely populated by many different proteins whose principal role is the regulation of the synaptic transmission. It has been estimated that human brain can contain up to 10^{11} neurons and 10^{14} synaptic connections (Kandel et al., 2000). In the next section we describe more in detail these principal actors of the signal transmission.

1.2. Neurons and synapses

Schematically, neurons consist of three differentiated parts: the dendrites, where the information is received, the soma or cell body, where the nucleus and the central machinery of the cell are found, and the axon, where the signal is transmitted through synapses in the axon terminals (**Figure 1.1**).

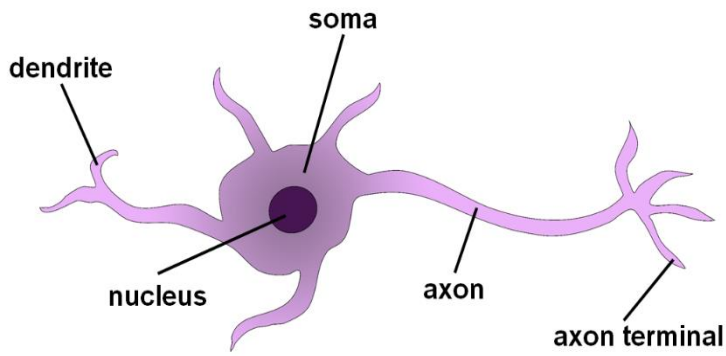

Figure 1.1. Scheme of a single neuron. *They consist of three main parts. The soma is where the nucleus is and the main inner cell functions take place. The dendrites are typically short ramifications that extend from the soma to other neurons. They become thinner with each branching and extend their farthest branches a few hundred micrometers from the soma. The axon can have a very wide range of extension, from few millimeters to the order of a meter. At the end, it also branches, but usually maintaining the same diameter.*

The synapse is composed of the presynaptic terminal in the axon, the postsynaptic side in the dendrite and a nanometric gap in between called the synaptic cleft (**Figure 1.2** - inset). The pre-synapse contains a high density of synaptic vesicle in an area called the presynaptic active zone (PAZ) and the synaptic vesicles are filled with neurotransmitter molecules. When an action potential is conducted through the axon and reaches its terminal, a depolarization of the membrane is produced, which leads to the fusion of synaptic vesicles with the membrane and the neurotransmitter is released into the synaptic cleft (Jin and Garner, 2008, Schoch and Gundelfinger, 2006). The transmitter diffuses rapidly across the synaptic cleft, binds to a receptor in the postsynaptic site and triggers a conformational change that opens or closes the ion channel, which creates a reproducible postsynaptic current (**Figure 1.2** - inset). Typically, a single axon branches at its far end, passing on its message to many target cells simultaneously.

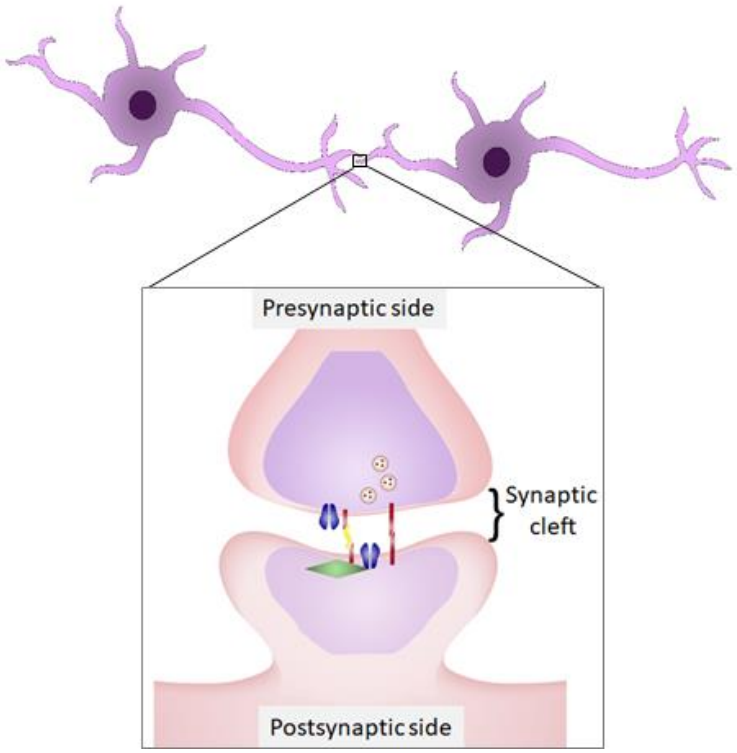

Figure 1.2. Scheme of a synapse. *The axon terminal of a neuron connects with a dendrite of another neuron forming a synapse. In this synapse, the presynaptic side is responsible for the release of neurotransmitters that travel through the synaptic cleft and are bound to receptors in the membrane of the postsynaptic side. This synaptic cleft is a nanometric gap whose size is typically between 20-50 nm (Zuber et al., 2005).*

Based on the type of neuronal receptors they contain and the nature of the signal, chemical synapses can be classified into excitatory and inhibitory. Whether the synaptic potential has an excitatory or inhibitory effect does not depend on the particular neurotransmitter release, but on the type of receptors present in the postsynaptic cell. The same transmitter can have different effects depending on the type of receptors present. When the release of neurotransmitters causes a depolarization on the postsynaptic membrane, the synapse is excitatory. However, if a hyperpolarization occurs instead, it is considered an inhibitory synapse (Kandel et al., 2000).

Excitatory synapses

In excitatory synapses, the arrival of action potentials produces a depolarization of the membrane that enhances the cell's ability to generate another action potential. When the electrical signal reaches the terminal of the axon, excitatory neurotransmitters such as acetylcholine, glutamate or serotonin are released through fusion of vesicles containing these neurotransmitters with the presynaptic membrane. In the postsynaptic membrane receptors open and induce influx of Na^+ or Ca^{2+} into the cell. Since the membrane is disbalanced towards negative charges, a subsequent influx of cations depolarizes the postsynaptic membrane, causing firing of an action potential.

The most abundant excitatory synapses are the glutamatergic synapses and are very enriched in the cortex and the hippocampus. We used the latter as a model for our experiments, as explained later in this thesis. The main receptors of these synapses are NMDA receptor (NMDAR) (The *N*-methyl-D-aspartate receptor) and AMPA receptor (AMPAR) (α-amino-3-hydroxy-5-methyl-4-isoxazolepropionic acid receptor). NMDARs and AMPARs belong to the group of glutamate receptors with crucial roles in memory, learning and synaptic plasticity. When a postsynaptic neuron is stimulated repeatedly, the AMPARs generates a powerful synaptic potential that depolarizes the cell membrane. Then, NMDARs open, allowing calcium to flow into the cell (Kandel, 2007).

In the postsynaptic side, a dense ensemble of scaffolding proteins anchors membrane receptors as well as various signaling molecules that relay the neurotransmitter signals (Okabe, 2007, Sheng and Hoogenraad, 2007). This scaffolding protein ensemble is called postsynaptic density (PSD) and is responsible for synaptic transmission, signal transduction and processing and

it provides a substrate for synaptic plasticity (Alberts et al., 2008, Nägerl and Triller, 2016).

Inhibitory synapses

At inhibitory synapses incoming action potentials produce a hyperpolarization of the postsynaptic membrane. Inhibitory neurotransmitters in dendrites, such as γ-aminobutyric acid (GABA) or glycine, are released, creating an opening of Cl^- or K^+ channels in the postsynaptic side. The opening of K^+ channels makes it harder to drive the cell away from the resting state. The influx of Cl^- produces an increase of the negative charges in the membrane, which in turn makes it more difficult for the cell to be depolarized and excited (Kandel et al., 2000, Alberts et al., 2008).

The most common receptors in inhibitory synapses are GABA and glycine receptors, which have an important role in the regulation of the central nervous system (CNS). Although postsynaptic scaffold proteins, such as gephyrin, are present at in inhibitory synapses, the postsynaptic side does not contain a large macromolecular machine of the PSD.

Overall, neuronal transmission is in fact a result of a very meticulous organization of synaptic proteins performing different roles, such as presynaptic vesicle fusion, scaffolding or structural stabilization. Synapse formation and maturation require multiple interactions between presynaptic and postsynaptic neurons that are mediated by a diverse set of synaptic proteins (Han and Kim, 2008, McMahon and Díaz, 2011, Siddiqui and Craig, 2011). Initial synapse formation needs both the binding of secreted proteins to presynaptic and postsynaptic receptors, and the direct binding between presynaptic and postsynaptic transmembrane proteins.

In addition to the major protein components described above, proteomic and genomic studies have suggested that hundreds of other protein species are localized in synapses (Collins et al., 2006, Fernández et al., 2009). The major components of the synapse are described in more detail the following section.

1.3. Synaptic proteins

The plasma membrane of all cells, including nerve cells, is about 6-8 nm thick and consists of a mosaic of lipids and proteins. Embedded within the continuous lipid sheet are integral membrane proteins, including ion channels, which are the essential proteins for signal transmission in the synapse. In order to enable stable signaling, synapses also contain other important proteins that allow the stabilization of the synaptic transmission. These proteins are structural proteins such as scaffolding proteins, adhesion proteins and secreted proteins (**Figure 1.3**).

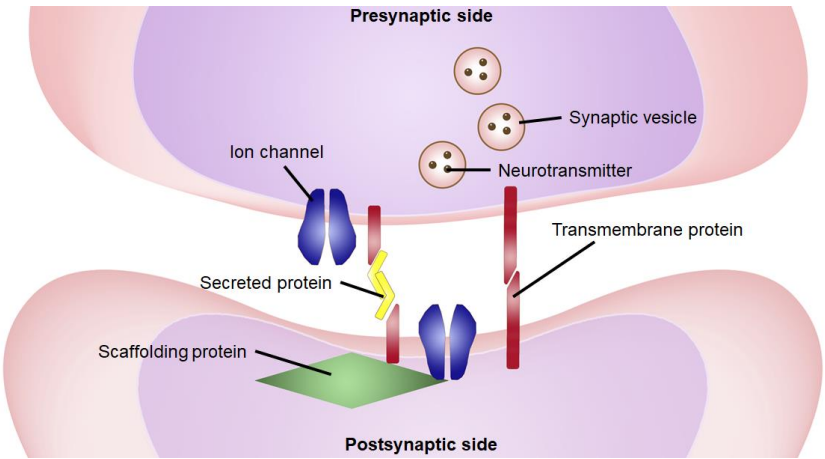

Figure 1.3. Synaptic proteins. *The synapse is a highly dense structure responsible for the neuronal transmission. The main players of this structure are ion channels (blue) that allow the transport of ions in and out of the cell. The transmembrane proteins (red), also present in both synaptic sides, give stabilization to the synaptic cleft, either interconnecting from one side to the other or with the help of secreted proteins (yellow) that bind and create a bridge between them. The scaffolding proteins (green) create a platform below the membrane to stabilize the ion channels and the transmembrane proteins.*

1.3.1 Ion channels and receptors

These proteins are among the most important ones for synaptic transmission. They differ from one another in their ion selectivity and in the factors that control their opening, closing or gating. The most relevant ones are the ligand-gated ion channels and voltage-gated ion channels.

Ligand-gated ion channels

These channels are also neuroreceptors with highly selective binding sites for neurotransmitters released from the presynaptic side. Their stabilization at the synapse is transient. However, when bound to synaptic scaffolds, these receptors are relatively immobile. In extra-synaptic regions they undergo fast diffusion and can diffuse in and out of the synapse at high rates.

The ion channels that open directly in response to the acetylcholine, serotonin, GABA and glycine contain subunits that are structurally similar and probably form transmembrane pores in the same way, even though they have distinct neurotransmitter-binding specificities and ion selectivity. These channels are all built from homologous polypeptide subunits, which assemble into pentamers (**Figure 1.4** – left). Glutamate-gated ion channels are an exception, in that they are constructed from a distinct family of subunits and form tetramers resembling to K^+ channels (Kandel, 2007) (**Figure 1.4** – right).
The stoichiometry of these ion channels is central to understand the different cellular mechanisms in which these channels are involved. In the first part of this thesis, we developed a strategy to account for protein counting error due to inefficiency of photoconversion in photoswitchable fluorescent proteins. Particularly, we made use of the Glycine receptor, whose stoichiometry is well known, as a model to characterize a set of fluorescent proteins used in PALM

experiments to be able to perform future quantitative measurements in cellular proteins.

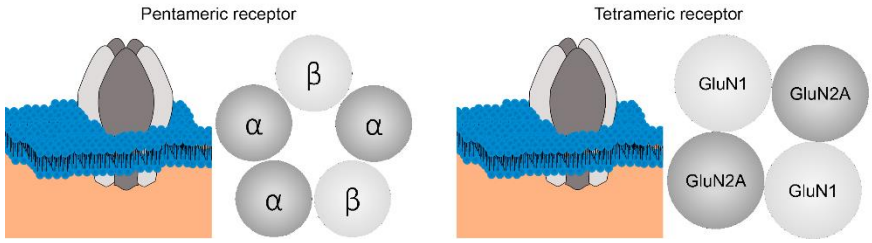

Figure 1.4. Stoichiometry of receptors. *Pentameric receptors, like the Glycine receptor (left), have a conformation of five equal subunits (homomeric) or a subset of different subunits (heteromeric). Glycine heteromeric receptors contain 3 α subunits and 2 β subunits. In the case of the tetrameric receptors, such as NMDAR (right), they can also contain a subset of different subunits. NMDA is composed by 2 GluN1 subunits on one half and GluN2A or 2B or a mixture of both on the other half.*

Voltage-gated ion channels

Voltage-gated channels are regulated by changes in voltage, not by neurotransmitters. For these ion channels the rates of signal transmission are steeply dependent on membrane potential. They generate action potentials that carry information within neurons. When an incoming action potential arrives to the presynaptic membrane of an excitatory synapse, they open allowing calcium ions to come into the cell. These ions trigger the neurotransmitter release. Therefore, voltage-gated ion channels are responsible for transforming electrical signals into chemical signals (Kandel et al., 2000, Kandel, 2007).

1.3.2 Scaffolding proteins

In the synaptic membrane, receptors interact with an underlying meshwork of scaffolding proteins that provide receptor binding sites and immobilize the receptors at the PSD (**Figure 1.3**). The adaptor protein PSD-95 forms the core of the scaffold at the PSD in excitatory synapses and it is critical for glutamate

receptor stabilization (Renner et al., 2008), while gephyrin is one of the main scaffolding proteins in the inhibitory synapses (Giesemann et al., 2003).
Two synaptic proteins that are part of this group have been used multiple times as a reference for localizing the presynaptic side and the postsynaptic side in fluorescent images: Bassoon, located mainly in the axon and Homer, located mainly in the dendritic spines. These proteins have been used in this thesis as reference proteins to position the synapses in our fluorescence images.

1.3.3 Adhesion and secreted proteins

Scaffolding proteins are responsible for the stability of the postsynaptic density, thus intracellular stability. However, in order to have stability through the synaptic cleft, it is crucial to have protein complexes that create a bridge between neurons, binding the presynaptic side with the postsynaptic side (intercellular stability). In this group, there are transmembrane proteins that act as adhesion proteins with the help of secreted proteins (**Figure 1.3**).

In our case, we focus our attention to the ADAMs family, a group of transmembrane proteins that impact cell adhesion, migration, proteolysis and signaling (Edwards et al., 2008). Together with a secreted protein called LGI1, ADAM22 and ADAM23 are the core proteins of an important trans-synaptic protein complex that we called LGI1 protein complex, studied in detail in Chapter 4.

The study of LGI family of proteins is critical for understanding proper development and function of the vertebrate nervous system, and for gaining insights into therapies for diseases that affect them (Kegel et al., 2013). LGI1, together with integrins (Chavis and Westbrook, 2001), seems to be crucial to the synchronous maturation of pre- and postsynaptic membrane functions of

glutamatergic synapses during postnatal development. LGI1 binds to disintegrin, one of the domains of ADAM proteins (Fukata et al., 2006, Yang et al., 2006) and also indirectly binds the Kv1.1 subunit of voltage-gated potassium channels (VGKC) whose major role is the modulation of synaptic transmission in neurons of the CNS (Schulte et al., 2006). LGI1 protein expression was reported to reduce the VGKC subunit Kv1.1 inactivation via the intracellular β-subunit of the channel (Schulte et al., 2006).

This thesis has been focused on studying in detail the molecular organization of LGI1 complex.

1.4 Importance of organization and stoichiometry in synaptic proteins

The organization of proteins within the synapse is crucial for physiological function, motivating continuing study of synaptic morphology. The precise number, distribution, and activity of synaptic proteins determine the efficacy of the synapse as a signaling device. A disruption of proper molecular organization can lead to problems with synaptic transmission. Many neurological disorders are a consequence of structural, biochemical or electrical abnormalities in the nervous system. These disorders can cause several symptoms such as epilepsy, seizures, memory loss, hallucinations, etc. and even in some cases death. Knowledge of the organization and the stoichiometry of these proteins at the nanoscale level can lead us to understand the machinery that regulates synaptic transmission and may help neuroscientists to understand the triggering mechanisms that lead to such severe neurological disorders.

One emerging theory suggests that individual neurons are self-tuning devices, constantly adjusting the expression of proteins in synapses in order to maintain a stable function. This plasticity in nerve cells is crucial to memory

and other higher brain functions. It is thus important to study the stoichiometry of synaptic proteins at two different levels: at the individual protein level, for example measuring the ratio between subunits in an ion channel, and at the structural level, i.e. counting the ratio of the different proteins within a protein complex (Alberts et al., 2008).

Since the proteins are nanostructures, visualization of the synaptic proteins with conventional imaging methods does not provide information about protein organization or stoichiometry. The first precise image of a synapse was performed in parallel in two different labs using electron microscopy (De Robertis and Bennett, 1955, Palay and Palade, 1955). In these images, the structure of vesicles was revealed and one year after, the same lab found that these vesicles contained particles called neurotransmitter (Palay, 1956). Together with electrophysiological recordings of unitary postsynaptic voltage changes (Fatt and Katz, 1951, del Castillo and Katz, 1954), these studies set a basis on the mechanisms of synaptic transmission. However, electron microscopy has important drawbacks regarding the imaging of multiprotein structures. The poor antibody efficiency and low contrast at the molecular level of electron microscopy makes the imaging of molecular structures highly challenging. In order to unveil a detailed multi-molecular organization in synapses, it is necessary to combine different techniques such as electrophysiology, immunoprecipitation, cell and animal based assays, etc. together with other imaging techniques, such as fluorescence super-resolution techniques. In particular, a complete understanding of neuronal functions requires observation of the synapse with high spatial and temporal resolution. In this thesis, we employ super-resolution microscopy to break the diffraction limit and visualize synaptic organization with high spatial resolution.

References

Alberts, B., Wilson, J. and Hunt, T. (2008) *Molecular biology of the cell.* New York: Garland Science.

Cajal, S. R. (1899) *Textura del sistema nervioso del hombre y de los vertebrados: estudios sobre el plan estructural y composición histológica de los centros nerviosos adicionados de consideraciones fisiológicas fundadas en los nuevos descubrimientos. Textura del sistema nervioso del hombre y de los vertebrados*: Instituto de neurociencias, 1992.

Chavis, P. and Westbrook, G. (2001) 'Integrins mediate functional pre- and postsynaptic maturation at a hippocampal synapse', *Nature,* 411(6835), pp. 317-21.

Collins, M. O., Husi, H., Yu, L., Brandon, J. M., Anderson, C. N. G., Blackstock, W. P., Choudhary, J. S. and Grant, S. G. N. (2006) 'Molecular characterization and comparison of the components and multiprotein complexes in the postsynaptic proteome', *Journal of Neurochemistry,* 97, pp. 16-23.

De Robertis, E. D. P. and Bennett, H. S. (1955) 'SOME FEATURES OF THE SUBMICROSCOPIC MORPHOLOGY OF SYNAPSES IN FROG AND EARTHWORM', *The Journal of Biophysical and Biochemical Cytology,* 1(1), pp. 47-58.

del Castillo, J. and Katz, B. (1954) 'Quantal components of the end-plate potential', *J Physiol,* 124(3), pp. 560-73.

Edwards, D. R., Handsley, M. M. and Pennington, C. J. (2008) 'The ADAM metalloproteinases', *Mol Aspects Med,* 29(5), pp. 258-89.

Fatt, P. and Katz, B. (1951) 'An analysis of the end-plate potential recorded with an intracellular electrode', *J Physiol,* 115(3), pp. 320-70.

Fernández, E., Collins, M. O., Uren, R. T., Kopanitsa, M. V., Komiyama, N. H., Croning, M. D. R., Zografos, L., Armstrong, J. D., Choudhary, J. S. and Grant, S. G. N. (2009) 'Targeted tandem affinity purification of PSD-95 recovers core postsynaptic complexes and schizophrenia susceptibility proteins', *Molecular Systems Biology,* 5(1).

Fukata, Y., Adesnik, H., Iwanaga, T., Bredt, D. S., Nicoll, R. A. and Fukata, M. (2006) 'Epilepsy-related ligand/receptor complex LGI1 and ADAM22 regulate synaptic transmission', *Science,* 313(5794), pp. 1792-5.

Giesemann, T., Schwarz, G., Nawrotzki, R., Berhörster, K., Rothkegel, M., Schlüter, K., Schrader, N., Schindelin, H., Mendel, R. R., Kirsch, J. and Jockusch, B. M. (2003) 'Complex Formation between the Postsynaptic Scaffolding Protein Gephyrin, Profilin, and Mena: A Possible Link to the Microfilament System', *The Journal of Neuroscience,* 23(23), pp. 8330.

Han, K. and Kim, E. (2008) 'Synaptic adhesion molecules and PSD-95', *Prog Neurobiol,* 84(3), pp. 263-83.

Jin, Y. and Garner, C. C. (2008) 'Molecular Mechanisms of Presynaptic Differentiation', *Annual Review of Cell and Developmental Biology,* 24(1), pp. 237-262.

Kandel, E. R. (2007) *In Search of Memory: The Emergence of a New Science of Mind.* W. W. Norton.

Kandel, E. R., Schwartz, J. H. and Jessel, T. M. (2000) *Principles of Neural Science.* 4th-Edition edn.: Mc Graw-Hill.

Kegel, L., Aunin, E., Meijer, D. and Bermingham, J. R. (2013) 'LGI proteins in the nervous system', *ASN Neuro,* 5(3), pp. 167-81.

McMahon, S. A. and Díaz, E. (2011) 'Mechanisms of excitatory synapse maturation by trans-synaptic organizing complexes', *Curr Opin Neurobiol,* 21(2), pp. 221-7.

Nägerl, U. V. and Triller, A. (2016) *Nanoscale Imaging of Synapses: New Concepts and Opportunities.* Springer New York.

Okabe, S. (2007) 'Molecular anatomy of the postsynaptic density', *Molecular and Cellular Neuroscience,* 34(4), pp. 503-518.

Palay, S. L. (1956) 'Synapses in the central nervous system', *J Biophys Biochem Cytol,* 2(4 Suppl), pp. 193-202.

Palay, S. L. and Palade, G. E. (1955) 'The fine structure of neurons', *J Biophys Biochem Cytol,* 1(1), pp. 69-88.

Renner, M., Specht, C. G. and Triller, A. (2008) 'Molecular dynamics of postsynaptic receptors and scaffold proteins', *Curr Opin Neurobiol,* 18(5), pp. 532-40.

Schoch, S. and Gundelfinger, E. D. (2006) 'Molecular organization of the presynaptic active zone', *Cell and Tissue Research,* 326(2), pp. 379-391.

Schulte, U., Thumfart, J. O., Klöcker, N., Sailer, C. A., Bildl, W., Biniossek, M., Dehn, D., Deller, T., Eble, S., Abbass, K., Wangler, T., Knaus, H. G. and Fakler, B. (2006) 'The epilepsy-linked Lgi1 protein assembles into presynaptic Kv1 channels and inhibits inactivation by Kvbeta1', *Neuron,* 49(5), pp. 697-706.

Sheng, M. and Hoogenraad, C. C. (2007) 'The Postsynaptic Architecture of Excitatory Synapses: A More Quantitative View', *Annual Review of Biochemistry,* 76(1), pp. 823-847.

Siddiqui, T. J. and Craig, A. M. (2011) 'Synaptic organizing complexes', *Curr Opin Neurobiol,* 21(1), pp. 132-43.

Yang, P., Baker, K. A. and Hagg, T. (2006) 'The ADAMs family: coordinators of nervous system development, plasticity and repair', *Prog Neurobiol,* 79(2), pp. 73-94.

Zuber, B., Nikonenko, I., Klauser, P., Muller, D. and Dubochet, J. (2005) 'The mammalian central nervous synaptic cleft contains a high density of

periodically organized complexes', *Proc Natl Acad Sci U S A,* 102(52), pp. 19192-7.

Chapter2

Introduction to super-resolution fluorescence microscopy

A detailed characterization of the architecture of synaptic proteins and their related processes can only be achieved by looking at the nanometric level using super-resolution techniques. In addition to high spatial resolution, super-resolution microscopy also offers high molecular specificity and the ability to discriminate among multiple molecular components of the synapse.

With the advent of electron microscopy, it has been possible to observe synapses at the nanoscale level. The use of electron microscopy with immunogold staining has enabled discriminating specific components of the synapse within a sea of many proteins (Arthur et al., 2007, Chen et al., 2008, Peters et al., 1991). However, due to its low efficiency and low throughput, immunogold electron microscopy is difficult to use at a large scale to identify molecular organization of multiple synaptic proteins. Fluorescence microscopy on the other hand is capable of multilabeling and simultaneous imaging in 3D. With the arrival of super-resolution techniques, the limitation of resolution was overcome and it became possible to image a numerous set of proteins and protein complexes at the nanometric scale. Particularly, the positioning of numerous pre- and post-synaptic proteins was determined with 3D super-resolution microscopy (Dani et al., 2010).

The first high resolution image of a synapse was acquired in the 1950s by two laboratories in parallel. They used electron microscopy to resolve the synaptic structure (De Robertis and Bennett, 1955, Palay and Palade, 1955). However, this technique presents several disadvantages when we want to study the composition of synapses with molecular specificity or study the dynamics of synaptic proteins in live cells, where less invasive techniques are necessary. Fluorescence super-resolution techniques are a clear alternative as they offer complementary capabilities to electron microscopy: (1) high molecular specificity through targeted labelling and imaging of specific cellular and subcellular populations, (2) multi-color imaging and (3) high-throughput. In this chapter we will focus on the single-molecule localization fluorescence techniques that are widely used to visualize synaptic proteins.

2.1 Introduction to the single-molecule localization imaging techniques

Since the development of the first microscope by Van Leeuwenhoek in the 16th century, scientist have been looking for ways to improve the imaging capabilities of the compound microscope. Fluorescence microscopy has become the workhorse of almost every biological laboratory around the world. Wide-field microscopy with visible light has experienced a revolution over the years. Key technological developments improving the features of the optical microscopes have expanded the capabilities of fluorescence microscopy. Moreover, more complex modalities such as total internal reflection (TIRF), confocal, two-photon, etc. have overcome barriers that allowed imaging of deep tissue samples with reduced background fluorescence. Additionally, the development of a large palette of fluorescent probes has opened the opportunity to label almost anything inside cells and at the same time with different colors and high specificity. Visible light is also mostly non-invasive, giving the opportunity to image dynamic biological processes in real time inside living cells or living animals.

One major limitation for improvement in fluorescence microscopy has been the diffraction limit, present in all optical systems, due to the diffraction of light that prevents the focusing of light to an infinitesimally small spot. Ernst Abbe described it in 1873 by introducing the term numerical aperture and stated that the resolution of a microscope is defined by

$$\text{Lateral (X, Y) resolution: } r = \frac{\lambda}{2NA}; \qquad \text{Axial (Z) resolution: } r = \frac{2\lambda n}{NA^2}$$

where λ is the wavelength of the incident light, n is the index of refraction of the medium and NA is the numerical aperture of the microscope objective. The resolving power of the microscope will be given by the ability to discriminate two different single emitters separated a certain distance (**Figure 2.1**). This separation cannot be longer than λ/2NA.

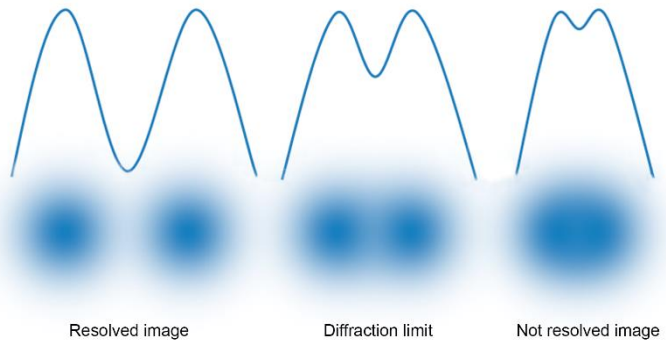

Figure 2.1 Spatial resolution. *Two-point sources going through an optical setup will only be resolved if they are separated more than the diffraction limit given by the optical setup and the wavelength of the light source.*

Optical microscopes face this limit at ~200nm in the lateral direction and ~500 nm in the axial direction. However, most of the biological structures, such as protein complexes, cytoskeletal filaments, DNA and viruses, are below this range, making it very difficult to study these structures in the particularly crowded cell environment.

However, in the last decade, fluorescence microscopy overcame this limitation with the discovery of photoswitchable fluorescent probes (Bates et al., 2005, Heilemann et al., 2005, Patterson and Lippincott-Schwartz, 2002). The fact that probes can have two or more states (dark states or other spectral fluorescent states) helped the scientists to engineer techniques to increase the resolution by 10-fold with respect to the standard resolution of the optical microscope. These super-resolution methods started in 1999 with stimulated emission depletion (STED) (Klar and Hell, 1999). Since then, other powerful techniques were developed for nanoimaging, such as saturated structured illumination microscopy (SSIM) (Gustafsson, 2005), (direct) stochastic optical reconstruction microscopy ((d)STORM) (Heilemann et al., 2008, Rust et al., 2006) and (fluorescence) photoactivation localization microscopy ((f)PALM) (Betzig et al., 2006, Hess et al., 2006). The worldwide recognition of these innovative methods came in 2014 with the Nobel Prize in Chemistry, awarded to the

pioneers of these techniques: Stefan W. Hell for proposing the first super-resolution technique based on patterned illumination, and Eric Betzig and William E. Moerner for laying the foundation for single-molecule super-resolution microscopy techniques (STORM, PALM and fPALM).

Even though all these techniques have demonstrated their strong capability to obtain super resolved fluorescent images, we will only focus on the fluorescent techniques used in this thesis: PALM and STORM.

They rely on the ability to detect and localize the signal coming from a single point-like light source. When imaged by an optical microscope, the image of a single fluorescence emitter will have a size that is determined by diffraction. This image is often referred to as the point spread function (PSF) of the microscope. Even though the PSF is much larger than the emitter itself, its position can nevertheless be determined with high precision by fitting this PSF to a Gaussian distribution and calculating its centroid (**Figure 2.2**).

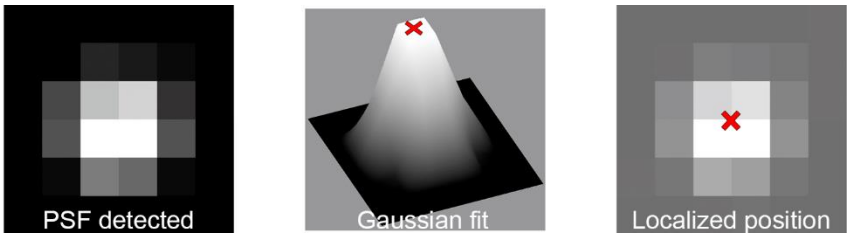

Figure 2.2 Single-molecule localization. *The PSF of a single fluorophore typically shows a Gaussian shape. Fitting its intensity profile into a Gaussian distribution allows us to find the centroid (red cross), giving the localized position of the fluorophore with nanometric precision.*

Therefore, the concept of single-molecule localization alone is not enough to break the diffraction limit and single-molecule localization microscopy (SMLM) super-resolution techniques use additional features. The most relevant one is the stochastic on/off switching of fluorescent probes. In the next section of the chapter, we will develop more precisely this concept.

2.2 On/off switching concept for super-resolution in single-molecule localization microscopy

As mentioned before, single-molecule localization techniques such as PALM or STORM rely on the localization precision of single fluorescent emitters and the ability to separate the position of two of these emitters in space. The discovery of photoswitchable fluorophores put a saddle point in the evolution of the single-molecule fluorescence techniques. It allowed to overcome the diffraction limit of the optical microscopes, both in lateral and axial directions by 10-fold (Bates et al., 2005, Heilemann et al., 2005, Patterson and Lippincott-Schwartz, 2002). These fluorophores have the ability to cycle between dark and bright states (or between two different spectral states). It is also possible to send the majority of these fluorophores from the bright to a dark state and excite only a subset by controlling the laser power in the presence of special buffers (**Figure 2.3**).

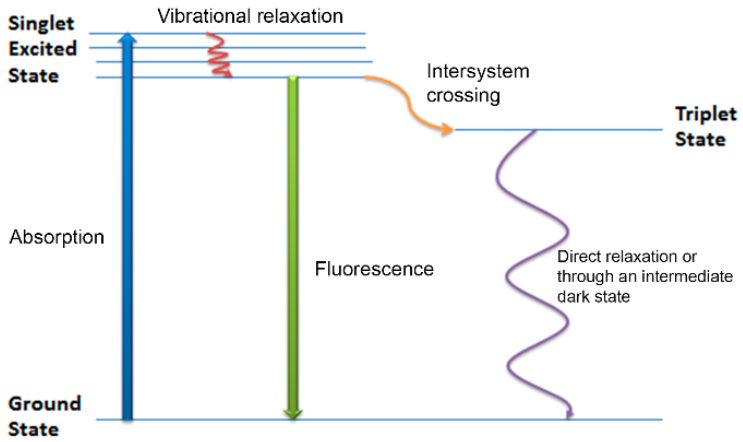

Figure 2.3. On/Off switching cycle. *The simplified Jablonski diagram shows the different molecular states of the fluorophores. After excitation, they either emit fluorescence or go to a dark triplet state. In the case of organic dyes, it is possible to tune their non-fluorescent relaxation time sending the fluorophores to a longer-lived dark state than the triplet state by means of special buffers. Using UV light, it is possible to control the molecules going back to the ground state.*

Even in the case of a dense sample, it is possible to sparsely activate a fraction of the fluorescent probes and precisely determine their position. These separated positions in time can be used to reconstruct an image in high resolution of the fluorescent sample without the limit of diffraction (**Figure 2.4**).

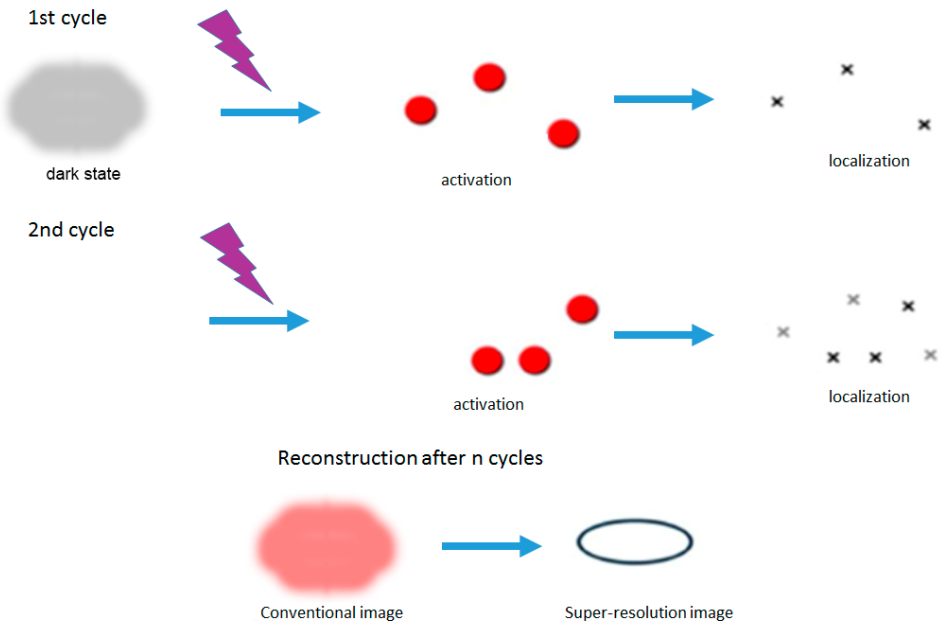

Figure 2.4 Scheme of the single-molecule localization techniques for super-resolution*. In the first cycle of activation with UV light, only a subset of fluorescent probes emit light (red dots). They are localized before they photobleach (black crosses). In the second cycle, a new subset of fluorescent probes become fluorescent and again they are localized before photobleaching and added to the ones of the 1st cycle (now grey crosses). Finally, after n cycles of activation, photobleaching and localization, a super-resolution image can be reconstructed that is about one order of magnitude more resolved than the conventional image.*

The demonstration of this concept was shown in two different methods. In one case using a fluorescent dye-pair, where Cy3 and Cy5 were combined to obtain a super-resolved image (Bates et al., 2005, Heilemann et al., 2005) and in the other case with a photoactivatable fluorescent protein, PA-GFP (Patterson and Lippincott-Schwartz,

2002). Since then, a large palette of fluorescent probes suitable for these techniques has been developed. In the next section, we expand the description of these fluorescent probes.

2.3 Photoswitchable probes used in single-molecule localization techniques

A wide range of probes have been developed for SMLM techniques. Their common feature is the ability to photoswitch from one state to another. Different SMLM techniques use different types of probes, here we summarize the most common ones.

2.3.1 Photoswitchable probes

Organic dyes

Organic dyes are typically attached to the protein of interest by immunohistochemistry. They are often brighter than fluorescent proteins and can switch from dark to bright state many times before they photobleach. These features make them very suitable to super-resolution techniques but their photophysics can be hard to control. There is a wide range of colors. Examples include rhodamines (Alexa Fluor® 488 [A488], Alexa Fluor® 532 [A532], Alexa Fluor® 568 [A568], ATTO488, ATTO532, ATTO565, tetramethylrhodamine, etc.), cyanines (Cy5, Cy5.5, Cy7, Alexa Fluor® 647 [AF647], etc.) and oxazines (ATTO655, ATTO680, etc.) (Fürstenberg and Heilemann, 2013, van de Linde et al., 2012). It is very common that a combination of dyes with different spectral conditions are used in STORM experiments to give a better fluorescent performance. AF647, Cy5.5 and Cy7 are

often combined with a second fluorophore such as Alexa Fluor® 405 [AF405], Cy2, AF488, or Cy3 in an activator-reporter pair configuration to increase the photoswitching efficiency and to facilitate multi-color imaging (Bates et al., 2007, Bates et al., 2012). The fluorescent state of the reporter is recovered from a dark state upon illumination of the activator dye with its absorption wavelength laser light (**Figure 2.5**).

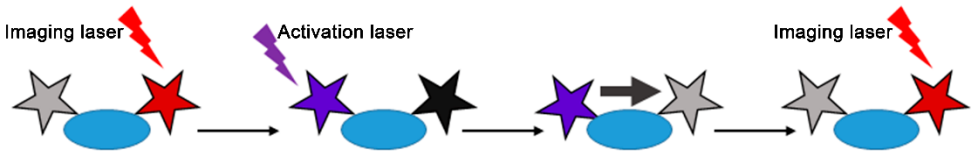

Figure 2.5 Organic dye-pair cycle. *The possibility to bind two organic dyes in the same antibody close to each other allows energy transfer between them under certain conditions. By means of light excitation, one of the dyes, called activator (purple), transfers non-radiatively its energy to the other dye, called reporter (red), allowing a better control of its blinking.*

Additionally, some photoswitchable fluorophores can be directly bound to specific structures of interest, such as DNA (Picogreen and YOYO-1 (Benke and Manley, 2012, Flors, 2010)) or cellular membrane (Nile red, DiI, DiR, DiD, MitoTracker Orange/ Deep Red, ER-Tracker and LysoTracker Red (Sharonov and Hochstrasser, 2006, Shim et al., 2012)). Furthermore, organic dyes with quencher moieties have also photoswitchable properties for super-resolution techniques (Belov et al., 2010, Lord et al., 2010, Gee et al., 2001, Maurel et al., 2010).

The ability of these fluorochromes to photoswitch or to enhance their photoswitching is one of the key factors for obtaining optimal super-resolved images. Such enhancement is usually achieved by special imaging buffers. These buffers typically contain a reducing agent such as a primary thiol (beta-mercaptoethanol (BME) or cysteamine (MEA) (Bates et al., 2005, Dempsey et al., 2011, Heilemann et al., 2009)), ascorbic acid (Benke and Manley, 2012) or a phosphine (Vaughan et al., 2013). The change of fluorescent state of the organic

dyes is chemically induced. In cyanines like Cy5 or AF647, the primary thiol forms an adduct on the polymethine bridge (Dempsey et al., 2009). Alternatively, other mechanisms can induce the photoswitching such as blinking by transient population of short-lived triplet state that may just last a few milliseconds. Moreover, organic dyes can also reach transient dark states by undergoing reversible cis–trans isomerisation such as cyanines or become reversibly protonated like fluorescein. For further details on the photoswitching mechanism, the reader is addressed to (Fürstenberg and Heilemann, 2013).

Fluorescent proteins

Fluorescent proteins (FPs) have very special photophysical properties that make them very valuable in single-molecule localization techniques. Currently used in the majority of biological imaging experiments, they were discovered in aquatic species such as *Aequorea victoria* or few kinds of algae. The genetic sequence of these proteins can be replicated and introduced into the genome of cells or even animals that will express them. Scientists have also developed several mutations in order to improve the properties of these fluorescent probes. Some of these mutations have allowed the photoswitching of the most relevant ones. They can be classified in two types, depending on their mode of photoswitching.

Reversibly photoswitchable fluorescent proteins

These proteins can be cycled many times between dark and bright states before photobleaching. They can lead to smoother images since the same structure is sampled many times. However, their use in quantitative measurements is limited because of their blinking, making it quite challenging to differentiate localizations that arise from the same probe from ones coming from another probe. The most common examples are Dronpa (Habuchi et al., 2005) and its derivatives, Dreikland

(Dickson et al., 1997), EYFP (Biteen et al., 2008) and rsEGFP (Brakemann et al., 2011). They all undergo a transition from dark to bright state when illuminated with ultraviolet laser light.

Irreversibly photoswitchable fluorescent proteins

In contrast to reversible fluorescent proteins, irreversible probes should in principle be more reliable to be counted and detected only once, thus they are preferable in quantitative analysis.

They can be classified in two subcategories, depending on whether they change their spectral color or change from a dark to a bright state. In the first category one can find mEos2 (Wiedenmann et al., 2004) and its derivatives (mEos3.1, mEos3.2 (Zhang et al., 2012)), Dendra (McKinney et al., 2009), mClavGR2 (Hoi et al., 2010) and mMaple (McEvoy et al., 2012) and its derivatives (mMaple2 and 3 (Wang et al., 2014)). In the second category there are PA-GFP (Patterson and Lippincott-Schwartz, 2002) and PA-mCherry (Subach et al., 2009). However, even some of these irreversible proteins can undergo in multiple reactivations in the same experiment (Annibale et al., 2011b, Durisic et al., 2014b). Therefore, methods have been developed to correct for this artifact in the quantitative analysis. For a more thorough explanation for correcting over-counting artifacts, the reader is directed to (Durisic et al., 2014a). Moreover, it can also happen that the probe is not 100% detectable. In that case, the quantitative measurement will lead to under-counting. This under-counting has to be corrected by other methods. Some i*n vitro* bulk experiments follow the evolution of either the absorption spectrum (McKinney et al., 2009, Wiedenmann et al., 2004, Annibale et al., 2011a, Habuchi et al., 2008) or the bands from the native and the converted forms using a protein gel (McKinney et al., 2009, Wiedenmann et al., 2004, Habuchi et al., 2008). However, these studies do not take into account the dark state of such FPs, therefore the photoswitching efficiency is underestimated. Additionally, this photoswitching efficiency may differ in proteins inside cells compared to the *in vitro* experiments. In this thesis, we

demonstrate a method to overcome all these issues by using well-defined *in vivo* templates to calibrate the fluorescent efficiency of the most important probes used in PALM studies (Chapter 3).

Quantum dots

The last set of fluorophores used in single-molecule techniques are the quantum dots (Dertinger et al., 2009, Hoyer et al., 2011). Even though they are the brightest of the different fluorophores, their main limitation is that they have short times in the dark state, whereas the super-resolution techniques rely on probes having longer off times and shorter times being in the fluorescent state. This parameter is called the duty-cycle and it is more detailed in the next subsection. Some studies propose improvements such as chemical caging and nanocrystal modifications that may propel the use of quantum dots in super-resolution techniques (Han et al., 2008, Hoyer et al., 2011).

2.3.2 Probe characteristics for single-molecule localization techniques

Choosing the proper fluorophore for a certain experiment is essential for the quality of the final image. We have discussed the immense toolbox of fluorescence probes available, but one must take into account their advantages and disadvantages to choose wisely. In fact, to date, only a few set of probes has been demonstrated to be reliable for super-resolution imaging.

When choosing a probe, many of the considerations for regular fluorescent probes are also applicable to the photoswitchable ones. The most common ones are the photostability of such probe and the spectral overlap in case of multi-color imaging. Imaging of live cells can benefit from the use of fluorescent proteins, as they are genetically encoded and their intracellular labeling outperforms the labeling with

organic dyes, however, special care must be taken regarding overexpression when the cells are transfected with these probes. It is also possible to label intracellular proteins using antibodies with organic dyes, which is very useful to label endogenous proteins only, but they rely on the antibody binding and internalization, which can be very challenging in live cells. An alternative is the use of smaller probes such as SNAP, HALO or CLIP tags with a fluorophore bound to them (Jones et al., 2011, Klein et al., 2011, van de Linde et al., 2012). Unfortunately, most of the fluorophores are membrane impermeable, limiting these hybrids to labeling of cell surface proteins. Another option for RNA/DNA labeling is the use of click-chemistry. The modification of nucleic acids with a terminal alkyne group that reacts with a modified probe containing an azyde-group has been proven satisfactory by Zessin et al. (Zessin et al., 2012). The choice of a good probe eventually is reduced to three considerations: brightness of the probe, its fluorescent duty-cycle and its switching kinetics.

Brightness

In SMLM, the brightness of the probe is central to achieve a high resolution. The precision of a fluorophore to be localized depends directly on the number of photons emitted (Thompson et al., 2002). Therefore, probes with higher photon yield will give a more accurate position of the targeted protein and, as a consequence, a higher resolution of the final image of this protein. The brightest fluorophores up to date are AF647 and Cy5. They are proven to be much brighter than the other organic dyes and most of the fluorescent proteins.

On/off duty cycle

Super-resolution using fluorescence can only be achieved when a low number of fluorophores is excited at a given time, to make sure that their point spread functions do not overlap. It is necessary to have probes with a low duty cycle, i. e.

with a long lifetime “off” (dark) state and a short lifetime “on” state (Dempsey et al., 2011). If this is not the case, a large number of fluorophores will be fluorescent at the same time, leading to overlapping of PSFs and loss of localization precision. Moreover, even though having a lower density of probes would solve the PSF overlapping, it would also lead to low spatial resolution (see Section 2.4). The fluorophores that mostly fulfill this requirement are AF647, Cy5, and fluorescent proteins.

Switching kinetics

Another important feature of the fluorophores is the time it takes to send them to the dark state after excitation. This time sets the acquisition time. Exposures longer than this time will decrease the localization precision. The camera rate has to be adjusted to the probe switching kinetics so that it switches off within one frame. Probes with faster switching rates allow faster data acquisition and reduce the time of the whole imaging session that is needed to achieve super-resolution (Dempsey et al., 2011, Jones et al., 2011). This is particularly important in live-cell imaging, which requires high temporal resolution to avoid motion blur. The off rate of certain fluorophores such as AF647 is proportional to the laser power used to image them: at high powers, they switch “off” faster but still emit similar number of photons. Fluorescent proteins, on the other hand, switch with slower rates and their photon output usually decreases with increasing laser illumination intensities (Jones et al., 2011).

In conclusion, a suitable probe for super-resolution techniques has to have a high photon output, a low duty-cycle and a fast switching kinetics. A deep analysis of the characteristics of the different probes has been published (Dempsey et al., 2011)

2.4 Spatial Resolution in single-molecule super-resolution techniques

A critical aspect in the SMLM is the spatial resolution. This resolution is limited by the accuracy in localizing each fluorescent molecule, the labeling density and the probe size.

2.4.1 Localization precision

The localization precision mainly depends on the number of photons detected from a single emitter. Assuming a Gaussian shape and an error just by photon counting, we can calculate the localization precision with the following expression

$$\sigma = \frac{s}{\sqrt{N}}$$

where σ is the localization precision, that depends on s, the standard deviation of the Gaussian fit and the number of counted photons, N. Additional sources of error include finite pixel size, as well as background noise including camera noise and cell auto-fluorescence. Several papers have addressed the fundamental issues in localization precision and have proposed different expressions to describe them (Mortensen et al., 2010, Stallinga and Rieger, 2012, Thompson et al., 2002). In addition, in order to determine the centroid position, several computational methods have been proposed. We highlight the nonlinear least squares fitting to a Gaussian PSF or the maximum likelihood estimation (MLE) using a Gaussian PSF model (Abraham et al., 2009, Mortensen et al., 2010, Ober et al., 2004, Smith et al., 2010). Among these methods, the MLE is the one that gives the highest accuracy. The latest analytical approximation for localization precision was proposed by Stallinga and Rieger in 2012 (Stallinga and Rieger, 2012). The expression is as follows:

$$\sigma^2_{LocPrec} = \frac{s^2 + {a^2}/{12}}{N}\left[1 + 4\tau + \sqrt{\frac{2\tau}{1+4\tau}}\right]$$

where s is the width of the Gaussian that is used to fit the PSF, a is the pixel size, N is the number of collected photons, and τ is a normalized dimensionless background parameter defined as follows: $\tau = 2\pi b(s^2 + a^2/12)/(Na^2)$, with b being the number of background photons per pixel.

An additional property is that the fluorescent molecules used in SMLM do not emit light isotropically but rather as electric dipoles. This clearly affects the localization precision if the emitters have a limited or no rotation during the camera exposure. The shape of the emitter differs from isotropic distribution. Enderlein et al. have characterized this effect in simulations taking into account several parameters such as effective pixel size, numerical aperture of the microscope objective and number of photon counts emitter by the probe (Enderlein et al., 2006). Taking an effective pixel size of ~100 nm, numerical apertures of 1.2-1.4 and photons counts around 500-16000 photons, they calculated an error in the position determination of ~10 nm, significantly independent on the orientation of the fluorescent molecule. In our setup, the numbers are: 1.4 NA objective, 160 nm pixel size, an average number of photons around 1000-2000 photons and then, our localization precision is around ~8-12 nm.

The typical labeling in STORM experiments is performed with dye-labeled antibodies that are not completely fixed, therefore, they have flexibility in the orientation and basically perform as isotropic emitters.

In practice, the localization precision can be determined by measuring the standard deviation of a cluster of localizations coming from a single emitter (Huang et al., 2008, Rust et al., 2006).

As mentioned before, the localization precision depends of the number of photons emitted, therefore, bright dyes such as AF647 have a higher localization precision

(typically 8-9 nm). Instead, fluorescent proteins have a lower photon output and their localization precision is commonly around 20 nm.

2.4.2 Labeling density and Nyquist criterion

The labeling density is a crucial point in the SMLM experiments and it highly affects the spatial resolution. When labeling fails to target all the molecules, different effects can be seen. The most common one is seeing continuous structures being partly cut in a random way, resulting in loss of detail.

The Nyquist criterion quantifies the effects of the labelling density on the effective spatial resolution (Shroff et al., 2008). This criterion states that target structures separated less than twice the fluorophore-to-fluorophore distance cannot be reliably resolved.

$$\sigma_{Nyquist} = {}^{2}/_{\rho^{1/D}}$$

where ρ is the labeling density obtained by calculating the number of localizations per unit area or volume and D is the dimension of the structure to be imaged. 2 will correspond to two-dimensional structures and 3 for three-dimensional ones.

The effective resolution can be determined by convoluting the localization precision and the contribution of the labeling density.

$$\sigma_{Effective} = \sqrt{\sigma_{LocPrec}^2 + \sigma_{Nyquist}^2}$$

Taking into account these effects is essential to obtain proper super-resolution results. Optimizing them guarantees a better imaging performance and thus a higher resolution.

Antibody labeling might have important effects such as low labeling efficiency owing to steric hindrance, low antibody affinity or low accessibility of epitopes. On the contrary, fluorescent proteins may avoid the previous effects, however, there are

also several factors that play a key role in the imaging strategy. They are induced via transfection, which typically allows a 1-to-1 ratio between targeted and fluorescent protein, but, as developed more thoroughly in Chapter 3, effects such as unlabeled endogenous proteins or incomplete maturation or photoactivation of these fluorescent proteins may cause a quality loss in imaging results, particularly in quantitative measurements (Durisic et al., 2014a, Durisic et al., 2014b).

Depending on the target, the choice of the right labeling and the availability of high-quality antibodies or fluorescent protein fusion constructs is critical. The optimization of these two factors will ensure a proper imaging performance.

2.4.3 Probe size

The physical size of the probe is another important factor in determining spatial resolution of the final image. It is important to mention that typically the size of the probes is in the same order as the size of the target protein as well as the localization precision and thus impacts the achievable spatial resolution. The organic dyes are around 1 nm in size, however, they are usually attached to bigger structures such as antibodies (10-15 nm). Smaller probes such as Fab fragments (~5-6 nm) or camelid antibodies, called nanobodies (Ries et al., 2012) (~4nm), may be an alternative. Another option is the targeting of organic dyes using SNAP, CLIP or HALO-tags (~3-4 nm). With a similar size, fluorescent proteins can be another labeling option, but one must be aware of their low photon budget. Alternatively, a direct labeling of specific markers that bind to membranes or organelles, DNA or the use of click-chemistry may reduce the probe size.

Due to their relative simplicity to implement as a well-established procedure, in our STORM experiments we have used the labelling with primary and secondary antibodies. The need to label multiple targets at the same time in primary cells like neurons makes this method the most feasible, as fluorescent protein targeting using

transfection is highly challenging in primary cells. However, in order to measure the absolute stoichiometry, a use of nanobodies or fluorescent proteins would be more recommendable.

2.5 Experimental requirements for single-molecule super-resolution microscopy

Even though it is possible to obtain super-resolution images with any microscope with high power light sources attached, it is important to mention some features in order to reach an optimal image.

Microscope components

Having an optimal microscope configuration is crucial to acquire the images at highest resolution possible. Some of these features include:

- Inverted microscope with total internal reflection fluorescence (TIRF) configuration. TIRF or inclined illumination prevent undesired background fluorescence from thick samples that can affect the spatial resolution.
- High quality oil or water immersion objectives with high numerical aperture and high magnification. It is essential that this objective has the optical aberrations such as chromatic or spherical aberrations properly corrected as much as possible. In our experiments, we used a 100x magnification and 1.4 NA objective.
- Automatic focusing that allows the sample to be in focus to prevent unwanted effects in long image acquisitions such as drift.
- High laser powers are key to generate decent activation and blinking to prevent molecules to emit longer than one frame. Typical intensities in

SMLM experiments are around 0.5-5 kW/cm^2 for fixed cells and around 10 kW/cm^2 for live cell experiments.

- Wavelength tunable devices might be a good choice to allow a variability of intensity powers during image acquisition. Acousto-optical tunable filters or modulators might be a very good option.
- A fast response, high sensitivity acquisition device is also key to improve both the temporal and the spatial resolution. EMCCDs or sCMOS cameras are the best choice in the experiments for SMLM.

Sample preparation

SMLM techniques do not require a very complicated sample preparation in comparison to other techniques. However, some considerations must be taken into account while preparing the sample. Fixation is a key issue that must be optimized to preserve the structure of interest while keeping the epitopes available for antibody binding. In case of using organic dyes attached to antibodies, a proper immunostaining protocol will mark the difference between a poor image and a super-resolved image. Antibody concentrations must be tested before performing the central experiment to optimize for high density labeling while maintaining a low background due to nonspecific labeling. When using dye-pairs, a special care on the dye ratios per antibody must be taken to avoid quenching or too much non-specific blinking. Ratios of 2-4 activator dyes versus 1 reporter dyes per antibody are the most common ones to achieve optimal labeling (Bates et al., 2007). In conclusion, good preservation of the structure, high specificity, high labeling density and low background are the aspects to pay attention to for an optimal sample preparation protocol for SMLM.

Imaging buffers

Organic fluorophores require the use of special buffers for proper photoswitching. Fluorophore photoswitching is highly dependent on the use of reducing agents and

oxygen scavengers. Primary thiols such as BME or MEA are some examples of reducing agents used in order to shelve the molecule into stable dark states. Another essential component is an oxygen scavenger such as glucose oxidase and catalase that increases the photostability of the fluorophores by scavenging reactive oxygen species. Additionally, higher blinking is achieved at higher pH conditions, therefore, a strong buffer such as PBS or TRIS is necessary to maintain the pH especially in the presence of acidic by-products that may come from the reactions with the oxygen scavenger.

Data analysis for reconstruction

Once the data is acquired at optimal sample conditions, the next key player is the software for analysis. The acquisition of individual frames has to be translated into a reconstruction of localizations. In each frame a certain number of molecules are detected. These detections have to be identified, fitted and rendered.

1) Single-molecule identification

   The identification of the single-molecules is performed by applying a threshold to the frames and finding pixels that have a higher intensity number than its adjacent ones. These pixels will denote an identification of a molecule. In the eventual case where many pixels have nearby other pixels with high intensities, a deeper analysis needs to be implemented to sequentially process the identification peaks using algorithms that can perform at high densities (Holden et al., 2011, Huang et al., 2011)

2) Localization, filtering and data processing

   Once the molecules have been identified, the next step is to determine their precise localization. The most common method is to fit the PSF to a 2D or 3D Gaussian, considering the fluorescent molecule as a point source. By finding the centroid it is possible to precisely localize that molecule. This fitting is performed using nonlinear least squares algorithms such as Levenberg-Marquardt method (Rust et al., 2006) or maximum likelihood

estimation (MLE) where a Gaussian PSF and a Poisson noise model are used (Brede and Lakadamyali, 2012). In the case of densely labeled samples there are other algorithms such as the ones implemented by Cox et al., 2011, Holden et al., 2011 and Zhu et al., 2012.

Optimal resolution can be achieved by applying different filters that keep only the localizations from molecules that satisfy certain criteria. Features such as brightness, localization precision or width are the most common ones. To further improve localization precision, peaks appearing in nearby frames can be linked together and considered as coming from the same molecule, based on the spatial and temporal distance between the peaks. Usually only peaks appearing in consecutive frames are considered to come from the same switching cycle of the same molecule.

Finally, additional data processing methods are applied to improve the image quality. The drift coming from the stage must be corrected. This drift can be corrected either by tracking the position of fiduciary fluorescent markers (Betzig et al., 2006) or by splitting the data into subsets of frames (Bates et al., 2007). In the latter case, images generated from each subset of frames can be correlated to correct for drift.

3) Rendering

Rendering is used to reconstruct the super-resolution image of all the identified localizations. Each localization is represented with one single point. These points can be tuned to show as crosses, dots, simple or weighted Gaussians according to the intensity. The width of the weighted Gaussians typically represents the localization precision (Rust et al., 2006).

Different software has been published to analyze and render SMLM data. Some of these algorithms are openly available such as DAOSTORM (Holden et al., 2011), which was later extended to 3D (Babcock et al., 2012), and others that perform different calculations such as compressed-sensing (Zhu et al., 2012) or Bayesian analysis (Cox et al., 2011). There are also open analysis algorithms that can be used

as plugins such as QuickPALM (Henriques et al., 2010), GraspJ (Brede and Lakadamyali, 2012) and rapidSTORM (Wolter et al., 2012). Recently, a review was published comparing the performance of all these algorithms (Small and Stahlheber, 2014).

2.6 Super-resolution modalities

The implementation of theses SMLM techniques was followed by new technical improvements to extend these methods to multi-color and 3D imaging. Here we explain the most relevant ones together with the ones used in this thesis.

2.6.1 Multi-color imaging

The development of new probes has expanded the possibility to target more than one protein, allowing multi-color imaging in super-resolution. This possibility extends immensely the capabilities of super-resolution techniques. In most of the biological systems, it is essential to examine multiple proteins at the same time, because they are interconnected in the biological processes. It is very rare to find a process where only one single protein is involved. Photoswitchable fluorescent proteins with different spectra can be used for multi-color imaging. Combinations such as PA-GFP/PA-mCherry, PA-mCherry/PS-CFP2, Dronpa/EosFP or PS-CFP2/EosFP have been successfully used for multi-color super-resolution imaging (Annibale et al., 2012, Renz et al., 2012, Shroff et al., 2007). Multi-color can also be achieved with organic dyes with different spectral properties. However, these dyes need specific buffers to perform properly and it is common that a certain buffer is optimal for one specific dye but not for the rest. It is important to remark that additional considerations such as chromatic aberrations and spectral sensitivity of the detector must be taken into account.

An alternative approach that does not suffer from chromatic aberrations is the use of organic dye-pairs (Bates et al., 2007). Labeling the different target proteins with different activator-reporter dye pairs, one can achieve multi-color super-resolution imaging. By keeping the same reporter and using different activators, the color coding can be performed based on the activation light. First, one of the activators is excited with its corresponding laser light and, ideally, only its reporter will be imaged right after until it goes to the dark state (preferably in one or two frames), then the next activator can be excited, and its corresponding reporter can be imaged (**Figure 2.6**). One disadvantage of this approach is the presence of color cross-talk. This effect arises from either a probe that non-specifically blinks independently of the activation laser and is assigned to the wrong channel (Bates et al., 2012) or from cross activation of the probe by the wrong activation laser. Although it is difficult to eliminate cross talk during image acquisition, there are effective ways to remove it using postprocessing based on statistical modeling (Bates et al., 2007, Dani et al., 2010).

This strategy can be extended to additional colors by selecting as many unique activator–reporter dye pairs as possible. Currently, there are nine spectral pairs that have been experimentally optimized for STORM, which combine AF405, Cy2 (or AF488), and Cy3 (or AF555) as the activator and Cy5 (or AF647), Cy5.5 (or AF680), and Cy7 (or AF750) as the reporter (Bates et al., 2007, Bates et al., 2012) (**Figure 2.6**), although additional potential fluorophores have also been suggested (Dempsey et al., 2011). It is important to note that not all activator-reporter pairs will perform equally well, which can result in non-uniform image quality with respect to each of the different colors.

Alternatively, another multi-color strategy is performing sequential imaging. An approach developed in our lab relies on sequential labeling and imaging avoids the color-cross talk as well as the need for multiple fluorophores (Tam et al., 2014). A

downside of this method is the time investment needed for sequential labeling and imaging, which makes acquiring many colors slow.

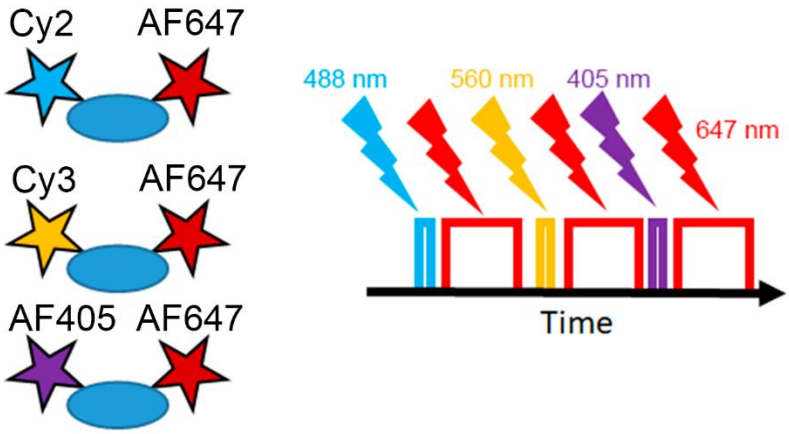

Figure 2.6. 3-color STORM imaging. *Having 3 dye-pairs with the same reporter and 3 different activators allows multi-color imaging (left). By controlling the excitation light of the 3 activators, the images of the reporters can be extracted separately in 3 different channels using consecutive cycles of laser illumination for each of the dye-pairs (right).*

Multi-color imaging has been very useful in neurons to determine the structure of protein complexes in axons and dendrites. In 2010, a multi-color 3D STORM imaging approach to determine the protein architecture of brain sub-cellular structures was developed to characterize the molecular organization of ten pre- and postsynaptic proteins (Dani et al., 2010). They performed 3-color STORM using the one reporter and 3 activator dye-pair modality to identify the position of several synaptic proteins as well as to give a precise quantification of the number of proteins in the synapse.

2.6.2 3D imaging

Most biological structures are three dimensional, whereas many of the imaging strategies are limited to two dimensions. In super-resolution techniques, there are several different approaches to obtain 3D images from the biological structures of

interest with high spatial resolution. One of the simplest methods is the use of a cylindrical lens in the optical path to introduce astigmatism. Due to this astigmatism, the signal coming from molecules that are exactly in the focal plane looks like a circular Gaussian, whereas the signal from molecules above or below the focal plane has the shape of an elliptical Gaussian, elongated either in the horizontal or vertical direction, depending on the orientation of the astigmatic lens (**Figure 2.7**).

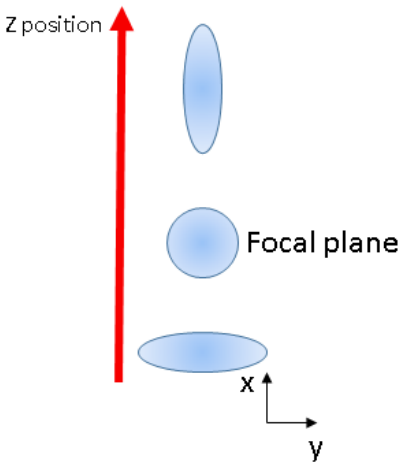

Figure 2.7. PSF astigmatism. *The addition of a cylindrical lens into the optical path of a microscope induces an elliptical deformation of the PSF along the axial direction for the molecules that are not in the focal plane. The ellipse goes in either the directions of the optical plane, depending on whether it is above or below the focus. By measuring the width of the ellipse, one can extract the position of the molecule in z with a previously calibrated curve.*

With a proper calibration, the ellipticity of the Gaussian function can be translated into an axial position. The calibration can be performed using a piezoelectric stage and a glass coverslip with diffraction-limited, fluorescent microspheres sparsely adsorbed onto the glass surface. By acquiring a series of images at fixed z-steps, a calibration curve relating z to the width (in either x or y) of the PSFs can be generated. This calibration curve can then be used to calculate the z-position of subsequent single-molecule localizations acquired using the same system. This method can yield an axial range of ~800 nm with an axial resolution of 50-60 nm. Additional details are explained in (Huang et al., 2008). This method for 3D imaging is the most used in the lab and interesting results related to the behavior of the cargo transport in microtubule intersections have been discovered (Bálint et al.,

2013, Verdeny-Vilanova et al., 2017). However, the number of localizations acquired is reduced with respect to 2D images, therefore, it might not be optimal for very low signal samples.

Other 3D super-resolution methods include PSF engineering or interferometric patterning to improve the axial resolution, but it is usually at the expense of the imaging depth (Xu et al., 2012, Pavani et al., 2009, Juette et al., 2008, Shtengel et al., 2009). A recently developed 3D imaging method which utilizes a self-bending point spread function (SB-PSF) based on Airy beams has demonstrated isotropic three-dimensional localization precision of 10–15 nm over a 3 µm imaging depth (Jia et al., 2014), two features that the previously strategies were lacking.

Recently, 3D STORM has been used by the lab of Xiaowei Zhuang to reveal a nanometric periodic structure in axons. They found out that actin, spectrin and adducin form a coordinated periodic lattice in the cortical cytoskeleton of axons (Xu et al., 2013). Spectrin tetramers interconnect periodic rings of short actin filaments capped by adducing at one of their ends. Such rings are separated by 180-190 nm and give the axonal cytoskeleton a long-range order. More interestingly, this periodic structure was found in axons but not in dendrites.

2.6.3 Live-cell imaging

One of the greatest advantages of fluorescence microscopy with respect to other high-resolution techniques such as electron microscopy is the possibility to acquire images of the dynamics in live cells. SMLM techniques are in principle compatible with live cell imaging. Even though there is no fundamental limitation to apply these techniques to live cells, it is a high challenge due to the timescale of the imaging. In order to obtain super-resolved images, it is essential to have an acquisition speed faster than the biological process being observed. Obtaining multiple localizations in a very short time so that the Nyquist criterion is satisfied is highly challenging

(Huang et al., 2010, Shroff et al., 2008). Therefore, an image that can last several minutes in fixed cells needs to be fasten up to a few seconds. One way to tune this time is to excite organic fluorophores with high laser intensities such that they switch off into the dark state faster without compromising the photon output (Jones et al., 2011). While fluorescent proteins are more suitable probes for intracellular labeling, their slow photoswitching and low photon output may compromise the temporal resolution. Another critical aspect is the time response of the acquisition camera. The camera frame rate has to match with the fluorophore photoswitching rate. In EMCCD cameras, by sacrificing part of the field of view, it is possible to decrease the exposure time and thus obtain a higher frame rate. sCMOS cameras can acquire at much higher speeds while maintaining a large field of view but at the compromise of quantum efficiency and sensitivity. In conclusion, a high temporal resolution can be achieved at the expense of spatial resolution, field of view or both. Finding a balance between these aspects may give the optimal super-resolved image. The first to achieve super-resolution imaging in live cells was Wombacher et al. (Wombacher et al., 2010) performing live cell dSTORM imaging the dynamics of histone protein H2B. They reached 20 nm spatial resolution and 10 nm temporal resolution. Later on, with the arrival of the scientific complementary metal-oxyde semiconductor (sCMOS), an increase in the temporal resolution without sacrificing the field of view was possible (Huang et al., 2013). A detailed review on the requirements for live cell imaging can be found in Lakadamyali, 2014.

Super-resolution imaging of live neurons still remains quite challenging nowadays. Most of the examples use STED or single-particle tracking (SPT) in order to study the dynamics of the nerve cells. Nair et al. used spt-PALM to determine the structure and the dynamics of AMPAR in synapses (Nair et al., 2013). They demonstrated that AMPA receptors are organized and stabilized in highly dense domains of ~ 70 nm in the synaptic boutons.

2.6.4 Hybrid imaging methods

More recently, the need to study dynamic biological processes at high resolution have driven researchers to find better approaches, where spatial and temporal resolution are not compromised with one another. Hybrid methods have been developed to overcome these limitations. An approach developed in our lab took advantage of single particle tracking combined with 3D STORM to reveal the impact of the microtubule network in the dynamics of cargo transport. By means of correlative and sequential imaging it was possible to map the trajectories of lysosomes in individual microtubules and their behavior at the intersections. They demonstrated that the axial separation of microtubules affects the cargo motion (Bálint et al., 2013). Further, they extended the imaging to 3D single particle tracking and showed how vesicles are regulated at these intersections depending on their size and how they overcome obstacles (Verdeny-Vilanova et al., 2017).

2.7 Quantitative super-resolution microscopy

With the arrival of nanoscopy, a higher interest in single-molecule quantification has emerged. The need for properly quantifying the super-resolution images has driven researchers to develop diverse data analysis tools to cover all the requirements. The quantitative information of interest can take several forms including characterization of image resolution, measure of nanostructure or nanocluster sizes, quantification of spatial (co)-organization of nanoclusters and 'molecular counting' of protein numbers. The increased resolution imposes stringent conditions on data analysis and extra care must be taken to ensure that photophysical properties of the probes, labeling and imaging strategies used do not lead to misinterpretation of the data. As the nanoscopy field has progressed at a fast pace, several new methods have also been developed for 'post-image' analysis. A review explaining the different demands to take into account while performing quantitative super-resolution methods can be found in (Durisic et al., 2014a).

A commonly used quantitative method is quantitative points accumulation in nanoscale topography (qPAINT) (Jungmann et al., 2016), based on the imaging method using DNA-PAINT (Jungmann et al., 2010, Lin et al., 2012, Jungmann et al., 2014, Iinuma et al., 2014, Schlichthaerle et al., 2016), where individual DNA dye-labeled strands transiently bind to protein-targeted strands. The dye only emits fluorescent signal a short time when both strands are bound. By controlling the density of implemented dyes, it is possible to extrapolate the number of target molecules from the measured apparent blinking coming from the dyes.

Another interesting method to quantify targeted proteins was developed in our lab. In this case the signal coming from antibody binding dyes was calibrated (Zanacchi et al., 2017). It was demonstrated that DNA origami can be used as a versatile calibration standard to quantify protein copy number in super-resolution imaging using antibody-dye labeling.

2.7.1 Quantitative super-resolution microscopy in neurons

There is a remarkable number of quantitative studies in neurons performed with super-resolution techniques. Some examples of the use of super-resolution experiments are summarized here.

Firstly, Zhuang's lab has been extensively dedicated to the study neurons by means of super-resolution. They did not only reveal their synaptic position with respect to the synaptic cleft, as mentioned before, but also quantified two of the most commonly studied proteins, GluR1, from AMPA receptors (AMPARs) and GluN2B, from NMDA receptors, with respect to the quantification of Homer, a very well-defined postsynaptic protein (Dani et al., 2010).

Moreover, other labs have also used super-resolution techniques to quantify the protein stoichiometry of synapses at the nanoscale level. Regarding the postsynaptic

site, Nair, Hozy et al. showed, using four different super-resolution imaging techniques, that the AMPARs are organized in nanodomains of around 70 nm in the synapse (Nair et al., 2013). They also showed that these AMPARs are stabilized in these nanodomains and they diffuse in random dynamics among them. The estimated size of these nanodomains was stipulated using spt-PALM (Manley et al., 2008) and uPAINT (Giannone et al., 2010) in live cells. They used localization maps and confinement of receptor movements from mean squared displacement (MSD) curves and reached comparable results. These results were confirmed in fixed cells using STED, dSTORM and EM. Finally, they reported an estimation of the number of receptors in each nanodomain using the dSTORM images. Taking the distribution and median of the fluorescence intensity coming from an isolated single AMPAR emitter, they calibrated such intensity distribution and extrapolated this measurement to the intensity distribution of the nanodomains to make an estimation of the number of molecules.

In addition to studies in excitatory synapses, there have been also super-resolution quantitative studies in inhibitory synapses. Specht et al. found a close correspondence between the spatial organization of gephyrin scaffolds and glycine receptors (GlyRs) at spinal cord synapses (Specht et al., 2013).

In conclusion, quantification of molecules, particularly proteins in synapses, is possible. Many researchers have studied multiple ways to quantify these super-resolution images at the molecular level. However, in order to do this quantification in a proper way, it is mandatory to have a deep knowledge of the probe that is being used. In the following chapter, we develop a deeper analysis on that matter.

References

Abraham, A. V., Ram, S., Chao, J., Ward, E. S. and Ober, R. J. (2009) 'Quantitative study of single molecule location estimation techniques', *Opt Express,* 17(26), pp. 23352-73.

Annibale, P., Scarselli, M., Greco, M. and Radenovic, A. (2012) 'Identification of the factors affecting co-localization precision for quantitative multicolor localization microscopy', *Optical Nanoscopy,* 1(1), pp. 9.

Annibale, P., Vanni, S., Scarselli, M., Rothlisberger, U. and Radenovic, A. (2011a) 'Identification of clustering artifacts in photoactivated localization microscopy', *Nat Methods,* 8(7), pp. 527-8.

Annibale, P., Vanni, S., Scarselli, M., Rothlisberger, U. and Radenovic, A. (2011b) 'Quantitative photo activated localization microscopy: unraveling the effects of photoblinking', *PLoS One,* 6(7), pp. e22678.

Arthur, C. P., Serrell, D. B., Pagratis, M., Potter, D. L., Finch, D. S. and Stowell, M. H. B. (2007) 'Electron Tomographic Methods for Studying the Chemical Synapse', *Methods in Cell Biology*: Academic Press, pp. 241-257.

Babcock, H., Sigal, Y. M. and Zhuang, X. (2012) 'A high-density 3D localization algorithm for stochastic optical reconstruction microscopy', *Opt Nanoscopy,* 1(6).

Bates, M., Blosser, T. R. and Zhuang, X. (2005) 'Short-range spectroscopic ruler based on a single-molecule optical switch', *Phys Rev Lett,* 94(10), pp. 108101.

Bates, M., Dempsey, G. T., Chen, K. H. and Zhuang, X. (2012) 'Multicolor Super-Resolution Fluorescence Imaging via Multi-Parameter Fluorophore Detection', *ChemPhysChem,* 13(1), pp. 99-107.

Bates, M., Huang, B., Dempsey, G. T. and Zhuang, X. (2007) 'Multicolor super-resolution imaging with photo-switchable fluorescent probes', *Science,* 317(5845), pp. 1749-53.

Belov, V. N., Wurm, C. A., Boyarskiy, V. P., Jakobs, S. and Hell, S. W. (2010) 'Rhodamines NN: a novel class of caged fluorescent dyes', *Angew Chem Int Ed Engl,* 49(20), pp. 3520-3.

Benke, A. and Manley, S. (2012) 'Live-cell dSTORM of cellular DNA based on direct DNA labeling', *Chembiochem,* 13(2), pp. 298-301.

Betzig, E., Patterson, G. H., Sougrat, R., Lindwasser, O. W., Olenych, S., Bonifacino, J. S., Davidson, M. W., Lippincott-Schwartz, J. and Hess, H. F. (2006) 'Imaging intracellular fluorescent proteins at nanometer resolution', *Science,* 313(5793), pp. 1642-5.

Biteen, J. S., Thompson, M. A., Tselentis, N. K., Bowman, G. R., Shapiro, L. and Moerner, W. E. (2008) 'Super-resolution imaging in live Caulobacter crescentus cells using photoswitchable EYFP', *Nat Methods,* 5(11), pp. 947-9.

Brakemann, T., Stiel, A. C., Weber, G., Andresen, M., Testa, I., Grotjohann, T., Leutenegger, M., Plessmann, U., Urlaub, H., Eggeling, C., Wahl, M. C., Hell, S. W. and Jakobs, S. (2011) 'A reversibly photoswitchable GFP-like protein with fluorescence excitation decoupled from switching', *Nat Biotechnol,* 29(10), pp. 942-7.

Brede, N. and Lakadamyali, M. (2012) 'GraspJ: an open source, real-time analysis package for super-resolution imaging', *Optical Nanoscopy,* 1(1), pp. 11.

Bálint, Š., Verdeny Vilanova, I., Sandoval Álvarez, Á. and Lakadamyali, M. (2013) 'Correlative live-cell and superresolution microscopy reveals cargo transport dynamics at microtubule intersections', *Proc Natl Acad Sci U S A,* 110(9), pp. 3375-80.

Chen, X., Winters, C. A. and Reese, T. S. (2008) 'Life Inside a Thin Section: Tomography', *The Journal of Neuroscience,* 28(38), pp. 9321.

Cox, S., Rosten, E., Monypenny, J., Jovanovic-Talisman, T., Burnette, D. T., Lippincott-Schwartz, J., Jones, G. E. and Heintzmann, R. (2011) 'Bayesian localization microscopy reveals nanoscale podosome dynamics', *Nat Methods,* 9(2), pp. 195-200.

Dani, A., Huang, B., Bergan, J., Dulac, C. and Zhuang, X. (2010) 'Superresolution imaging of chemical synapses in the brain', *Neuron,* 68(5), pp. 843-56.

De Robertis, E. D. P. and Bennett, H. S. (1955) 'SOME FEATURES OF THE SUBMICROSCOPIC MORPHOLOGY OF SYNAPSES IN FROG AND EARTHWORM', *The Journal of Biophysical and Biochemical Cytology,* 1(1), pp. 47-58.

Dempsey, G. T., Bates, M., Kowtoniuk, W. E., Liu, D. R., Tsien, R. Y. and Zhuang, X. (2009) 'Photoswitching mechanism of cyanine dyes', *J Am Chem Soc,* 131(51), pp. 18192-3.

Dempsey, G. T., Vaughan, J. C., Chen, K. H., Bates, M. and Zhuang, X. (2011) 'Evaluation of fluorophores for optimal performance in localization-based super-resolution imaging', *Nat Methods,* 8(12), pp. 1027-36.

Dertinger, T., Colyer, R., Iyer, G., Weiss, S. and Enderlein, J. (2009) 'Fast, background-free, 3D super-resolution optical fluctuation imaging (SOFI)', *Proc Natl Acad Sci U S A,* 106(52), pp. 22287-92.

Dickson, R. M., Cubitt, A. B., Tsien, R. Y. and Moerner, W. E. (1997) 'On/off blinking and switching behaviour of single molecules of green fluorescent protein', *Nature,* 388(6640), pp. 355-8.

Durisic, N., Cuervo, L. L. and Lakadamyali, M. (2014a) 'Quantitative super-resolution microscopy: pitfalls and strategies for image analysis', *Curr Opin Chem Biol,* 20C, pp. 22-28.

Durisic, N., Laparra-Cuervo, L., Sandoval-Álvarez, A., Borbely, J. S. and Lakadamyali, M. (2014b) 'Single-molecule evaluation of fluorescent protein photoactivation efficiency using an in vivo nanotemplate', *Nat Methods*.

Enderlein, J., Toprak, E. and Selvin, P. R. (2006) 'Polarization effect on position accuracy of fluorophore localization', *Opt Express,* 14(18), pp. 8111-20.

Flors, C. (2010) 'Photoswitching of monomeric and dimeric DNA-intercalating cyanine dyes for super-resolution microscopy applications', *Photochem Photobiol Sci,* 9(5), pp. 643-8.

Fürstenberg, A. and Heilemann, M. (2013) 'Single-molecule localization microscopy-near-molecular spatial resolution in light microscopy with photoswitchable fluorophores', *Phys Chem Chem Phys,* 15(36), pp. 14919-30.

Gee, K. R., Weinberg, E. S. and Kozlowski, D. J. (2001) 'Caged Q-rhodamine dextran: a new photoactivated fluorescent tracer', *Bioorg Med Chem Lett,* 11(16), pp. 2181-3.

Giannone, G., Hosy, E., Levet, F., Constals, A., Schulze, K., Sobolevsky, Alexander I., Rosconi, M. P., Gouaux, E., Tampé, R., Choquet, D. and Cognet, L. (2010) 'Dynamic Superresolution Imaging of Endogenous Proteins on Living Cells at Ultra-High Density', *Biophysical Journal,* 99(4), pp. 1303-1310.

Gustafsson, M. G. L. (2005) 'Nonlinear structured-illumination microscopy: Wide-field fluorescence imaging with theoretically unlimited resolution', *Proceedings of the National Academy of Sciences of the United States of America,* 102(37), pp. 13081-13086.

Habuchi, S., Ando, R., Dedecker, P., Verheijen, W., Mizuno, H., Miyawaki, A. and Hofkens, J. (2005) 'Reversible single-molecule photoswitching in the GFP-like fluorescent protein Dronpa', *Proc Natl Acad Sci U S A,* 102(27), pp. 9511-6.

Habuchi, S., Tsutsui, H., Kochaniak, A. B., Miyawaki, A. and van Oijen, A. M. (2008) 'mKikGR, a monomeric photoswitchable fluorescent protein', *PLoS One,* 3(12), pp. e3944.

Han, G., Mokari, T., Ajo-Franklin, C. and Cohen, B. E. (2008) 'Caged quantum dots', *J Am Chem Soc,* 130(47), pp. 15811-3.

Heilemann, M., Margeat, E., Kasper, R., Sauer, M. and Tinnefeld, P. (2005) 'Carbocyanine dyes as efficient reversible single-molecule optical switch', *J Am Chem Soc,* 127(11), pp. 3801-6.

Heilemann, M., van de Linde, S., Mukherjee, A. and Sauer, M. (2009) 'Super-resolution imaging with small organic fluorophores', *Angew Chem Int Ed Engl,* 48(37), pp. 6903-8.

Heilemann, M., van de Linde, S., Schüttpelz, M., Kasper, R., Seefeldt, B., Mukherjee, A., Tinnefeld, P. and Sauer, M. (2008) 'Subdiffraction-resolution fluorescence imaging with conventional fluorescent probes', *Angew Chem Int Ed Engl,* 47(33), pp. 6172-6.

Henriques, R., Lelek, M., Fornasiero, E. F., Valtorta, F., Zimmer, C. and Mhlanga, M. M. (2010) 'QuickPALM: 3D real-time photoactivation nanoscopy image processing in ImageJ', *Nat Methods,* 7(5), pp. 339-40.

Hess, S. T., Girirajan, T. P. and Mason, M. D. (2006) 'Ultra-high resolution imaging by fluorescence photoactivation localization microscopy', *Biophys J,* 91(11), pp. 4258-72.

Hoi, H., Shaner, N. C., Davidson, M. W., Cairo, C. W., Wang, J. and Campbell, R. E. (2010) 'A monomeric photoconvertible fluorescent protein for imaging of dynamic protein localization', *J Mol Biol,* 401(5), pp. 776-91.

Holden, S. J., Uphoff, S. and Kapanidis, A. N. (2011) 'DAOSTORM: an algorithm for high- density super-resolution microscopy', *Nat Methods,* 8(4), pp. 279-80.

Hoyer, P., Staudt, T., Engelhardt, J. and Hell, S. W. (2011) 'Quantum dot blueing and blinking enables fluorescence nanoscopy', *Nano Lett,* 11(1), pp. 245-50.

Huang, B., Babcock, H. and Zhuang, X. (2010) 'Breaking the diffraction barrier: super-resolution imaging of cells', *Cell,* 143(7), pp. 1047-58.

Huang, B., Wang, W., Bates, M. and Zhuang, X. (2008) 'Three-dimensional super-resolution imaging by stochastic optical reconstruction microscopy', *Science,* 319(5864), pp. 810-3.

Huang, F., Hartwich, T. M., Rivera-Molina, F. E., Lin, Y., Duim, W. C., Long, J. J., Uchil, P. D., Myers, J. R., Baird, M. A., Mothes, W., Davidson, M. W., Toomre, D. and Bewersdorf, J. (2013) 'Video-rate nanoscopy using sCMOS camera-specific single-molecule localization algorithms', *Nat Methods,* 10(7), pp. 653-8.

Huang, F., Schwartz, S. L., Byars, J. M. and Lidke, K. A. (2011) 'Simultaneous multiple-emitter fitting for single molecule super-resolution imaging', *Biomed Opt Express,* 2.

Iinuma, R., Ke, Y., Jungmann, R., Schlichthaerle, T., Woehrstein, J. B. and Yin, P. (2014) 'Polyhedra self-assembled from DNA tripods and characterized with 3D DNA-PAINT', *Science,* 344(6179), pp. 65-9.

Jia, S., Vaughan, J. C. and Zhuang, X. (2014) 'Isotropic 3D Super-resolution Imaging with a Self-bending Point Spread Function', *Nat Photonics,* 8, pp. 302-306.

Jones, S. A., Shim, S. H., He, J. and Zhuang, X. W. (2011) 'Fast, three-dimensional super-resolution imaging of live cells', *Nat Methods,* 8.

Juette, M. F., Gould, T. J., Lessard, M. D., Mlodzianoski, M. J., Nagpure, B. S., Bennett, B. T., Hess, S. T. and Bewersdorf, J. (2008) 'Three-dimensional sub-100 nm resolution fluorescence microscopy of thick samples', *Nat Methods,* 5(6), pp. 527-9.

Jungmann, R., Avendaño, M. S., Dai, M., Woehrstein, J. B., Agasti, S. S., Feiger, Z., Rodal, A. and Yin, P. (2016) 'Quantitative super-resolution imaging with qPAINT', *Nat Methods,* 13(5), pp. 439-42.

Jungmann, R., Avendaño, M. S., Woehrstein, J. B., Dai, M., Shih, W. M. and Yin, P. (2014) 'Multiplexed 3D cellular super-resolution imaging with DNA-PAINT and Exchange-PAINT', *Nat Methods,* 11(3), pp. 313-8.

Jungmann, R., Steinhauer, C., Scheible, M., Kuzyk, A., Tinnefeld, P. and Simmel, F. C. (2010) 'Single-molecule kinetics and super-resolution microscopy by fluorescence imaging of transient binding on DNA origami', *Nano Lett,* 10(11), pp. 4756-61.

Klar, T. A. and Hell, S. W. (1999) 'Subdiffraction resolution in far-field fluorescence microscopy', *Opt Lett,* 24(14), pp. 954-6.

Klein, T., Löschberger, A., Proppert, S., Wolter, S., van de Linde, S. and Sauer, M. (2011) 'Live-cell dSTORM with SNAP-tag fusion proteins', *Nat Methods,* 8(1), pp. 7-9.

Lakadamyali, M. (2014) 'Super-resolution microscopy: going live and going fast', *Chemphyschem,* 15(4), pp. 630-6.

Lin, C., Jungmann, R., Leifer, A. M., Li, C., Levner, D., Church, G. M., Shih, W. M. and Yin, P. (2012) 'Submicrometre geometrically encoded fluorescent barcodes self-assembled from DNA', *Nat Chem,* 4(10), pp. 832-9.

Lord, S. J., Lee, H. L., Samuel, R., Weber, R., Liu, N., Conley, N. R., Thompson, M. A., Twieg, R. J. and Moerner, W. E. (2010) 'Azido push-pull fluorogens photoactivate to produce bright fluorescent labels', *J Phys Chem B,* 114(45), pp. 14157-67.

Manley, S., Gillette, J. M., Patterson, G. H., Shroff, H., Hess, H. F., Betzig, E. and Lippincott-Schwartz, J. (2008) 'High-density mapping of single-molecule trajectories with photoactivated localization microscopy', *Nat Methods,* 5(2), pp. 155-7.

Maurel, D., Banala, S., Laroche, T. and Johnsson, K. (2010) 'Photoactivatable and photoconvertible fluorescent probes for protein labeling', *ACS Chem Biol,* 5(5), pp. 507-16.

McEvoy, A. L., Hoi, H., Bates, M., Platonova, E., Cranfill, P. J., Baird, M. A., Davidson, M. W., Ewers, H., Liphardt, J. and Campbell, R. E. (2012) 'mMaple: a photoconvertible fluorescent protein for use in multiple imaging modalities', *PLoS One,* 7(12), pp. e51314.

McKinney, S. A., Murphy, C. S., Hazelwood, K. L., Davidson, M. W. and Looger, L. L. (2009) 'A bright and photostable photoconvertible fluorescent protein', *Nat Methods,* 6(2), pp. 131-3.

Mortensen, K. I., Churchman, L. S., Spudich, J. A. and Flyvbjerg, H. (2010) 'Optimized localization analysis for single-molecule tracking and super-resolution microscopy', *Nat Methods,* 7(5), pp. 377-81.

Nair, D., Hosy, E., Petersen, J. D., Constals, A., Giannone, G., Choquet, D. and Sibarita, J. B. (2013) 'Super-resolution imaging reveals that AMPA receptors inside synapses are dynamically organized in nanodomains regulated by PSD95', *J Neurosci,* 33(32), pp. 13204-24.

Ober, R. J., Ram, S. and Ward, E. S. (2004) 'Localization accuracy in single-molecule microscopy', *Biophys J,* 86(2), pp. 1185-200.

PALAY, S. L. and PALADE, G. E. (1955) 'The fine structure of neurons', *J Biophys Biochem Cytol,* 1(1), pp. 69-88.

Patterson, G. H. and Lippincott-Schwartz, J. (2002) 'A photoactivatable GFP for selective photolabeling of proteins and cells', *Science,* 297(5588), pp. 1873-7.

Pavani, S. R., DeLuca, J. G. and Piestun, R. (2009) 'Polarization sensitive, three-dimensional, single-molecule imaging of cells with a double-helix system', *Opt Express,* 17(22), pp. 19644-55.

Peters, A., Palay, S. L. and Webster, H. D. F. 1991. The fine structure of the nervous system: Neurons and their supporting cells. 3rd Edition ed. New York: Oxford University Press.

Renz, M., Daniels, B. R., Vámosi, G., Arias, I. M. and Lippincott-Schwartz, J. (2012) 'Plasticity of the asialoglycoprotein receptor deciphered by ensemble FRET imaging and single-molecule counting PALM imaging', *Proc Natl Acad Sci U S A,* 109(44), pp. E2989-97.

Ries, J., Kaplan, C., Platonova, E., Eghlidi, H. and Ewers, H. (2012) 'A simple, versatile method for GFP-based super-resolution microscopy via nanobodies', *Nat Methods,* 9(6), pp. 582-4.

Rust, M. J., Bates, M. and Zhuang, X. (2006) 'Sub-diffraction-limit imaging by stochastic optical reconstruction microscopy (STORM)', *Nat Methods,* 3(10), pp. 793-5.

Schlichthaerle, T., Strauss, M. T., Schueder, F., Woehrstein, J. B. and Jungmann, R. (2016) 'DNA nanotechnology and fluorescence applications', *Curr Opin Biotechnol,* 39, pp. 41-7.

Sharonov, A. and Hochstrasser, R. M. (2006) 'Wide-field subdiffraction imaging by accumulated binding of diffusing probes', *Proc Natl Acad Sci U S A,* 103(50), pp. 18911-6.

Shim, S. H., Xia, C., Zhong, G., Babcock, H. P., Vaughan, J. C., Huang, B., Wang, X., Xu, C., Bi, G. Q. and Zhuang, X. (2012) 'Super-resolution fluorescence imaging of organelles in live cells with photoswitchable membrane probes', *Proc Natl Acad Sci U S A,* 109(35), pp. 13978-83.

Shroff, H., Galbraith, C. G., Galbraith, J. A. and Betzig, E. (2008) 'Live-cell photoactivated localization microscopy of nanoscale adhesion dynamics', *Nat Methods,* 5(5), pp. 417-23.

Shroff, H., Galbraith, C. G., Galbraith, J. A., White, H., Gillette, J., Olenych, S., Davidson, M. W. and Betzig, E. (2007) 'Dual-color superresolution imaging of genetically expressed probes within individual adhesion complexes', *Proc Natl Acad Sci USA,* 104.

Shtengel, G., Galbraith, J. A., Galbraith, C. G., Lippincott-Schwartz, J., Gillette, J. M., Manley, S., Sougrat, R., Waterman, C. M., Kanchanawong, P., Davidson, M. W., Fetter, R. D. and Hess, H. F. (2009) 'Interferometric fluorescent super-resolution microscopy resolves 3D cellular ultrastructure', *Proc Natl Acad Sci U S A,* 106(9), pp. 3125-30.

Small, A. and Stahlheber, S. (2014) 'Fluorophore localization algorithms for super-resolution microscopy', *Nat Methods,* 11(3), pp. 267-79.

Smith, C. S., Joseph, N., Rieger, B. and Lidke, K. A. (2010) 'Fast, single-molecule localization that achieves theoretically minimum uncertainty', *Nat Methods,* 7(5), pp. 373-5.

Specht, C. G., Izeddin, I., Rodriguez, P. C., El Beheiry, M., Rostaing, P., Darzacq, X., Dahan, M. and Triller, A. (2013) 'Quantitative nanoscopy of inhibitory

synapses: counting gephyrin molecules and receptor binding sites', *Neuron,* 79(2), pp. 308-21.

Stallinga, S. and Rieger, B. 'The effect of background on localization uncertainty in single emitter imaging'. *2012 9th IEEE International Symposium on Biomedical Imaging (ISBI)*, 2-5 May 2012, 988-991.

Subach, F. V., Patterson, G. H., Manley, S., Gillette, J. M., Lippincott-Schwartz, J. and Verkhusha, V. V. (2009) 'Photoactivatable mCherry for high-resolution two-color fluorescence microscopy', *Nat Methods,* 6(2), pp. 153-9.

Tam, J., Cordier, G. A., Borbely, J. S., Sandoval Álvarez, A. and Lakadamyali, M. (2014) 'Cross-talk-free multi-color STORM imaging using a single fluorophore', *PLoS One,* 9(7), pp. e101772.

Thompson, R. E., Larson, D. R. and Webb, W. W. (2002) 'Precise nanometer localization analysis for individual fluorescent probes', *Biophys J,* 82(5), pp. 2775-83.

van de Linde, S., Heilemann, M. and Sauer, M. (2012) 'Live-cell super-resolution imaging with synthetic fluorophores', *Annu Rev Phys Chem,* 63, pp. 519-40.

Vaughan, J. C., Dempsey, G. T., Sun, E. and Zhuang, X. (2013) 'Phosphine quenching of cyanine dyes as a versatile tool for fluorescence microscopy', *J Am Chem Soc,* 135(4), pp. 1197-200.

Verdeny-Vilanova, I., Wehnekamp, F., Mohan, N., Sandoval Álvarez, Á., Borbely, J. S., Otterstrom, J. J., Lamb, D. C. and Lakadamyali, M. (2017) '3D motion of vesicles along microtubules helps them to circumvent obstacles in cells', *J Cell Sci,* 130(11), pp. 1904-1916.

Wang, S., Moffitt, J. R., Dempsey, G. T., Xie, X. S. and Zhuang, X. (2014) 'Characterization and development of photoactivatable fluorescent proteins for single-molecule-based superresolution imaging', *Proc Natl Acad Sci U S A,* 111(23), pp. 8452-7.

Wiedenmann, J., Ivanchenko, S., Oswald, F., Schmitt, F., Röcker, C., Salih, A., Spindler, K. D. and Nienhaus, G. U. (2004) 'EosFP, a fluorescent marker protein with UV-inducible green-to-red fluorescence conversion', *Proc Natl Acad Sci U S A,* 101(45), pp. 15905-10.

Wolter, S., Löschberger, A., Holm, T., Aufmkolk, S., Dabauvalle, M. C., van de Linde, S. and Sauer, M. (2012) 'rapidSTORM: accurate, fast open-source software for localization microscopy', *Nat Methods,* 9(11), pp. 1040-1.

Wombacher, R., Heidbreder, M., van de Linde, S., Sheetz, M. P., Heilemann, M., Cornish, V. W. and Sauer, M. (2010) 'Live-cell super-resolution imaging with trimethoprim conjugates', *Nat Methods,* 7(9), pp. 717-9.

Xu, K., Babcock, H. P. and Zhuang, X. (2012) 'Dual-objective STORM reveals three-dimensional filament organization in the actin cytoskeleton', *Nat Methods,* 9(2), pp. 185-8.

Xu, K., Zhong, G. and Zhuang, X. (2013) 'Actin, spectrin, and associated proteins form a periodic cytoskeletal structure in axons', *Science,* 339(6118), pp. 452-6.

Zanacchi, F. C., Manzo, C., Alvarez, A. S., Derr, N. D., Garcia-Parajo, M. F. and Lakadamyali, M. (2017) 'A DNA origami platform for quantifying protein copy number in super-resolution', *Nature Methods,* 14, pp. 789.

Zessin, P. J., Finan, K. and Heilemann, M. (2012) 'Super-resolution fluorescence imaging of chromosomal DNA', *J Struct Biol,* 177(2), pp. 344-8.

Zhang, M., Chang, H., Zhang, Y., Yu, J., Wu, L., Ji, W., Chen, J., Liu, B., Lu, J., Liu, Y., Zhang, J., Xu, P. and Xu, T. (2012) 'Rational design of true monomeric and bright photoactivatable fluorescent proteins', *Nat Methods,* 9(7), pp. 727-9.

Zhu, L., Zhang, W., Elnatan, D. and Huang, B. (2012) 'Faster STORM using compressed sensing', *Nat Methods,* 9(7), pp. 721-3.

Chapter 3

Quantification for synaptic proteins

As mentioned before, the molecular organization of the proteins present in the synapse is fundamental for synaptic plasticity. Knowing the stoichiometry of the different synaptic receptors and channels will help us to understand the mechanisms of the neuronal transmission. However, in order to obtain reliable results, one must take into account a number of factors which we describe here.

3.1. Introduction to quantification of proteins

Single molecule localization fluorescence techniques rely on the ability to properly detect the PSFs of single molecules as well as the correct digital processing after the acquisition. In the detection, there are several considerations. The density of fluorescent molecules plays a critical role. One must be able to control the molecules that are fluorescent at a given time and this is where the photoswitchable probes come into play. Nevertheless, these probes have complex photophysics, which make quantification highly challenging. Several factors must be calibrated before performing quantitative experiments. First of all, the considerations explained in the previous chapter regarding the image resolution are a central factor. For quantification, the over- and under-counting artifacts resulting from multiple blinking events and inefficient photoactivation, respectively must be taken into account.

Over-counting of fluorescent molecules

Over-counting of molecules results from the fact that while doing single molecule experiments, more molecules than actually present can be counted. This effect can be due to several reasons. One case might be a consequence of the immunocytochemistry staining. The use of polyclonal antibodies may lead to binding of more than one probe in the same protein, giving rise to non-stoichiometric labeling. Another effect of the antibodies is their capability of crosslinking molecules, which leads to artificial clustering. However, if these effects are taken into account and calibrated, one can perform quantitative measurements using antibodies, as long as a calibration curve to extract the number of fluorophores from the number of localizations is measured (Zanacchi et al., 2017). A reasonable alternative to the quantitative experiments with antibodies is the use of fluorescent proteins instead. In principle, fluorescent proteins give rise to one-to-one labeling ratio. Among these fluorescent proteins, irreversibly photoactivatable and

photoconvertible ones are the best candidates for quantitative imaging, since in principle each fluorescent protein is imaged (and counted) only once.

In practice, the fluorescent proteins are transfected to the cells, which usually leads to over-expression and thus non-stoichiometric labeling since the endogenous copy of the protein is unlabeled and not visible. Therefore, to be precise, it is necessary to use genome editing techniques to tag proteins at the endogenous level. However, even if endogenous tagging can be achieved, fluorescent proteins can undergo transitions to non-fluorescent off states (blinking and re-activation) and reappear multiple times during the imaging (Annibale et al., 2010), which gives rise to challenges in quantification. If not taken into account, this effect gives rise to over-counting and may make the image look clustered while there is no actual physical clustering of the target.

Some labs have addressed the over-counting with different methodologies. For further details, the reader is redirected to (Annibale et al., 2011a, Annibale et al., 2011b, Lee et al., 2012, Durisic et al., 2014b, Sengupta et al., 2013, Sengupta et al., 2011, Veatch et al., 2012).

Under-counting and missed molecules

Apart from over-counting, it is also possible to have the opposite effect, missing molecules. A one-to-one ratio between the protein of interest and the probe is the ideal case, however this is often not possible to achieve, especially with antibodies. The large size of the antibodies can be detrimental in quantitative measurements due to steric hindrance. In a dense sample, it may not be possible to label all the proteins if the probe is too big. Smaller probes like nanobodies or aptamers have been demonstrated to lead to denser labeling of certain targets and higher spatial resolution in super-resolution images (Opazo et al., 2012, Ries et al., 2012). However, like antibodies, they depend on their binding affinity. As mentioned above, genetically encoded fluorescent proteins allow a better control on the

protein-probe ratio. Transient transfection, the most common way of tagging proteins with fluorescent proteins in mammalian cells, leads to a mixture of endogenous unlabeled and over- expressed labeled protein. Ideally, one would like to determine the stoichiometry and spatial distribution of endogenous and not overexpressed proteins, but with advances like genome editing, it is now possible to tag endogenous proteins with fluorescent proteins (Ran et al., 2013, Wood et al., 2011). Additionally, the imaging strategy must be such that multiple probes are not photoactivated simultaneously within a diffraction limited volume, since their images will overlap leading to missed events. The number of photoactivated probes is proportional to the power of the photoactivation laser and the total number of the remaining un-activated probes. Therefore, an imaging strategy must be followed in which the power of the photoactivation laser starts out very low and is progressively and slowly increased over time (Lee et al., 2012, Gunzenhäuser et al., 2012). Similarly, the imaging period must be long enough such that all the probes are exhaustively imaged. Plotting a cumulative curve of localized molecules in each frame can give an indication of whether this condition has been satisfied (Gunzenhäuser et al., 2012). The cumulative curve should increase slowly, reaching a plateau once most of the probes have been imaged. Finally, a very important issue for under-counting is photoactivation efficiency, defined as the percentage of fluorescent proteins that can be efficiently photoactivated or photoconverted. A number of recent papers have used calibration standards to calculate the percentage of successful photoactivation during super-resolution imaging for a number of fluorescent proteins (Nan et al., 2013, Puchner et al., 2013) but a thorough and extensive analysis was never done. In our lab we developed a method to calculate the photoactivation efficiency of any fluorescent protein that might be used for such quantitative experiments. In the next part of this chapter we will focus on the characterization of the most commonly used PALM probes in order to use them in quantitative analysis. We took advantage of an *in vivo* nanotemplate with

well-known stoichiometry tagged to the fluorescent protein of interest to calculate their photoactivation efficiency.

For further details on strategies and pitfalls for quantitative analysis in single molecule super-resolution microscopy, the reader is directed to the review of Durisic et al. (Durisic et al., 2014a).

3.2. Human Glycine receptor as a template for quantitative measurements

Oligomers with known stoichiometry are reliable calibration standards which can be used to determine the efficiency of photoactivation or photoconversion of fluorescent proteins. In our studies, we used the Glycine receptor (GlyR) as our nanotemplate. The well-defined and stable stoichiometry of this synaptic receptor makes it a very good candidate to calibrate the photoswitching efficiency of the fluorescent proteins under study. This receptor has a pentameric conformation of three α- and two β-subunits (Durisic et al., 2012) (**Figure 3.1**). The α-subunit can form a homo-pentamer consisting of 5 α-subunits, while β-subunit cannot (Durisic et al., 2012, Lynch, 2009). Therefore, the stoichiometry can be tuned to be two, three or five depending on which subunit is labeled and expressed. In all our experiments, we used *Xenopus* oocytes as expression system since they do not express the human GlyR endogenously (Durisic et al., 2012).

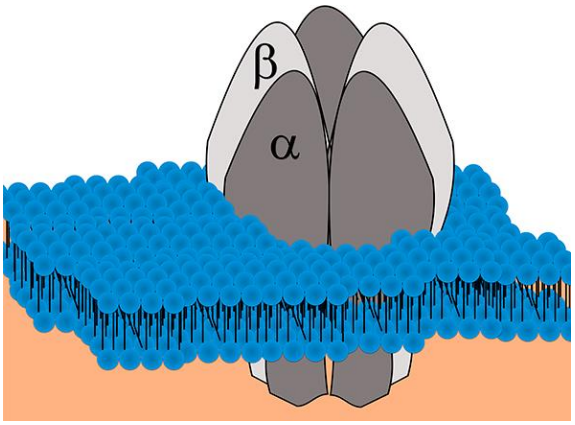

Figure 3.1. Human glycine receptor (GlyR). *This receptor is a heteropentamer containing three α-subunits and two β-subunits, expressed in the cell membrane.*

Once expressed on the surface of the *Xenopus* oocytes, GlyRs are stationary for several minutes, enabling long time measurements even in living cells.
Finally, depending on the time after RNA injection, the expression level evolves from single GlyR density to many GlyRs within a diffraction-limited volume, and thus the observation time can be tuned to image individual GlyRs.

In this thesis, we used two methods to independently determine the photoactivation and the photoconversion efficiency in FPs used in PALM: single-step photobleaching and single-molecule-counting PALM.

3.3. Single-step photobleaching

One of the most reliable ways to characterize stoichiometry of small oligomers is to use the stepwise disappearance of fluorescence corresponding to the photobleaching of single molecules, called single-step photobleaching. This method has been widely used to determine the stoichiometry of different protein complexes (Durisic et al., 2012, Ulbrich and Isacoff, 2007, Simonson et al., 2010, Gaitán-Peñas et al., 2016). It consists of imaging the fluorescent sample with intermediate laser power. The fluorescent protein undergoes photobleaching with a given rate

determined by the laser power used and the recorded signal shows a stepwise decrease in intensity over time as each florescent protein photobleaches. Each step can thus be counted as one protein. For example, ideally, if we count the number of α-subunits in the heteromeric GlyR, one should count 3 steps. If we label the β-subunit, we should see 2 steps. However, the intensity-time traces typically contain both single and double steps when the β-subunit is labeled. The single steps are partially due to a small percentage of "missed events" in which two fluorescent proteins photobleach simultaneously (Ulbrich and Isacoff, 2007, Durisic et al., 2012). These missed events can be accounted for by considering the fluorescence intensity (simultaneous photobleaching of two fluorescent proteins will produce roughly twice the step size compared to a single fluorescent protein) (Durisic et al., 2012). Often, after correction for missed events, a number of single-step traces remain, owing to one of the subunits containing a "dark" fluorescent protein. The percentage of dark fluorescent protein can be determined by fitting the counted number of steps to the binomial distribution (Ulbrich and Isacoff, 2007, Durisic et al., 2012) (See methods section). Thus, single-step photobleaching provides information not only on protein stoichiometry but also on the probability for a fluorescent protein to fluoresce in a given expression system. We used this second property to characterize the photoconversion efficiency (PE) of fluorescent proteins used in PALM experiments. **Figure 3.2** shows a scheme of the single-step photobleaching scheme after photoconversion of mEos2 from green to red.

Because heteromeric GlyRs contain two β-subunits (or three α-subunits), we expected to count a combination of single and double steps (or single, double and triple steps) after photoactivation. Fitting the number of counted steps to the binomial distribution provided the percentage of fluorescent protein that has been successfully photoactivated.

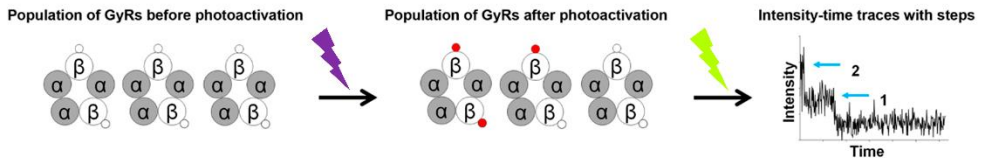

Figure 3.2. Single-step photobleaching scheme. *Heteropentameric ion channels (GlyRs) with two fluorescent protein–tagged β-subunits per channel are photoactivated by varying powers and durations of activation laser (purple ray). For each power (or illumination time) the photoactivated fluorescent proteins are imaged until they photobleach (green ray). Intensity-time traces are used to count the number of single or double photobleaching steps.*

In single molecule super-resolution experiments, mEos2 is the most widely used FP with photoconversion from green to red (Wiedenmann et al., 2004). The native green form changes its conformation when excited with 405nm laser light. The fluorescent emission spectrum changes from 519nm to 584nm. More recently, derivatives of mEos2 were generated with highly monomeric conformation (mEos3.1 and mEos3.2)(Zhang et al., 2012). Similarly, there are other green-to-red photoconversion proteins that are widely used due to their different properties: mClavGR2 (Hoi et al., 2010), mMaple (McEvoy et al., 2012) and Dendra2 (McKinney et al., 2009). Additionally, 2 photoactivatable fluorescent proteins, PA-GFP (Patterson and Lippincott-Schwartz, 2002) and PA-mCherry (Subach et al., 2009), are commonly used.

We characterized the photoswitching efficiency of these 8 important fluorescent proteins used in PALM experiments and analyzed in detail how suitable they are for quantitative measurements.

3.3.1 Single-step photobleaching in photoconvertible fluorescent proteins

In this experiment, we took mEos2 as our reference and characterized the PE in different ways. We also used this FP to perform all the control experiments. We then

characterized the rest of the photoconvertible FPs using the same procedure as for mEos2.

We coexpressed tagged GlyR β-subunit with one of the PALM FPs and untagged α-subunits in *Xenopus* oocytes and carried out single-step photobleaching experiments in living oocytes. We first extracted intensity-time traces from individual GlyRs before photoconversion in order to control the percentage of native FP that is actually fluorescent. These traces showed stepwise photobleaching (**Figure 3.3**).

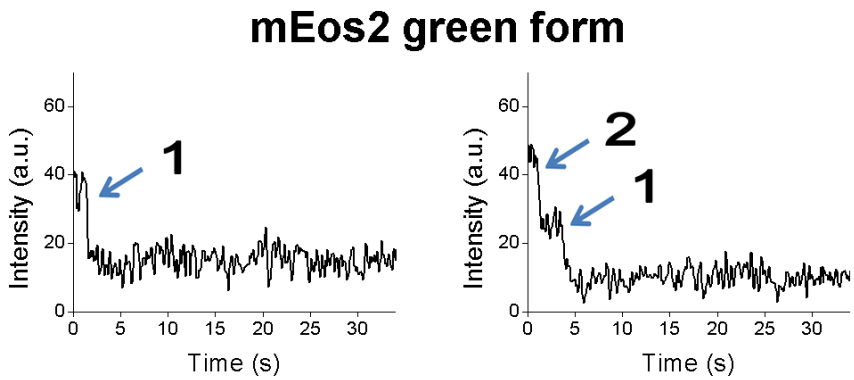

Figure 3.3. Intensity-time traces of the green form of mEos2 tagged to the GlyR β subunit. *Examples of single (left) and double (right) steps of mEos2 imaged with single-step photobleaching method. Counting the number of steps in each trace, a distribution of single and double steps can be extracted.*

From these traces, we could extract the number of steps. Our results showed that the counted number of single steps (n = 117 for mEos2, n = 160 for mEos3.2, n = 136 for mClavGR2, n=121 for mMaple and n = 144 for Dendra2) and double steps (n = 210 for mEos2, n = 149 for mEos3.2, n = 208 for mClavGR2, n = 170 for mMaple and n = 259 for Dendra2) fit well to a binomial distribution given that ~80 % of mEos2 or Dendra2 and ~75 % of mClavGR2 or mMaple is fluorescent in their native form in good agreement with other fluorescent protein variants (Durisic et al., 2012, Ulbrich and Isacoff, 2007). This number was slightly lower for the green form of mEos3.2

(65 %, n=160 single and n=149 double). Finally, the green form of mEos3.1 was less photostable than the other fluorescent proteins, making it hard to determine its photoactivity (Table3.1).

The next step was to determine the *in vivo* photoconversion kinetics of the FPs. We illuminated the sample with continuous 405nm light and we counted a cumulative number of detected proteins in each frame to ensure that all molecules were converted from green to red form. The cumulative curve of mEos2 reached a plateau after ~7 seconds of illumination at a 405nm laser power of 6.8 W/ cm^2. This result is in good agreement with the previously determined photoconversion kinetics for this fluorescent protein (Zhang et al., 2012). The cumulative curve of Dendra2 showed saturation after ~20 seconds of illumination with only 1.5 W/cm^2 of 405 nm laser (**Figure 3.4**).

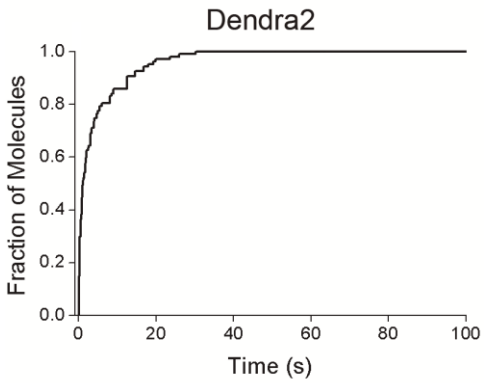

Figure 3.4. Cumulative curve of the photoconversion of Dendra2. *In single-step photobleaching, the photoconverted molecules of Dendra2, excited at 1.5 W/cm^2, reach a plateau after approximately 30 seconds. The cumulative number has been normalized by the maximum number of detected molecules at the end of the imaging session.*

To achieve varying levels of photoconversion, we illuminated the GlyRs labeled with mEos2 fused to the β-subunit for different illumination times with the laser power that gave the saturation point in the previous experiment (6.8W/ cm^2). The illumination times were from 2 to 12 seconds in jumps of 2 seconds. For each illumination time, we then imaged the photoconverted molecules with 560 nm laser until they photobleached.

Despite the fact that under some of these illumination conditions (i.e. ~7 seconds or longer) the majority of mEos2 should have photoconverted, the stepwise photobleaching data predominantly contained single steps. The fitting of the single (n = 50) and double (n = 33) steps to the binomial distribution showed that, at most, 57 % of mEos2 was fluorescent in the red form. Photoconversion times longer than 7 seconds showed a decrease in the percentage probably through photodamage of the red form of mEos2 after extended 405nm laser light (**Figure 3.5**).

To determine whether the incomplete photoconversion was due to uncleaved mEos2 remaining in the native state or to a dark population of newly formed mEos2, we checked the photobleaching behavior of the remaining GlyRs in the green channel. We were surprised to find that, for short enough illumination times, the remaining percentage of fluorescently detectable green mEos2, when added to red mEos2, brought the total percentage of fluorescently detectable mEos2 to nearly 100 % (**Figure 3.5**). Given that only 80 % of mEos2 is actually fluorescent in its native form, these results indicate that the dark native mEos2 can potentially also photoconvert. Further, the percentage of remaining green mEos2 reached a plateau at around 37 % and continued illumination from a 405-nm laser did not change this percentage (**Figure 3.5**). These results indicate that a subpopulation of native mEos2 is unable to photoconvert, which is consistent with previous *in vitro* studies that track the evolution of purified mEos2 absorption spectrum upon different times of 405-nm illumination (Annibale et al., 2012). They showed that the red form of mEos2 reaches a saturation before the green form has completely disappeared. Even after 50 minutes of 405 illumination, they still see high absorbance in the 488 nm band (Annibale et al., 2012).

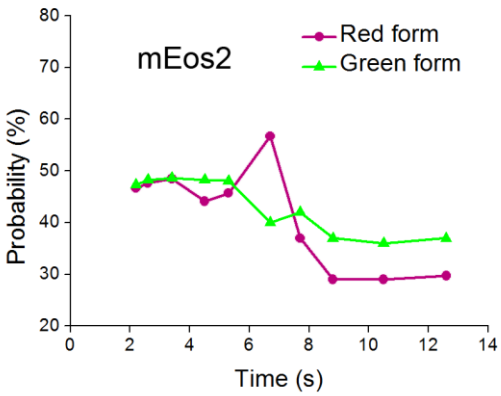

Figure 3.5. Probability of mEos2 determined from single-step photobleaching at different exposure times with 405 nm laser light. *The photoactivation of the red form of mEos2, in magenta, shows a peak of photoconversion at 7 seconds of exposure time. In green, the percentage of the remaining native form of mEos2 after different exposure times of 405 nm laser illumination is showed.*

It is possible that the incomplete photoconversion is due to the fact that some red mEos2 molecules photobleached during the 405-nm illumination before we could image them and thus never appeared in the traces. To rule out this possibility, we illuminated GlyRs with 405-nm and 560-nm lasers simultaneously and continuously and counted steps in the intensity-time traces. The counting of single and double steps gave us similar results (PE = 62 %, n = 159 single, n = 132 double steps).

We also did controls to rule out changes caused by fluctuations of temperature or pH of the buffer. We changed the buffer temperature to 37ºC, a standard temperature for mammalian cells, to see if the photoconversion of mEos2 was affected. We obtained a 60 % photoconversion following the same imaging procedures as the experiments with continuous 560nm illumination and 405nm illumination (n = 136 single and n = 102 double steps). In the case of pH, the resulting PE was 62 % at pH 5.6 (n = 83 single and n = 69 double steps) and 59 % at pH 8.5 (n = 71 single and n = 52 double steps). It is important to mention that the internal pH of the oocytes is self-regulated and the FPs were located in an intracellular loop of the GlyR subunit, which is cytoplasmic.

To circumvent this situation, we filled glass bottom dishes with buffer and briefly placed the oocytes on the glass surface. After the oocytes were removed, only a portion of the oocyte membrane containing some GlyRs remained in the dish, allowing exposure of the FPs to the buffer. This process is called patching. Then, we

changed the pH of the buffer and looked at the photoconversion. We also performed the same experiments with buffer at pH 6, 7.5 and 8.5. Nevertheless, these experiments showed that traces at pH 6 looked overall with lower number of photons compared to more basic buffers and with not very well-defined single steps, making the results difficult to interpret.

In addition to temperature and buffer pH, we measured how the 1 % paraformaldehyde (PFA) fixation of the oocyte may affect the PE. The results were 57 % PE for mEos2 (n = 67 single and n = 45 double steps), showing that fixation at this percentage does not cause any change in the photoconversion of the FP.

Finally, we checked how the PE of mEos2 may change depending on the subunit that it is tagged to. We performed single-step photobleaching experiments in oocytes with GlyR α-subunit tagged with mEos2 and, once again, the fitting to a binomial distribution for a trimeric stoichiometry did not show any change in the results (PE = 59 %; n = 14 triple steps, n = 31 double steps, n = 20 single steps, fitting extremely well to the binomial distribution for trimeric stoichiometry (χ^2 = 0.07886, P = 0.96) (**Figure 3.6**).

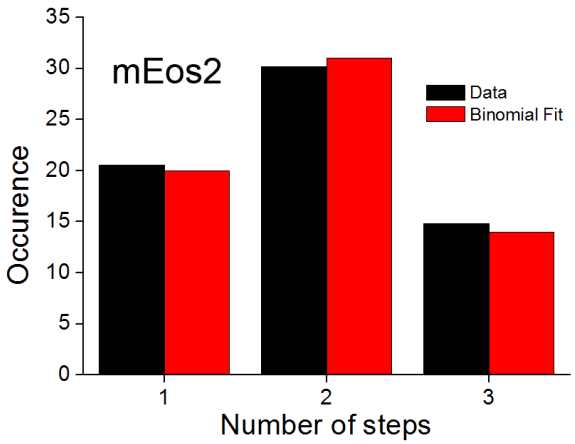

Figure 3.6. Binomial distribution for the α-subunit counted steps. *In black, the number of single, double and triple steps of the experimental data is represented, which gave a probability of 59 % and a fit goodness of X2 = 0.0789 or P= 0.96 in Chi-squared test. The red plot is the theoretical fit to a binomial distribution with 59 % of probability.*

Additionally, as a control to determine that the dimeric signal was due to the photobleaching of two molecules and not coming from an artifact, we tagged mEos2 to the α1E-Ca^{+2} channel. In this channel, all the subunits are connected into one polypeptide (Ulbrich and Isacoff, 2007), giving rise to only one fluorescent protein per channel. We performed the single-step photobleaching experiment as in the case of GlyR. As expected, the stepwise photobleaching of the α1E-Ca^{+2} after photoconversion predominantly (~96 %) showed single steps (46 single and 2 double steps for α1E-Ca^{+2} tagged with mEos2).

A final control was performed to determine if the conversion was depending on the linear polarization of the excitation and imaging light. Linear polarization can lead to inefficient excitation of the fluorescent proteins if the dipole moment of the fluorescent protein is not properly aligned with the polarization of the exciting light. We believe that laser polarization does not have an important role in these experiments for several reasons. The intracellular loop of the GlyR subunits where the FPs are tagged gives them enough freedom to rotate during an imaging session. Furthermore, the PE of mEos2 determined with single-step photobleaching is the same in living and fixed cells, indicating that fixation does not immobilize the FP. Nevertheless, to rule out polarization effects, we used a quarter-wave plate to change the polarization to circular, re-measured the PE of mEos2 and obtained very similar results with single-step photobleaching (PE = 65 %, n = 22 single and n = 20 double).

Once all the principal experiments and the controls to validate the method were used to characterize the PE of mEos2, we proceeded with the characterization of the PE for the other main FPs used in PALM studies. Following the same procedures as for mEos2, we determined the photoactivation efficiency of Dendra2 (PE = 54 %; n = 168 single, n = 100 double steps), mClavGR2 (PE = 56 %; n = 194 single, n = 121 double), mMaple (PE = 51 %; n = 427 single, n = 224 double steps) and the two

derivatives of mEos2, mEos3.1 (PE = 44 %; n = 244 single, n = 94 double) and mEos3.2 (PE = 42 %; n = 107 single, n = 38 double) (Table 3.1).

We also examined the remaining green Dendra2 and mClavGR2 after photoconversion. Dendra2 behaved similar to mEos2, with the green and red probability adding up to ~100 % and residual green molecules remaining even after extended illumination with the 405-nm laser. In the case of mClavGR2, the green and red probabilities only added up to ~84 %, and there were very few residual green molecules remaining. The low amount of remaining green mClavGR2 indicates either photodamage to the green chromophore with extended 405-nm illumination before photoconversion could occur or photoconversion of the green chromophore into a fluorescently undetectable form. We are unable to distinguish between these possibilities. **Figure 3.7** shows the graphs of the percentage of photoconverted proteins of Dendra2 (**Figure 3.7**a) and MClavGR2 (**Figure 3.7**b) and the remaining native green form.

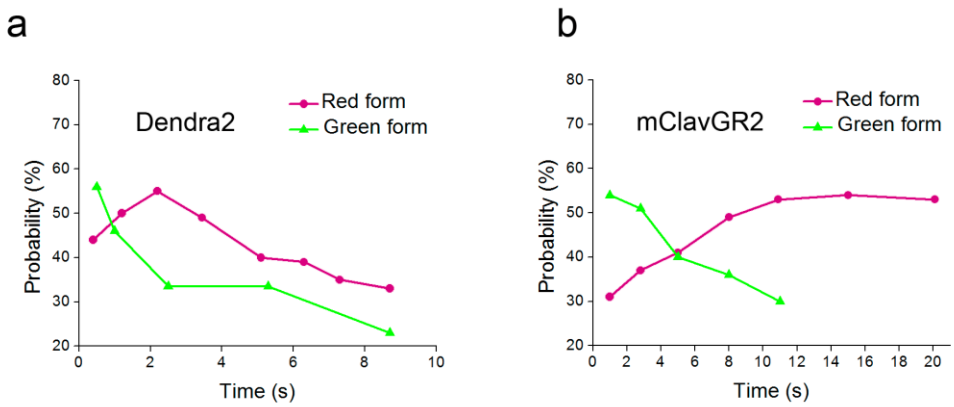

Figure 3.7. Single.-step photobleaching probability of Dendra2 and mClavGR2. *Probability of Dendra2 (left) and mClavGR2 (right) determined from single-step photobleaching at different exposure times with 405 nm laser light. The photoactivation of the red form is shown in magenta. In green, the percentage of the remaining native form of both Dendra2 and mClavGR2 after different exposure times of 405 nm laser illumination is showed.*

Table 3.1 shows a summary of the different PEs for each photoconvertible FP with all the experiments and controls combined into one value of PE.

Fluorescent Protein	Green Form (mean±s.d.)	PE 405 nm (mean±s.d.)	405 nm power density and illumination time
mEos2	**78±1 %**(*n* = 327)	**60±3 %**(*n* = 1106)	6.8 W/cm^2 for 6.7 s
mEos3.2	**65±2 %** (*n* = 309)	**42 %±9 %** (*n* = 145)	6.5 W/cm^2 for 6.3 s
mClavGR2	**75±2 %** (*n* = 344)	**56 %±1 %** (*n* = 315)	6.5 W/cm^2 for 15 s
mMaple	**74±4 %** (*n* = 291)	**51 %±2 %** (*n* = 651)	3.2 W/cm^2 for 3 s
Dendra2	**82±2 %** (*n* = 403)	**54±3 %** (*n* = 268)	1.5 W/cm^2 for 2.2 s

Table 3.1. Photoactivation efficiency of the photoconvertible FPs using single-step photobleaching. *The uncertainty reported is the s.d. calculated from different oocytes. n, total number of traces analyzed. The data are from a minimum of two oocytes obtained from different frogs and multiple fields of view per oocyte. Similar results were obtained for mEos3.1 as mEos3.2.*

3.3.2 Single-step photobleaching in photoactivatable fluorescent proteins

After the characterization of the most common photoconvertible FPs used in PALM, we continued with the photoactivatable FPs that are also widely used in super-resolution experiments: PA-GFP and PA-mCherry. In this case, the FPs have a dark native form and by excitation with laser light, they become fluorescent. PA-GFP is photoactivated from a dark state into bright green fluorescence (517 nm) upon 405- or 488-nm light illumination. We tagged the β-subunit of GlyR with PA-GFP and coexpressed it with mCherry-tagged α-subunit. These two FPs are spectrally very different, which avoids crosstalk when imaged together. The α-subunit tagged with mCherry was used for visualization since PA-GFP is dark before photoactivation. We first examined the PE after illumination with the 488-nm laser. PA-GFP was photoactivated with high efficiency (72 %) even with relatively low 488-nm laser

power (7.8 W/cm^2 for 130 s) (n = 557 single steps and n = 712 double steps). Similarly, illumination with 405- and 488-nm lasers photoactivated 85 % of the PA-GFP (n = 143 single steps and n = 393 double steps).

We similarly calculated the PE of PA-mCherry as for PA-GFP. We tagged PA-mCherry to the β-subunit together with Venus fluorescent protein (VFP) co-expressed with the α-subunit, again spectrally different from PA-mCherry. The fluorescence of the VFP was used as a localization of the GlyRs before imaging PA-mCherry in order to determine its photoactivation efficiency. The results gave a PE of 50 % for PA-mCherry (n = 224 single and n = 110 double steps).

Table 3.2 shows a summary of the different PEs for each photoactivatable FPs.

Fluorescent Protein	PE 405 nm (mean±s.d.)	PE 488 nm (mean±s.d.)	405 nm power density and illumination time	488 nm power density and illumination time
PA-GFP	**85 ±5 %** (*n* = 536)	**72 ±4 %** (*n* = 1269)	0.4 W/cm^2 for 140 s	7.8W/cm^2 for 130 s
PA-mCherry	**50 ±3 %** (*n* = 334)	NA	6.8 W/cm^2 for 2.2 s	NA

Table 3.2. Photoactivation efficiency of the photoactivatable FPs using single-step photobleaching method. *The uncertainty reported is the s.d. calculated from different oocytes. n, total number of traces analyzed. The data are from a minimum of two oocytes obtained from different frogs and multiple fields of view per oocyte. NA, not applicable.*

3.4. Single-molecule-counting PALM

As an alternative to single-step photobleaching for measuring the PE we used single-molecule-counting PALM. This method is used to determine protein stoichiometry when single-step photobleaching is not feasible (such as when there is a high density of proteins) (Gunzenhäuser et al., 2012, Lando et al., 2012, Lee et al., 2012, Renz et al., 2012). Fluorescent proteins are photoactivated one at a time by an incremental increase of the photoactivation laser power over time. An imaging laser at high

power is used to excite and subsequently photobleach the photoactivated fluorescent proteins (**Figure 3.8**). The number of imaged fluorescent proteins should ideally correspond to the number of actual proteins. For this concept to work, several conditions must be satisfied: (i) fluorescent proteins must be photoactivated slowly to prevent simultaneous activation of multiple molecules within a diffraction limited volume, (ii) all fluorescent proteins must be exhaustively activated and detected during the imaging, (iii) blinking (or reactivation of the same fluorescent protein) must be accounted for and (iv) the PE must be precisely known. Imaging schemes have been proposed for controlled photoactivation of fluorescent proteins (Gunzenhäuser et al., 2012, Lee et al., 2012). Furthermore, the cumulative number of fluorescent proteins detected in each frame has been used to determine whether the fluorescent proteins have been exhaustively imaged (Gunzenhäuser et al., 2012). The cumulative plot has an initial rise that reaches a plateau once the majority of fluorescent proteins have been detected. Finally, the fluorescence off times have been used to determine a cutoff time to separate blinking (or reactivation) from photoactivation of a new fluorescent protein (Lee et al., 2012, Annibale et al., 2011b). Typically, the blinking time is short compared to the photoactivation time, particularly when the protein density is low and a sparse photoactivation regime is followed. Therefore, a plot of fluorescence off times can be used to set a cutoff time and peaks that appear during shorter time intervals can be linked together as belonging to the same fluorescent protein (**Figure 3.8**). Here, we followed these steps to count the number of peaks in the PALM intensity-time traces for β- or α-subunit of single GlyRs and fitted the counted number of peaks to the binomial distribution to determine the PE using this alternative approach (**Figure 3.8**)

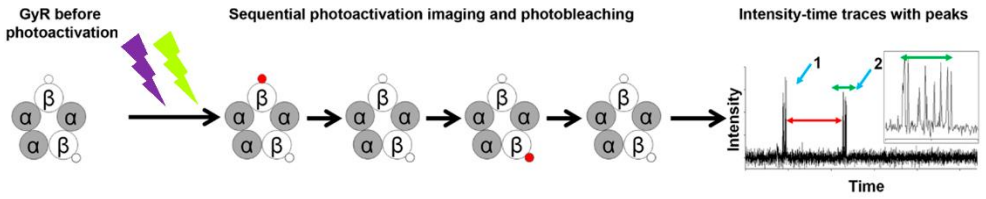

Figure 3.8. Single-molecule-counting PALM scheme. *GlyRs are expressed in* Xenopus *oocytes as in single-step photobleaching. Fluorescent proteins are sequentially photoactivated, detected and photobleached. Intensity-time traces are used to count the number of peaks. Peaks with short off times (green arrow and inset) are linked together as one peak. Peaks with long off times (red arrow) are counted as new photoactivation events.*

Once again, we tagged the β-subunit of the GlyR with one FP at a time and in this case, we also tagged the α-subunit with a non photoswitchable FP to be able to mark the GlyRs before the PALM experiment. It was essential that the 2 FPs had a clear separated spectrum of absorption and emission to avoid crosstalk. We first took an image of the regular FP and then we proceeded with the imaging of the β-subunit. After acquisition, we obtained a distribution of traces with one peak or two peaks and we could then determine the number of dark proteins and the photoswitching efficiency by fitting the numbers to a binomial distribution, as used before.

3.4.1 Single-molecule-counting PALM in photoconvertible fluorescent proteins

We coexpressed photoconvertible fluorescent protein tagged β-subunits and mCherry tagged α-subunits and lightly fixed the oocytes at a time point of low GlyR density. We first imaged and completely photobleached mCherry and subsequently carried out the PALM experiment. We then overlapped the mCherry image with the maximum intensity projection of the PALM time sequence (**Figure 3.9**).

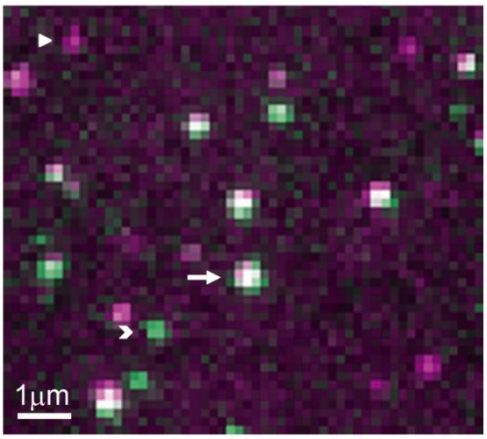

Figure 3.9. mCherry-mEos2 overlap. *Image showing the overlap between mCherry-tagged α-subunit (magenta) and the maximum intensity projection of the single-molecule-counting PALM sequence of mEos2-tagged β-subunit (green). The GlyRs that appear in both channels (arrow) are used for further analysis while the mCherry alone (full arrowhead) and mEos2 alone (empty arrowhead) spots are discarded from the analysis.*

Some GlyRs that appeared in the mCherry image did not have a partner in the PALM image (**Figure 3.9**). These spots could be due to homomeric GlyRs or GlyRs whose photoconversion completely failed. Similarly, there were some spots that appeared in the PALM image without a partner in the mCherry image (**Figure 3.9**). These spots could be due to false positives or a new GlyR that became incorporated into the membrane during the PALM imaging, as the light fixation did not completely eliminate GlyR transport. Overall, ~60 % of GlyRs that appeared in the mCherry image had a corresponding partner in the PALM image (**Figure 3.9**). We selected a subset of these GlyRs (30–40 %) for further analysis avoiding ones with elongated point spread function or partially overlapping GlyRs. In the absence of mEos2 there was very little overlap (<4 %) between the mCherry image and the PALM image, ruling out resurrected mCherry contributing to the signal in PALM (**Figure 3.10**).

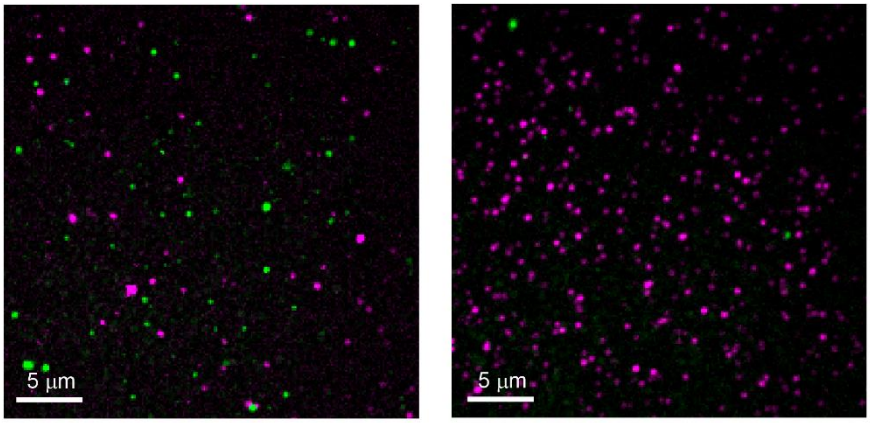

Figure 3.10. Control experiment with untagged β and mCherry tagged α-subunit. Images show the overlap between mCherry-tagged α-subunit (magenta) and the maximum intensity projection of the PALM sequence for untagged β-subunit (green) immediately after fixation (left) and 1 hour after fixation (right).

We first plotted a cumulative curve of the number of molecules detected in each frame of the PALM image for all the photoconvertible FPs under consideration (**Figure 3.11**), which reached a plateau confirming that we exhaustively imaged the majority of fluorescent proteins.

We next plotted intensity-time traces from the PALM time sequence. These traces typically showed single or double "peak clusters" (**Figure 3.12**). The closely spaced peaks in these traces are probably due to the same fluorescent protein reappearing multiple times after photoactivation. We refer to this behavior, in which a fluorescent protein returns from a dark state with a short off time, as "blinking".

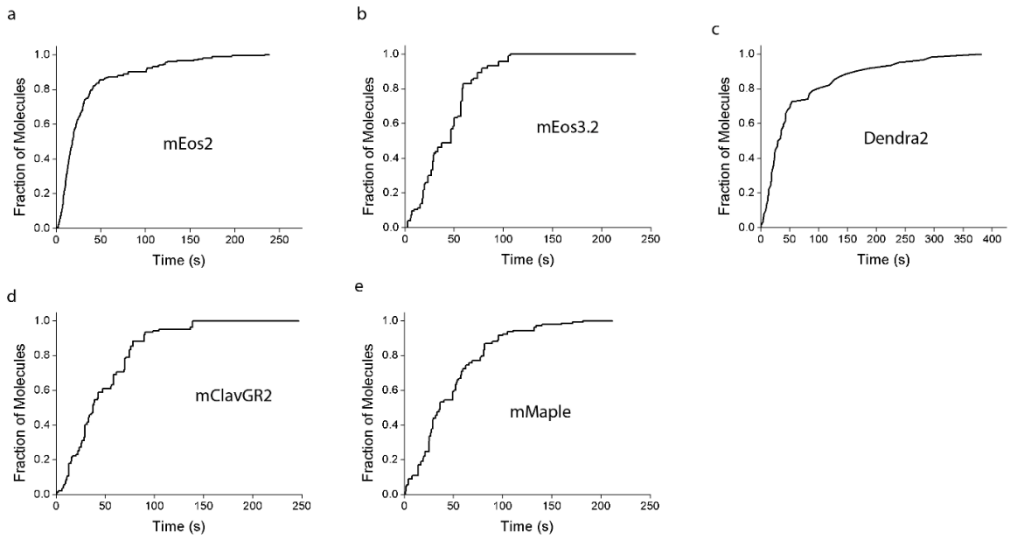

Figure 3.11. Cumulative curves of single-molecule-counting PALM. *Cumulative curves of mEos2 (a), mEos3.2 (b), Dendra2 (c), mClavGR2 (d) and mMaple (e). Similar results were obtained for mEos3.1 as mEos3.2. The cumulative plots have been normalized to the total number of detected molecules in each case. After a certain time, they all show a plateau towards the end of the imaging session, therefore, the majority of fluorescent molecules that could photoconvert have been exhaustively imaged.*

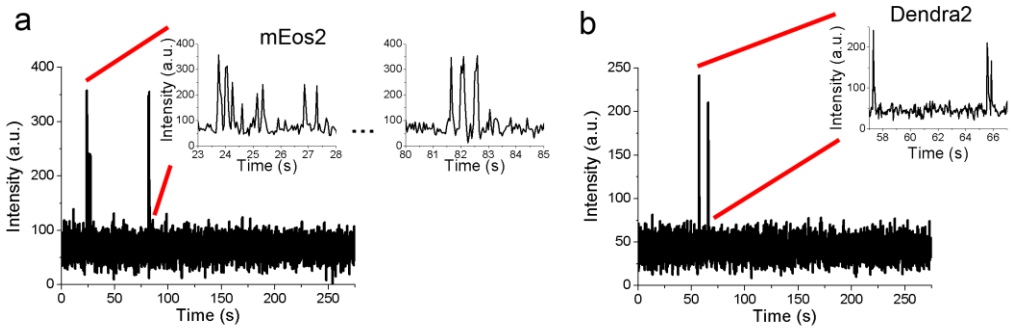

Figure 3.12. Intensity-time traces of single-molecule-counting PALM. *Examples for mEos2 (a) and Dendra2 (b) using single-molecule-counting PALM. These traces show how in the case of mEos2 there is a considerable reactivation of the same molecule. Peaks separated by short off-times are grouped as one (inset), whereas peaks separated by long times are counted as differentiated peaks. In the case of Dendra2, the blinking is minimal, but the same grouping by time between peaks is used to count the number of FPs. a.u., correspond to arbitrary units.*

We determined the blinking kinetics by counting the percentage of molecules that showed blinking and the number of times that each molecule blinked on average

(**Table 3.3**). After extracting the off times from the different intensity-time traces, we plotted the distributions and fitted it to a single exponential. **Figure 3.13** shows the distribution obtained from the mEos2 experiments.

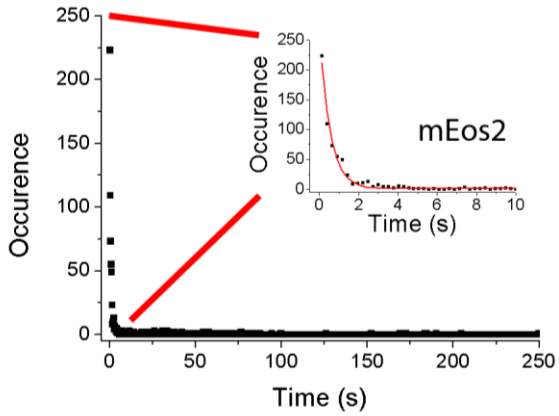

Figure 3.13: Distribution of fluorescence off-times in PALM traces of mEos2 tagged in β-subunit. *The experimental data is represented by black squares whereas the red line corresponds to a fit of the data to an exponential decay. The time where the distribution decayed at 99.8 % was used as the cutoff time (4.1 seconds) to group peaks together. If their separation time was shorter than this cutoff time, they were considered to belong to the same FP.*

The short times that dominate the distribution are probably due to blinking, whereas the long tail comes from activation of a new fluorescent protein. We set a cutoff time corresponding to the time in which the exponential decayed to 99.8 % of its initial value to account for the majority of blinking events. This cutoff time was 4.1 s for mEos2 and 1.6 s for Dendra2, consistent with previous cutoff times used for these fluorescent proteins (Lee et al., 2012). **Table 3.3** show a summary of all the cutoff times for the different photoconvertible FPs.

Fluorescent Protein	Molecules that blinked (%)	Average # of times a molecule blinked	Cut-off time (s)
mEos2	58	2.8	4.1
mEos3.2	50	2.4	3
mClavGR2	49	3	1.9
mMaple	49	3.4	2.6
Dendra2	30	2.7	1.6

Table 3.3. Blinking kinetics and cutoff times used in single-molecule-counting PALM in photoconvertible FPs.

We linked together peaks with off times smaller than or equal to the cutoff time. After this step, the majority of traces (85–89 %) contained single or double peaks and discarded the small percentage of traces with more than two peaks. These traces were partially due to overlapping GlyRs (4 %) and partially due to potential reactivation of the same fluorescent protein after a long off time (7–10 %) (Annibale et al., 2010).

As a control for the reactivation, we tagged again the monomeric α1E-Ca^{+2} with mEos2 and performed the PALM experiment. The results showed that ~15 % of the traces gave more than one peak.

Finally, after all the previous considerations, we fitted the counted number of single (n = 83 for mEos2, n = 100 for mEos3.2, n = 117 for mClavGR2, n = 84 for mMaple and n = 107 for Dendra2) and double (n = 72 for mEos2 , n = 35 for mEos3.2, n = 67 for mClavGR2, n = 50 for mMaple and n = 50 for Dendra2) peaks to the binomial distribution and obtained a similar photoactivation efficiency as determined from single-step photobleaching (63 % for mEos2, 41 % for mEos3.2, 53 % for mClavGR2, 54 % for mMaple and 48 % for Dendra2). **Table 3.4** summarizes all the PEs obtained.

	Photoactivation efficiency (mean±s.d.)
mEos2	**61±2 %** (*n* = 292)
mEos3.2	**41±4 %** (*n* = 135)
mClavGR2	**53±8 %** (*n* = 184)
mMaple	**54±3 %** (*n* = 134)
Dendra2	**48±1 %** (*n* = 157)

Table 3.4. Photoactivation efficiency of photoconvertible FPs using single-molecule-counting PALM. *The uncertainty reported is the s.d. calculated from different oocytes. n, total number of traces analyzed. The data are from a minimum of two oocytes obtained from different frogs and multiple fields of view per oocyte. Similar results were obtained for mEos3.1 as mEos3.2.*

3.4.2 Single-molecule-counting PALM in photoactivatable fluorescent proteins

Following the steps of single-step photobleaching, we also characterized the PE of photoactivatable fluorescent proteins using single-molecule-counting PALM. We tagged the α-subunit with mCherry and the β-subunit with PA-GFP. We first photobleached the mCherry and used this image to localize the GlyRs that overlapped with the image of the β-subunit.

Laser illumination at 488 nm is needed for imaging PA-GFP but this wavelength also photoactivates PA-GFP, making it impossible to decouple photoactivation from imaging. We therefore started the PALM imaging with 488 nm laser alone. We used 488 nm power that was high enough (~162 W/cm^2) to quickly photobleach the PA-GFP molecules once they become photoactivated, typical for PALM. However, high power rapidly and simultaneously photoactivated a high amount of PA-GFP. The cumulative fraction of PA-GFP detected in each frame during PALM showed a sharp rise that quickly reached a plateau, confirming that most of the PA-GFP was photoactivated within the first 10 s of PALM imaging (**Figure 3.14**). Therefore, the likelihood of simultaneously photoactivating both PA-GFPs on the same GlyR was high. Consistent with this observation, we found a low PE for PA-GFP (39 %, n = 99 single peaks and n = 31 double peaks) without setting any cutoff time.

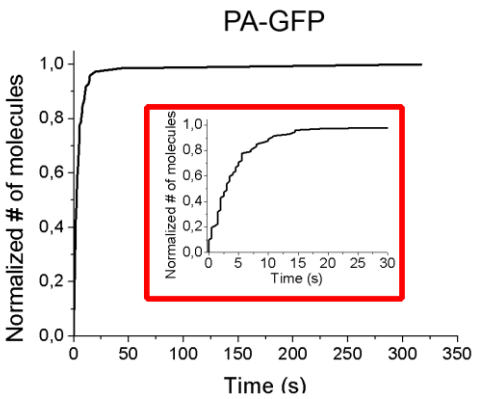

Figure 3.14: Cumulative curve of PA-GFP new photoactivated molecules per frame. *Curve showing the detected number of PA-GFP molecules in an imaging session with 488 nm laser power of 162 W/cm^2. The cumulative number has been normalized to the total number of detected molecules. Inset, blow-up of the first 30 seconds of the cumulative curve, showing the rapid photoactivation of molecules with 488 nm laser illumination alone.*

Since single-step photobleaching showed high photoactivation efficiency, this result was likely due to both PA-GFPs within the same GlyR being photoactivated simultaneously and thus undercounted.

We next carried out single-molecule-counting PALM experiments in oocytes tagged with PA-mCherry in the GlyR β-subunit and VFP in the α-subunit. In this case, VFP was the protein to be used to localize the GlyRs, as we did before with mCherry. The extracted intensity-time traces showed a majority of single and double peaks with only 15 % of the traces showed two peaks, therefore setting a cutoff time was not necessary, as blinking could easily be distinguished from photoactivation.

The PA-mCherry photoactivation efficiency determined in this way was 41 % (n = 60 single and n = 21 double peaks). Finally, tagging the α-subunit with PA-mCherry, counting the number of traces that contained triple (n = 9), double (n = 19) and single (n = 22) peaks and fitting to the binomial distribution for three subunits gave a probability of 49 % with $\chi^2 = 0.9998$ (P = 0.60) for the binomial fit.

Table 3.5 shows the PEs for both FPs analyzed in this chapter. In the case of PA-mCherry, the given percentage is an average between experiments of α- and β -subunits.

	PE (mean±s.d.)
PA-GFP	**39±6 %** (*n* = 130)
PA-mCherry	**45±6 %** (*n* = 131)

Table 3.5. Photoactivation efficiency of photoactivatable FPs using single-molecule-counting PALM. *The uncertainty reported is the s.d. calculated from different oocytes. n, total number of traces analyzed. The data are from a minimum of two oocytes obtained from different frogs and multiple fields of view per oocyte.*

3.5 Single-step photobleaching to determine ion channel subunit stoichiometry

As a collaboration with Dr Raúl Estévez, from Universitat de Barcelona, we also used single-step photobleaching to characterize the protein stoichiometry of LRRC8, a protein present in volume-regulated anion channels (VRAC) (Gaitán-Peñas et al., 2016).

Cells regulate their volume through expression of water channels called aquaporins. Changes in cell volume trigger regulatory mechanisms involving different osmotic transporters and ion channels that help to restore the original size. These channels control the cell volume by opening upon cell swelling. They consist of heteromers of LRRC8A combined with other LRRC8 subunits, such as B, C, D and E (Qiu et al., 2014, Voss et al., 2014). The stoichiometry of the subunits in this channel affects different processes such as channel inactivation (Ullrich et al., 2016) by depolarization , substrate specificity (Planells-Cases et al., 2015, Voss et al., 2014) or single-channel conductance (Syeda et al., 2016), however, the specific composition of the LRRC8 subunits in the VRACs remained unknown.

To determine the subunit stoichiometry of LRRC8, we transfected the *Xenopus* oocytes with an equimolar amount of LRRC8A subunits tagged with VFP and one of the other LRRC8 subunits (B-E) tagged with mCherry, since it is spectrally different from VFP. The image of the subunit tagged with mCherry was used as a locator for the VRACs and the one tagged with VFP was used to count the steps. We took the overlapping spots in both images and once again, we excluded spots that were fluorescent for only one frame and multiple partially overlapping ones in the same region of interest (**Figure 3.15**).

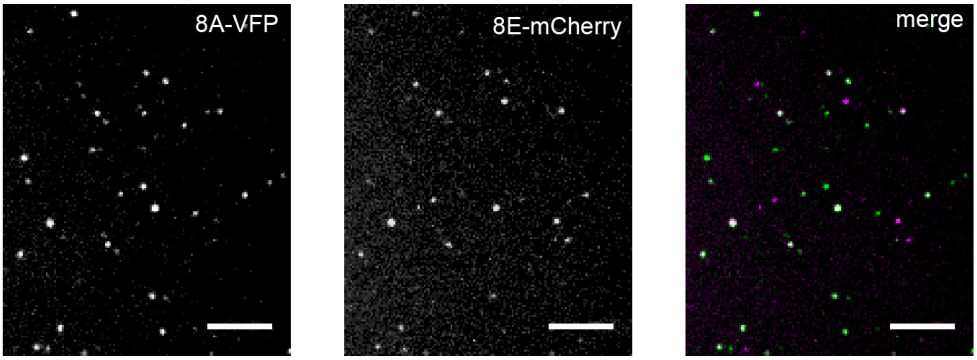

Figure 3.15. 8A-VFP – 8E-mCherry overlap. *TIRF image showing LRRC8A-VFP and LRRC8EmCherry oligomers on the* Xenopus *oocyte membrane and a merge of the two fluorescent channels. Arrowheads point to overlapping LRRC8A and LRRC8E spots. Scale bar: 5 µm.*

We then extracted the intensity-time traces for each of the overlapping spots and counted the number of steps (**Figure 3.16**).

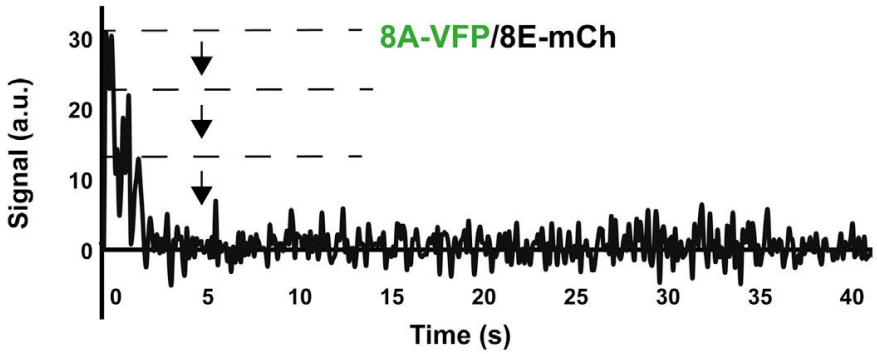

Figure 3.16. Intensity-time trace of 8A-VFP. *Subunit counting of LRRC8 heteromers by single-step photobleaching. Intensity-time traces showing individual photobleaching steps from one of the LRRC8A-VFP oligomers in complex with LRRC8E-mCherry identified on the oocyte membrane in TIRF microscopy. Dashed lines and arrows indicate observed single steps.*

The extraction of the intensity-time traces revealed a broad distribution of steps ranging from 1 to 6 steps (**Figure 3.17**).

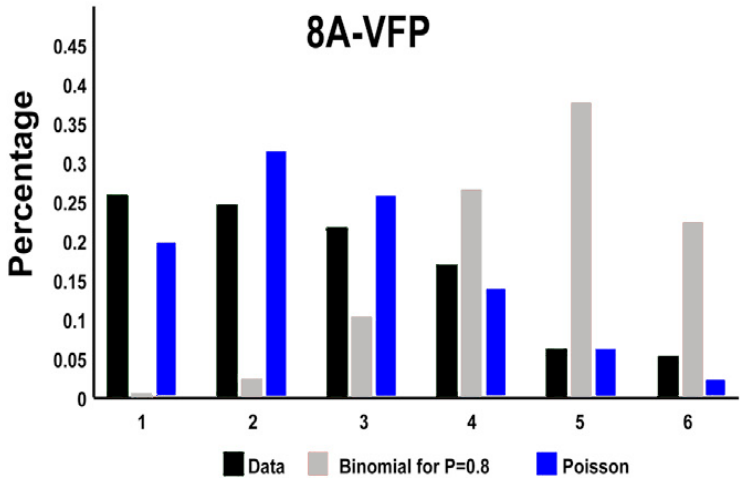

Figure 3.17. Distribution of the percentage of counted steps from LRRC8A-VFP oligomers in complex with LRRC8E-mCherry oligomers at equimolar ratio. *Black bars indicate the data, grey bars show the prediction of a binomial distribution with P = 0.8 (See methods for the corresponding equation) and blue bars indicate the best fits of Poisson distribution. N = 142*

This broad distribution is not compatible with a binomial distribution assuming 80 % probability for VFP to be fluorescent and a fixed stoichiometry ranging from 1 to 6. Instead, the fitting of the data gave a closer agreement with a Poisson distribution with 1 to 6 subunits. The average of the Poisson distribution for the LRRC8A subunit was 3. We also performed counting experiments to determine the stoichiometry of LRRC8E subunits. We again coexpressed LRRC8A and LRRC8E in *Xenopus* oocytes, but then inverted the tagged FPs and performed the same counting measurements for LRRC8E as for LRRC8A, using again the VFP signal. In this case, we also obtained a distribution of steps ranging from 1 to 6 steps. The fitting of the steps to the Poisson distribution gave an average of 2.5 LRRC8E subunits. Our results suggest that the heteromer composition depends on the relative expression of the different subunits and that the number of total subunits is higher than 5. The detailed results of this study can be found in (Gaitán-Peñas et al., 2016).

3.6. Discussion and conclusions

Quantitative measurements are clearly possible using single molecule localization techniques. However, it is essential that the probes to be used are extensively calibrated to avoid artifacts that would invalidate the final results. In the case of PALM, the photoactivation behavior of the fluorescent proteins needs to be well understood to perform such experiments. The characterization of *in vivo* photoswitching efficiency of the 8 most common fluorescent proteins used in PALM at the single-molecule level carried out in this chapter provides valuable information needed to use these FPs in the quantitative super-resolution experiments. We would like to emphasize that the results obtained with single-step photobleaching give the highest percentage of PE that can be achieved in PALM experiments. However, depending on the experimental conditions, other factors such as background, threshold for detecting peaks or inability to decouple photoactivation from imaging may further limit the percentage of detected fluorescent protein in PALM. In our observations, we found that PA-GFP was photoactivated with the highest efficiency, but the 488-nm imaging laser induced substantial photoactivation, making it difficult to control activation times and decreasing the detected percentage of fluorescent protein in single-molecule-counting PALM. Alternative imaging strategies with very low imaging-laser power may be used to overcome this problem at the expense of additional time to photobleach the photoactivated molecules.

Additionally, we showed that a subpopulation of mEos2 and Dendra2 are resistant to photoconversion. Previous results suggested that excited-state proton transfer has an important role in photoconversion (Wiedenmann et al., 2004) and thus the non-photoconverting molecules may lack the favorable protonation of the native chromophore. It was recently observed by PALM imaging, blinking correction and binomial statistics, that ~60 % of a membrane-localized mEos2 expressed at low levels in yeast was detectable (Puchner et al., 2013). This is in excellent agreement

with our results, indicating that fluorescent protein photoactivation efficiency does not depend on the fusion partner or expression system used.

Our experiments also showed a high blinking rate for mEos2. This can be problematic in densely labeled samples, as the increased frequency of photoactivation obscures the temporal separation between blinking and photoactivation (Lee et al., 2012). A way to overcome these limitations is using alternative methods, such as pair correlation analysis (Sengupta et al., 2011, Sengupta et al., 2013). These methods do not rely on defined cutoff times and therefore it may be preferable for quantifying super-resolution data with mEos2. Additionally, we observed that PA-mCherry and Dendra2 showed moderate photoactivation and lower blinking rates. Despite their lower PE than mEos2, these two FPs might be a reasonable choice for quantitative super-resolution analysis.

As we have observed, when the stoichiometry is unknown but conserved, it should be possible to distinguish among monomeric, dimeric and trimeric stoichiometry using these fluorescent proteins. Although we focused here on single molecule counting, photoactivation efficiency has other important implications. As an example, we could corroborate that a percentage of the labeled structure of the GlyRs was completely undetected. Finally, quantification of protein co-localization in multi-color experiments is also affected by the photoactivation efficiency.

It is important to note that the characterization methods we describe here are not limited to GlyR expressed in *Xenopus* oocytes but can be easily adapted to any protein complex with a well-defined stoichiometry or tandem repeats of fluorescent proteins expressed in any system.

Methods

Constructs

The plasmid, pT7 GlyR-β-VFP was used to perform plasmid constructions with the fusion proteins of glycine receptor β-subunit and the different fluorescent proteins in play.

8 plasmids were constructed where each of GlyR β-subunit contained one of the eight fluorescent proteins (mEos2, mEos3.2, mEos3.1, mClavGR2, mMaple, Dendra2 PA-GFP and PA-mCherry). Further details of the fusion process can be found in (Durisic et al., 2014b).

All the plasmids constructed were verified by direct sequencing to ensure the right orientation of the insert, the consistency of the whole sequence of the fragment amplified by PCR and the preservation of the reading frame in the joints in both ends of the fluorescent protein insertion. The GlyR α-subunit containing mCherry, mEos2 and PA-mCherry was generated in a similar way from GlyR-α-VFP.

Cloning was performed to remove the original mEGFP in the α1E-Ca+2 channel (pGEMHE-α1E Ca+2-mEGFP) and replace it with mEos2 or PA-mCherry. The fluorescent proteins were amplified using PCR using modified primers with SpeI restriction sites. α1E-Ca+2-mEGFP plasmid was digested with this restriction enzyme to remove mEGFP, the digested plasmid was dephoshorilated with CIAP and the SpeI-digested PCR products were ligated. The resulting plasmids were verified by direct sequencing.

For the LRRC8 subunits study, plasmids were constructed using standard molecular biology techniques employing recombinant polymerase chain reaction and the Multisite Gateway system (Invitrogen, Carlsbad, CA). The integrity of all constructs was confirmed by DNA sequencing.

Expression in *Xenopus* oocytes

The pT7-GlyR cDNA constructs were linearized with restriction enzymes and capped cRNAs were transcribed with the mMESSAGE mMACHINE T7 kit (Life technologies). Synthesized cRNAs were recovered by LiCl precipitation and resuspended in nuclease-free water at a final concentration of 0.5–1.0 μg/μL. The pT7-calciumcDNA constructs were linearized with NheI restriction enzyme. The rest of the steps of RNA synthesis were the same as for pT7-GlyR.

The harvesting of Xenopus oocytes from mature female Xenopus laevis was performed according to standard procedures and maintained at 17-20ºC in ND96 solution (96 mM NaCl, 2 mM KCl, 1.8 mM CaCl2, 1 mM MgCl2, 5 mM HEPES, pH 7.5)(Goldin, 1992). Oocytes were injected with 40 nL of cRNA using the Nanoject system (Drummond Scientific) and FemtoJet system (Eppendorf) and incubated for 12–20 hours prior to photobleaching or PALM experiments. The β-subunit RNA was injected at a concentration 5-10-fold higher than the α-subunit RNA. Since β-subunits do not form homomeric channels or do not insert into the membrane as monomers, this injection strategy was used to bias the expression towards heteromeric channels(Durisic et al., 2012). For single step photobleaching experiments, vitelline envelope and extracellular matrix were removed by incubating the oocytes in 0.05 mg/mL proteinase K (Roche Applied Science) for 5–6 min immediately before the experiment(Wang, 2004). The oocytes were then allowed to settle on the surface of a chambered coverglass prior to microscopy. For single molecule counting-PALM experiments, oocytes were fixed with 1 % paraformaldehyde (PFA) for 30 minutes after removal of the vitelline envelope and prior to imaging. This light fixation did not completely stop GlyR transport from the endoplasmic reticulum (ER), however higher PFA concentrations or longer incubation times with PFA lead to a decreased integrity of the oocyte and crosslinking of multiple GlyR channels and therefore could not be used. The imaging

was carried out in the ND96 solution, at pH 7.5 and at room temperature unless otherwise stated in the text.

In the case of the LRRC8 subunits project, the expression in *Xenopus* oocytes was performed after linearization by NotI and complementary RNA (cRNA) of human LRRC8 proteins was transcribed using the mMessage mMachine SP6 kit (Ambion, Waltham, MA). We produced cRNA of LRRC8A/E constructs and hLRRC8A/E-VFP and hLRRC8A/E-monomeric Cherry (mCherry) fluorescent constructs. They were expressed by themselves or coexpressed mainly with LRRC8A or LRRC8A-VFP.

Single step photobleaching and single molecule counting PALM experiments

Images were acquired on a custom-built total internal reflection fluorescence (TIRF) microscope with an Olympus IX71 inverted microscope frame fitted with a 100x 1.4 NA oil-immersion objective. Excitation light at 488 nm from an Argon-Krypton laser (Coherent Inc) was used to excite the native form of mEos2, mEos3.1, mEos 3.2, mClavGR2, mMaple and Dendra2 as well as the photoactivated form of PA-GFP in TIRF mode. Excitation light at 560 nm from a fiber laser (MPB Communications) was used to excite the photoactivated form of PA-mCherry or the photoconverted form of mEos2, mEos3.1, mEos3.2, mClavGR2, mMaple and Dendra2 in TIRF mode. Excitation light from a 405 nm solid state laser (Cube, Coherent Inc) was used to photoactivate all eight fluorescent proteins in TIRF mode. The emission of native mEos2, mEos3.1, mEos3.2, mClavGR2, mMaple, Dendra2 and photoactivated PA-GFP was collected with a BP 525/50 emission filter (Chroma Technology) and that of photoconverted mEos2, mEos3.1, mEos3.2, mClavGR2, mMaple, Dendra2 and photoactivated PA-mCherry was collected with BP 605/52 (Chroma Technology). The fluorescence emission was recorded onto an EMCCD camera (pixel size 157 nm) (Andor Technology) with an exposure time of 100 ms per frame for single step photobleaching experiments and 50 ms per frame for single molecule counting-

PALM experiments. For single step photobleaching experiments, fluorescent proteins were photoactivated (or photoconverted) by exposing them to the photoactivation laser at varying powers and durations (as indicated in the manuscript). The single step photobleaching was then achieved by exposing PA-GFP to 488 nm laser light at 7.8 W/cm^2, PA-mCherry to 560 nm laser light at 9.7 W/cm^2, mEos2 to 488 nm or 560 nm laser light at 4 W/cm^2 and 9.7 W/cm^2, mEos3.1 and mEos3.2 to 488 nm or 560 nm laser light at 11 W/cm^2, mClavGR2 to 488 nm or 560 nm laser light at 11 W/cm^2 and 16 W/cm^2, mMaple to 488 nm or 560 nm laser light at 5.5 W/cm^2 and 13 W/cm^2, and finally Dendra2 to 488 nm or 560 nm laser light at 4 W/cm^2 and 17 W/cm^2. For single molecule counting-PALM, mEos2, mEos3.2, mClavGR2, mMaple and PA-mCherry were photoactivated over time by illuminating the sample with 405 nm laser for 50 ms every 0.5 s. For mEos2, mEos3.2, mClavGR2, mMaple and PA-mCherry, the laser power was increased in small increments every 10 s and followed a sigmoidal rise during the first 6 min until the power reached 9.5 W/cm^2. The 405 nm power was then kept constant until the end of the measurement. Dendra2 was photoactivated following the same procedure, except the maximum 405 nm power was lowered to 5.4 W/cm^2. These fluorescent proteins were simultaneously imaged and photobleached by exposure to 560 nm laser at 1 k W/cm^2. PA-GFP was simultaneously photoactivated, imaged and photobleached by exposure to 488 nm laser at 162 W/cm^2. Data acquisition in PALM experiments typically lasted for ~10 min.

Data Analysis

Single step photobleaching

A square region of 3×3 pixels around the center of each spot was chosen to extract intensity-time traces using custom written MatLab software(Heyes et al., 2007). Background was subtracted locally by considering the average intensity of a 2X2

pixel region surrounding the molecule of interest. We excluded from our analysis: spots that moved by more than one pixel before they photobleached, spots that were fluorescent for only 1 frame and multiple partially overlapping spots. The steps in intensity-time traces were counted manually. Photobleaching steps were identified manually and defined as events in which the mean intensity of the smallest step was at least twice the standard deviation of the background fluorescence. We corrected for missed events in which both fluorescent proteins photobleached simultaneously as previously described (Durisic et al., 2012). Briefly, we calculated the photon distribution of single fluorescent proteins from traces that contained two photobleaching steps and characterized traces containing a single step size larger than twice the mean of this distribution as missed events. To determine the reliability of manual counting and the number of traces needed for a confident determination of the photoactivation efficiency, we used computer simulated traces taking into account the fluorescent protein photophysics such as signal to noise ratio, blinking and photobleaching kinetics.

When the subunit stoichiometry of the receptor is constant, the observed distribution of steps should follow the binomial distribution given by:

$$q_n = \left(\frac{M!}{n!\,(M-n)!}\right) P_f{}^n (1-P_f)^{M-n}$$

where, q_n is the probability to observe n steps in a time trace, M is the total number of subunits, n is the observed number of steps, P_f is the probability for the fluorescent protein to be fluorescent (or photoactivation efficiency in the text). For two subunits the above expression reduces to a series of three equations: $q_2 = P_f{}^2$ (probability for two steps), $q_1 = 2\,P_f(1-P_f)$ (probability for one step) and $q_0 = (1-P_f)^2$ (probability for completely dark channels). The probability, P_f, for the fluorescent

protein to be fluorescent can be estimated by directly fitting the observed number of steps to the above equation.

Single molecule counting-PALM

PALM traces were extracted in the same way as the single step photobleaching traces. A threshold for the average intensity was set as 4-6 times the standard deviation of the background fluorescence and events in the traces that were above this threshold were identified as peaks. Typically each peak lasted for one or two frames. The fluorescence off-times were determined as the time after the intensity of one peak decayed to the background level and the next peak appeared above the intensity threshold. Fluorescence off-times were fit to an exponential and a cut-off time was set as the time in which the exponential decayed to 99.8 % of its initial value. Peaks with off-times shorter than or equal to this cut-off time were then linked together.

In a few cases the oocyte membrane disintegrated due to increased sensitivity to proteinase K digestion as evidenced by highly fluorescent background appearing as the yolk leaked out. These oocytes were not used for imaging or data analysis. Finally, in a few cases the photoactivation during PALM imaging completely failed as evidenced by very low overlap of detected spots in PALM with the mCherry image as well as very low coincidence between the activating light pulse and the appearance time of fluorescence spots in the PALM movie. These samples were excluded from the analysis.

Simulations of photobleaching traces

A Monte Carlo method was used for simulating traces as follows. The fluorescence signal from all fluorophores was calculated as a function of time and as time was incremented a comparison was made between a random number and a simulation

parameter to determine if a certain event happened. The simulation parameters that we used for the comparison were the probability for the fluorescent protein to be on, P_f, the photobleaching lifetime, τ_{bleach}, and the blinking lifetime, τ_{blink} for which a molecule was either in the "on" or "off" state. At time equal to zero, a random number was generated from a uniform distribution and if this random number was less than P_f then the fluorophore was set to be in a bright state; otherwise the fluorophore remained in the dark state for the entire trace. To simulate a bleaching event, a random number was generated from an exponential distribution, with lifetime τ_{bleach}, and was defined to be the time at which bleaching occurred. At each time increment in the simulation a comparison was made between the value of the simulation time and the value of the randomly-generated bleaching time and if the simulation time was greater than the bleaching time then the fluorophore photobleached. Similarly, to simulate blinking, a random number was generated from an exponential distribution, with lifetime τ_{blink}, and was defined as the duration for which the fluorophore was in either a bright or a dark state. To determine which state the fluorophore was in, another random number was generated from a uniform distribution and if this random number was greater than 0.5 then the fluorophore was in a bright state; otherwise it was in a dark state. When the simulation time progressed to the end of this blinking event another randomly-generated blinking event was obtained and these blinking events repeated until the simulation time reached the maximum time specified for the trace. The simulated signal from each fluorophore was multiplied by a constant value and random noise (from a Poisson distribution with a specified expectation value) was added to adjust the signal-to-noise ratio of the trace. Simulated traces were generated by one researcher and counted in a double-blind way by another researcher.

References

Annibale, P., Scarselli, M., Greco, M. and Radenovic, A. (2012) 'Identification of the factors affecting co-localization precision for quantitative multicolor localization microscopy', *Optical Nanoscopy,* 1(1), pp. 9.

Annibale, P., Scarselli, M., Kodiyan, A. and Radenovic, A. (2010) 'Photoactivatable Fluorescent Protein mEos2 Displays Repeated Photoactivation after a Long-Lived Dark State in the Red Photoconverted Form', *The Journal of Physical Chemistry Letters,* 1(9), pp. 1506-1510.

Annibale, P., Vanni, S., Scarselli, M., Rothlisberger, U. and Radenovic, A. (2011a) 'Identification of clustering artifacts in photoactivated localization microscopy', *Nat Methods,* 8(7), pp. 527-8.

Annibale, P., Vanni, S., Scarselli, M., Rothlisberger, U. and Radenovic, A. (2011b) 'Quantitative photo activated localization microscopy: unraveling the effects of photoblinking', *PLoS One,* 6(7), pp. e22678.

Durisic, N., Cuervo, L. L. and Lakadamyali, M. (2014a) 'Quantitative super-resolution microscopy: pitfalls and strategies for image analysis', *Curr Opin Chem Biol,* 20C, pp. 22-28.

Durisic, N., Godin, A. G., Wever, C. M., Heyes, C. D., Lakadamyali, M. and Dent, J. A. (2012) 'Stoichiometry of the human glycine receptor revealed by direct subunit counting', *J Neurosci,* 32(37), pp. 12915-20.

Durisic, N., Laparra-Cuervo, L., Sandoval-Álvarez, A., Borbely, J. S. and Lakadamyali, M. (2014b) 'Single-molecule evaluation of fluorescent protein photoactivation efficiency using an in vivo nanotemplate', *Nat Methods*.

Gaitán-Peñas, H., Gradogna, A., Laparra-Cuervo, L., Solsona, C., Fernández-Dueñas, V., Barrallo-Gimeno, A., Ciruela, F., Lakadamyali, M., Pusch, M. and Estévez, R. (2016) 'Investigation of LRRC8-Mediated Volume-Regulated Anion Currents in Xenopus Oocytes', *Biophys J,* 111(7), pp. 1429-1443.

Goldin, A. L. (1992) 'Maintenance of Xenopus laevis and oocyte injection', *Methods Enzymol,* 207, pp. 266-79.

Gunzenhäuser, J., Olivier, N., Pengo, T. and Manley, S. (2012) 'Quantitative super-resolution imaging reveals protein stoichiometry and nanoscale morphology of assembling HIV-Gag virions', *Nano Lett,* 12(9), pp. 4705-10.

Heyes, C. D., Kobitski, A. Y., Breus, V. V. and Nienhaus, G. U. (2007) 'Effect of the shell on the blinking statistics of core-shell quantum dots: A single-particle fluorescence study', *Physical Review B,* 75(12), pp. 125431.

Hoi, H., Shaner, N. C., Davidson, M. W., Cairo, C. W., Wang, J. and Campbell, R. E. (2010) 'A monomeric photoconvertible fluorescent protein for imaging of dynamic protein localization', *J Mol Biol,* 401(5), pp. 776-91.

Lando, D., Endesfelder, U., Berger, H., Subramanian, L., Dunne, P. D., McColl, J., Klenerman, D., Carr, A. M., Sauer, M., Allshire, R. C., Heilemann, M. and Laue, E. D. (2012) 'Quantitative single-molecule microscopy reveals that

CENP-A(Cnp1) deposition occurs during G2 in fission yeast', *Open Biol,* 2(7), pp. 120078.

Lee, S. H., Shin, J. Y., Lee, A. and Bustamante, C. (2012) 'Counting single photoactivatable fluorescent molecules by photoactivated localization microscopy (PALM)', *Proc Natl Acad Sci U S A,* 109(43), pp. 17436-41.

Lynch, J. W. (2009) 'Native glycine receptor subtypes and their physiological roles', *Neuropharmacology,* 56(1), pp. 303-9.

McEvoy, A. L., Hoi, H., Bates, M., Platonova, E., Cranfill, P. J., Baird, M. A., Davidson, M. W., Ewers, H., Liphardt, J. and Campbell, R. E. (2012) 'mMaple: a photoconvertible fluorescent protein for use in multiple imaging modalities', *PLoS One,* 7(12), pp. e51314.

McKinney, S. A., Murphy, C. S., Hazelwood, K. L., Davidson, M. W. and Looger, L. L. (2009) 'A bright and photostable photoconvertible fluorescent protein', *Nat Methods,* 6(2), pp. 131-3.

Nan, X., Collisson, E. A., Lewis, S., Huang, J., Tamguney, T. M., Liphardt, J. T., McCormick, F., Gray, J. W. and Chu, S. (2013) 'Single-molecule superresolution imaging allows quantitative analysis of RAF multimer formation and signaling', *Proc Natl Acad Sci U S A,* 110(46), pp. 18519-24.

Opazo, F., Levy, M., Byrom, M., Schäfer, C., Geisler, C., Groemer, T. W., Ellington, A. D. and Rizzoli, S. O. (2012) 'Aptamers as potential tools for super-resolution microscopy', *Nat Methods,* 9(10), pp. 938-9.

Patterson, G. H. and Lippincott-Schwartz, J. (2002) 'A photoactivatable GFP for selective photolabeling of proteins and cells', *Science,* 297(5588), pp. 1873-7.

Planells-Cases, R., Lutter, D., Guyader, C., Gerhards, N. M., Ullrich, F., Elger, D. A., Kucukosmanoglu, A., Xu, G., Voss, F. K., Reincke, S. M., Stauber, T., Blomen, V. A., Vis, D. J., Wessels, L. F., Brummelkamp, T. R., Borst, P., Rottenberg, S. and Jentsch, T. J. (2015) 'Subunit composition of VRAC channels determines substrate specificity and cellular resistance to Pt-based anti-cancer drugs', *EMBO J,* 34(24), pp. 2993-3008.

Puchner, E. M., Walter, J. M., Kasper, R., Huang, B. and Lim, W. A. (2013) 'Counting molecules in single organelles with superresolution microscopy allows tracking of the endosome maturation trajectory', *Proc Natl Acad Sci U S A,* 110(40), pp. 16015-20.

Qiu, Z., Dubin, A. E., Mathur, J., Tu, B., Reddy, K., Miraglia, L. J., Reinhardt, J., Orth, A. P. and Patapoutian, A. (2014) 'SWELL1, a plasma membrane protein, is an essential component of volume-regulated anion channel', *Cell,* 157(2), pp. 447-458.

Ran, F. A., Hsu, P. D., Wright, J., Agarwala, V., Scott, D. A. and Zhang, F. (2013) 'Genome engineering using the CRISPR-Cas9 system', *Nat Protoc,* 8(11), pp. 2281-2308.

Renz, M., Daniels, B. R., Vámosi, G., Arias, I. M. and Lippincott-Schwartz, J. (2012) 'Plasticity of the asialoglycoprotein receptor deciphered by ensemble FRET

imaging and single-molecule counting PALM imaging', *Proc Natl Acad Sci U S A,* 109(44), pp. E2989-97.

Ries, J., Kaplan, C., Platonova, E., Eghlidi, H. and Ewers, H. (2012) 'A simple, versatile method for GFP-based super-resolution microscopy via nanobodies', *Nat Methods,* 9(6), pp. 582-4.

Sengupta, P., Jovanovic-Talisman, T. and Lippincott-Schwartz, J. (2013) 'Quantifying spatial organization in point-localization superresolution images using pair correlation analysis', *Nat Protoc,* 8(2), pp. 345-54.

Sengupta, P., Jovanovic-Talisman, T., Skoko, D., Renz, M., Veatch, S. L. and Lippincott-Schwartz, J. (2011) 'Probing protein heterogeneity in the plasma membrane using PALM and pair correlation analysis', *Nat Methods,* 8(11), pp. 969-75.

Simonson, P. D., Deberg, H. A., Ge, P., Alexander, J. K., Jeyifous, O., Green, W. N. and Selvin, P. R. (2010) 'Counting bungarotoxin binding sites of nicotinic acetylcholine receptors in mammalian cells with high signal/noise ratios', *Biophys J,* 99(10), pp. L81-3.

Subach, F. V., Patterson, G. H., Manley, S., Gillette, J. M., Lippincott-Schwartz, J. and Verkhusha, V. V. (2009) 'Photoactivatable mCherry for high-resolution two-color fluorescence microscopy', *Nat Methods,* 6(2), pp. 153-9.

Syeda, R., Qiu, Z., Dubin, A. E., Murthy, S. E., Florendo, M. N., Mason, D. E., Mathur, J., Cahalan, S. M., Peters, E. C., Montal, M. and Patapoutian, A. (2016) 'LRRC8 Proteins Form Volume-Regulated Anion Channels that Sense Ionic Strength', *Cell,* 164(3), pp. 499-511.

Ulbrich, M. H. and Isacoff, E. Y. (2007) 'Subunit counting in membrane-bound proteins', *Nat Methods,* 4(4), pp. 319-21.

Ullrich, F., Reincke, S. M., Voss, F. K., Stauber, T. and Jentsch, T. J. (2016) 'Inactivation and Anion Selectivity of Volume-regulated Anion Channels (VRACs) Depend on C-terminal Residues of the First Extracellular Loop', *J Biol Chem,* 291(33), pp. 17040-8.

Veatch, S. L., Machta, B. B., Shelby, S. A., Chiang, E. N., Holowka, D. A. and Baird, B. A. (2012) 'Correlation functions quantify super-resolution images and estimate apparent clustering due to over-counting', *PLoS One,* 7(2), pp. e31457.

Voss, F. K., Ullrich, F., Münch, J., Lazarow, K., Lutter, D., Mah, N., Andrade-Navarro, M. A., von Kries, J. P., Stauber, T. and Jentsch, T. J. (2014) 'Identification of LRRC8 heteromers as an essential component of the volume-regulated anion channel VRAC', *Science,* 344(6184), pp. 634-8.

Wang, M. H. (2004) 'A technical consideration concerning the removal of oocyte vitelline membranes for patch clamp recording', *Biochem Biophys Res Commun,* 324(3), pp. 971-2.

Wiedenmann, J., Ivanchenko, S., Oswald, F., Schmitt, F., Röcker, C., Salih, A., Spindler, K. D. and Nienhaus, G. U. (2004) 'EosFP, a fluorescent marker

protein with UV-inducible green-to-red fluorescence conversion', *Proc Natl Acad Sci U S A,* 101(45), pp. 15905-10.

Wood, A. J., Lo, T. W., Zeitler, B., Pickle, C. S., Ralston, E. J., Lee, A. H., Amora, R., Miller, J. C., Leung, E., Meng, X., Zhang, L., Rebar, E. J., Gregory, P. D., Urnov, F. D. and Meyer, B. J. (2011) 'Targeted genome editing across species using ZFNs and TALENs', *Science,* 333(6040), pp. 307.

Zanacchi, F. C., Manzo, C., Alvarez, A. S., Derr, N. D., Garcia-Parajo, M. F. and Lakadamyali, M. (2017) 'A DNA origami platform for quantifying protein copy number in super-resolution', *Nat Methods,* 14(8), pp. 789-792.

Zhang, M., Chang, H., Zhang, Y., Yu, J., Wu, L., Ji, W., Chen, J., Liu, B., Lu, J., Liu, Y., Zhang, J., Xu, P. and Xu, T. (2012) 'Rational design of true monomeric and bright photoactivatable fluorescent proteins', *Nat Methods,* 9(7), pp. 727-9.

Chapter 4

LGI1 Synaptic Protein Complex

In the previous chapters we have explained the importance of knowing the molecular organization of certain complexes in the synapse and how super-resolution techniques not only help us to achieve nanoscale resolution but also enable quantitative analysis of protein organization and stoichiometry in cells. In this last part of the thesis we apply these super-resolution techniques to unveil the molecular organization of the LGI1 synaptic protein complex. This complex has an important role in neuronal function and has been linked to severe neurological disorders. We show the molecular structure of the protein complex at the nanoscale level as well as estimate the stoichiometry among the different members of this complex in healthy neurons as well as in neurons treated with patient autoantibodies against LGI1.

4.1 Introduction

Memory, behavior, and cognition are dependent on the normal function of neurotransmitter receptors, ion channels and other regulatory proteins involved in synaptic transmission and plasticity (Lau and Zukin, 2007, Shepherd and Huganir, 2007). Synaptic transmission requires a fine-tuned balance between excitation and inhibition in neural circuits. Disruption of this balance can lead to dramatic neurological disorders, such as epilepsy, that can cause memory loss and seizures.

Initial studies on the LGI1 gene showed a relation of this gene with epilepsy. Experiments with mutations in the LGI1 gene demonstrated a linkage with autosomal dominant lateral temporal lobe epilepsy (ADLTE). Recent studies have identified a group of human autoimmune disorders in which several synaptic receptors and proteins are targeted by autoantibodies (Lancaster and Dalmau, 2012, Graus et al., 2016). In one of these autoimmune diseases, autoantibodies against LGI1 are produced. Here, we will study how autoantibodies may impact the nanoscale localization of proteins within the LGI1 complex.

4.1.1 LGI1 complex

The central protein of the complex is LGI1 (leucine-rich glioma inactivated 1) protein, a secreted protein whose molecular mass is approximately 60 kDa (Chernova et al., 1998). It essentially consists of a domain of four LRRs (leucine-rich repeats) (Kobe and Kajava, 2001) and a so-called epilepsy-associated or EPTP (epitempin) domain containing seven EPTP repeats (Scheel et al., 2002, Staub et al., 2002). Both domains are thought to function in protein–protein interactions although only a subset of LGI binding partners has been identified. LGI1 is secreted (Senechal et al., 2005) and has a high possibility to dimerize with other LGI1 proteins through the LRR domain (Fukata et al., 2006). Co-immunoprecipitation experiments showed that secreted LGI1 interacts with the intracellular PSD-95 protein through a transmembrane protein that acts as a receptor for LGI1, ADAM22. Mutations in the EPTP domain of

LGI1 showed no co-immunoprecipitation with ADAM22, indicating that EPTP is the binding site of LGI1 to this protein (Fukata et al., 2006). Similar experiments showed interaction of LGI1 with another member of the ADAM family, ADAM23 (Fukata et al., 2010) (Owuor et al., 2009). Moreover, both ADAM22 and ADAM23 knockout mice show strong overlap in phenotype with LGI1 knockout mice, which is characterized by severe spontaneous epilepsy and premature death (Sagane et al., 2005, Owuor et al., 2009, Chabrol et al., 2010, Fukata et al., 2010, Yu et al., 2010). Importantly, ADAM22 and ADAM23 co-assemble in the brain in a manner dependent on LGI1 (Fukata et al., 2010). Thus, it was hypothesized that LGI1 forms a bridge between presynaptic ADAM23 and postsynaptic ADAM22 (Fukata et al., 2010), effectively regulating trans-synaptic interactions contributing to synaptic stability (**Figure 4.1**).

The extracellular domain of ADAM22 allows the binding of LGI1, whereas the cytoplasmic domain is anchored to the postsynaptic density by the cytoskeletal scaffold protein PSD95. This postsynaptic density also contains stargazin, a transmembrane regulatory subunit that is crucial for the trafficking and gating of the AMPA receptor (AMPAR) (Chen et al., 2000, Tomita et al., 2005, Nicoll et al., 2006) (**Figure 4.1**).

Additionally, LGI1 is functionally and physiologically related to the Kv1.1 subunit of voltage-gated potassium channels (VGKC). Current measurements in *Xenopus* oocytes coexpressing LGI1 protein showed a reduction of Kv1.1 inactivation in action potentials (Schulte et al., 2006). Mutations in LGI1 prevented this effect, resulting in rapid inactivation of the Kv1.1 channels and thus causing a broadening of the action potential. Such findings together with electrophysiological experiments on LGI1 function in presynaptic Kv1.1-associated protein complexes suggest that LGI1

prevents the increase of neurotransmitter release by slowing down the inactivation of Kv1 channels (Schulte et al., 2006).

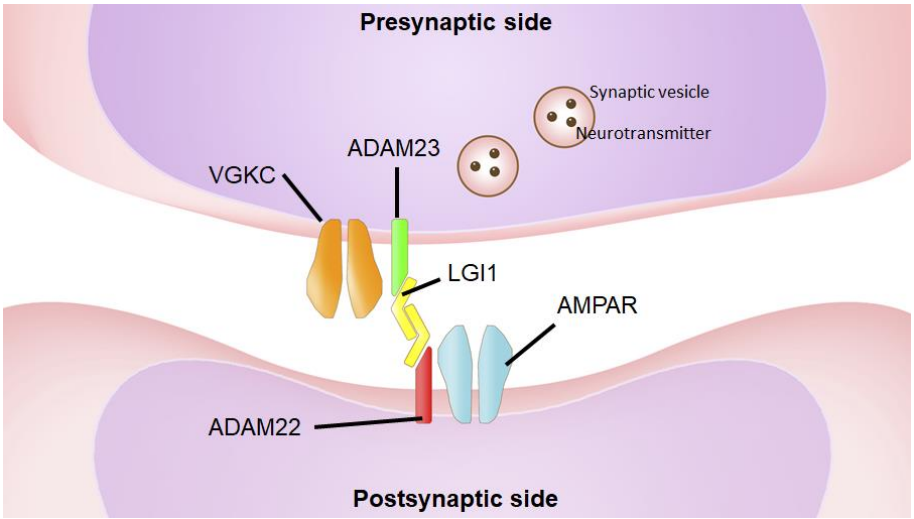

Figure 4.1 Schematic drawing of LGI1 molecular complex. *LGI1 is a secreted protein that interacts with two transmembrane proteins, presynaptic ADAM23 and postsynaptic ADAM22 organizing a trans-synaptic protein complex that includes presynaptic VGKC and postsynaptic AMPA receptors.*

4.1.2 LGI1 in autosomal dominant lateral temporal lobe epilepsy (ADLTE)

Previous observations underscore an important role for LGI1 in brain excitation and development. Knockout of the LGI1 gene in mice leads to a lethal epileptic phenotype, predominantly characterized by seizures (Yu et al., 2010). Similar epileptic phenotypes are observed with knockouts of ADAM22, ADAM23, and VGKC channels, also characterized by severe spontaneous epilepsy and premature death. Moreover, mutations of LGI1 gene also cause autosomal dominant partial epilepsy with auditory seizures (ADPEAF) or ADLTE (Kalachikov et al., 2002, Morante-Redolat et al., 2002). Most ADLTE mutations alter the ability of the LRR domain or the EPTP domain to fold properly, thereby inhibiting LGI1 secretion (de Bellescize et al., 2009, Di Bonaventura et al., 2011, Striano et al., 2011, Nobile et al., 2009). These

mutations have provided some important information about the functional interactions of LGI1 protein.

4.1.3 LGI1 in Autoimmune limbic encephalitis

There are currently 16 identified autoimmune encephalitis in which autoantibodies are directed against neuronal proteins involved in synaptic transmission, somatodendritic signal integration, clustering and modulation of receptors, synaptic vesicle reuptake, or synaptogenesis (Dalmau et al., 2007, Lai et al., 2009, Lai et al., 2010, Lancaster et al., 2010, Hutchinson et al., 2008). Out of these identified targets, LGI1 is among the most common ones, together with NMDA receptors (Lancaster et al., 2011). LGI1 limbic encephalitis causes severe loss of memory, seizures and epilepsy, leading in some cases to death. It preferentially affects patients between 30 and 80 years old with a slight predominance for men (median age: 60 years) (Lai et al., 2010). The memory loss among other symptoms of dysfunction in the limbic system can be preceded by seizures. Most patients with LGI1 autoantibodies show epileptic activity in frontal cortical and hippocampal regions according to electrophysiological measurements (Navarro et al., 2016). From the 70% of patients that recover neurological function after immunotherapy, only 35% return to the basal cognitive function. Relapses may happen in 24-35% of the cases (Ariño et al., 2016, van Sonderen et al., 2016).

In most autoimmune encephalitis disorders, autoantibodies cross-link receptors, leading to their internalization and degradation. One of the special characteristics of LGI1 autoimmune limbic encephalitis is the fact that the antibody subclass is IgG4, instead of IgG1 (Ariño et al., 2016). This subclass has a hetero-bispecific nature, which makes it is less effective in cross-linking and internalizing the target antigen than those with IgG1. Consequently, the disruption of the normal function of the target is due to the fact that the autoantibodies interfere with protein-protein interactions, disrupting the LGI1 complex (Dalmau et al., 2017). More specifically, it

has been suggested that antibodies against LGI1 prevent the binding of this protein to ADAM22 and ADAM23 (Ohkawa et al., 2013). Immunoprecipitation and mass spectrometry experiments showed different target antigens for the LGI1 autoantibodies, suggesting that they have a polyclonal configuration and thus can bind to several LGI1 domains (Ohkawa et al., 2013). Moreover, preincubation of patient antibodies in primary neurons caused downregulation of AMPARs, leading to an epileptic phenotype, however, the causes remain unclear. To date, there is no direct functional evidence of how LGI1 antibodies affect neuronal excitability and synaptic transmission.

In addition to the previous experiments evaluating the pathogenic effect of LGI1 antibodies on synaptic function and levels of synaptic proteins, further studies are needed to understand the mechanisms underlying LGI1-antibody mediated hyperexcitability in neuronal networks. Immunoprecipitation methods were used to identify the proteins involved in the LGI1 complex. Nevertheless, a subcellular analysis of the molecular organization of the complex in the spatial context of the synapse under physiological conditions and after treatment with autoantibodies against LGI1 is missing. In this thesis, we aimed to determine the synaptic organization of proteins that are known to interact with LGI1, including ADAM22, ADAM23, Kv1.1 and GluR1, an AMPAR subunit, and analyze the effect of autoantibodies on this organization. Our starting point was to unveil the molecular structure of the LGI1 complex using super-resolution fluorescence techniques. Additionally, we characterized the same structure in neurons treated with antibodies from patients with LGI1 autoimmune encephalitis.

4.2 LGI1 complex in physiological conditions

The imaging of the synapses in super-resolution was performed in cultured hippocampal neurons. This type of neurons are one of the most common models in excitatory synapses. Moreover, most of the experiments used to reveal the interaction between the different proteins of the complex used these neurons as well as hippocampal tissue as their models (Fukata et al., 2006, Owuor et al., 2009, Fukata et al., 2010, Okhawa et al., 2013). Additionally, the tests to detect the effects of the LGI1 autoantibody performed by our collaborator's lab (Josep Dalmau's lab) confirmed a high reactivity in the hippocampus of rats and mice. Therefore, we considered the hippocampal neurons to be the optimal model for our experiments.

We used an imaging method previously developed by Dani et al. (Dani et al., 2010). To this end, we used multi-color STORM using activator-reporter pairs (3 different activator fluorophores and 1 reporter fluorophore: AF405-AF647, Cy3-AF647 and Cy2-AF647) (see Methods and Chapter 2.6.1) to image two well-defined pre- and post-synaptic proteins, Bassoon and Homer1 (from now on referred to as Homer), respectively. Bassoon and Homer super-resolution images revealed the close apposition of these two proteins at the synapse. In addition to Bassoon and Homer, we additionally imaged a third protein belonging to one of the members of the LGI1 complex. These 3AF405-color images were used to determine the position of the LGI1 complex proteins relative to Bassoon and Homer. However, using the method of Dani *et al.*, we faced several problems. The most important ones were the cross-talk and the low density in the labeling. Except for GluR1, all the other antibodies against the proteins of the LGI1 complex, namely ADAM22, ADAM23, Kv1.1 and LGI1, have a very low signal, probably because of their low density in the synapse. This low density of labeling combined with the higher density labeling of Homer and Bassoon led to color cross-talk from Homer and Bassoon into the protein of interest, making it challenging to identify the position of the protein. To reduce cross-talk between the different colors, we developed a modified sequential imaging

approach. Firstly, Homer and Bassoon were imaged and then the 3rd protein was imaged in a separate sequence (**Figure 4.2**). This modified approach led to less cross-talk, since the Homer and Bassoon signals were mostly photobleached during the first round of imaging and did not contribute to signal in the second round of imaging.

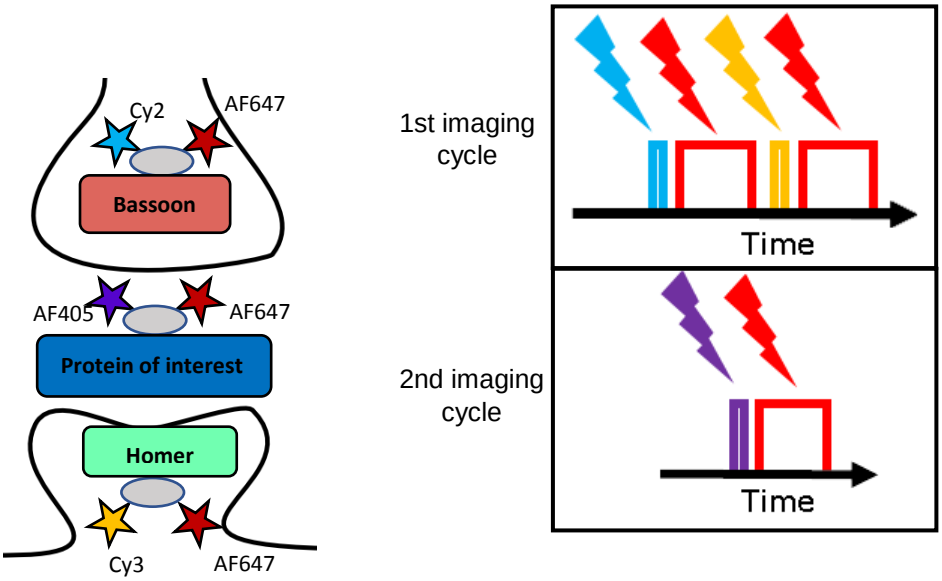

Figure 4.2. Labeling and imaging strategy. *3-color STORM was used for imaging the LGI1 complex. 3 dye-pairs with different activators, Cy3, Cy2 and AF405, and the same reporter, AF647 were immuno-stained to 3 different proteins, Homer (green), Bassoon (red) and the protein of interest (blue) (left). By controlling the excitation of the different laser lights for the activators, one could separate in time the images coming from the reporters, obtaining 3 STORM images, each of them corresponding to one protein. In order to avoid cross-talk, the imaging was divided in 2 sequences. In the first sequence, cycles of 560/647 nm laser lights and 488/647 nm laser lights were used with a time exposure of 20ms/frame. After that, the imaging with 405/647 nm laser light was performed at the same frame rate (right).*

The STORM images were analyzed and rendered using custom-written software. **Figure 4.3** shows an example of the resulting reconstructed image of Homer (green), Bassoon (red) and LGI1 (blue).

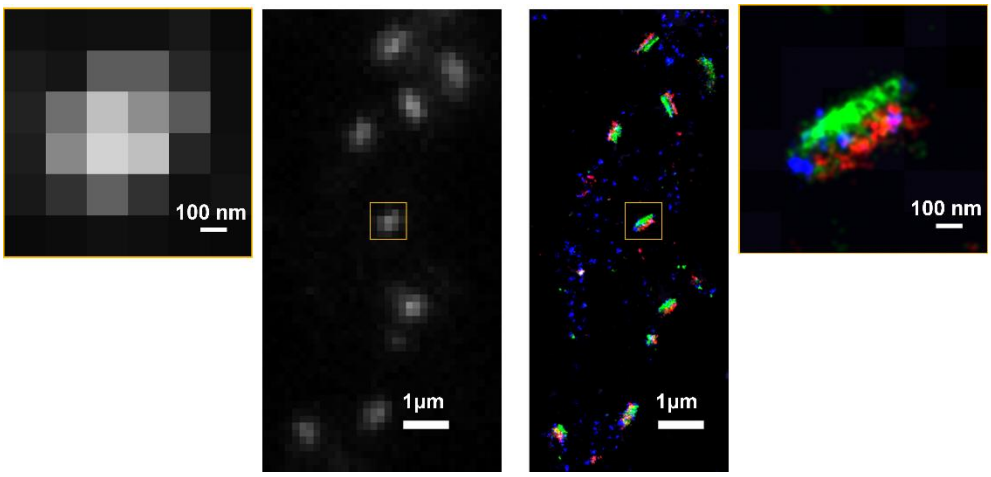

Figure 4.3. 3-color STORM image. *Initially, a snapshot of the conventional image was saved (center left). After reconstructing the STORM image, a super-resolved image with 3 channels was obtained (center right). Synapses were easily identified by looking at Homer clusters (**green**) opposing to Bassoon clusters (**red**). The 3rd protein (**blue**) presented sets of smaller clusters around the two synaptic reference proteins. The comparison of the insets of the conventional image (extreme left) and the STORM image (extreme right) show a clear improvement of the resolution.*

Since the imaging was done in 2D, synapses that are perpendicular to the imaging plane will have completely overlapping Homer and Bassoon images. To simplify quantitative analysis, we manually selected synapses in which Homer and Bassoon were well separated and the synapse appeared to be aligned parallel to the imaging plane (**Figure 4.4**).

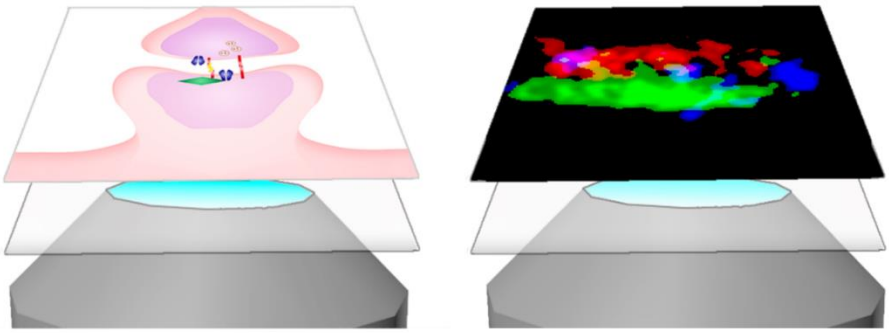

Figure 4.4. Parallel synapses to the image plane. *The chosen synapses for analysis showed very few or no overlapping of Homer and Bassoon clusters, corresponding to the synapses whose orientation was parallel to the image plane.*

The images were further analyzed using a previously developed cluster analysis method (Ricci et al., 2015). This analysis allowed us to automatically segment the super-resolution localizations belonging to each protein (Homer, Bassoon or one of the members of the LGI1 complex). We then automatically grouped together the segmented localizations belonging to the same synapse as individual objects for further analysis (See Methods). A synapse was defined as those regions of the image that contained both Homer and Bassoon within 250 nm of each other's center of mass and 300 nm between Homer and the protein of interest (**Figure 4.5**).

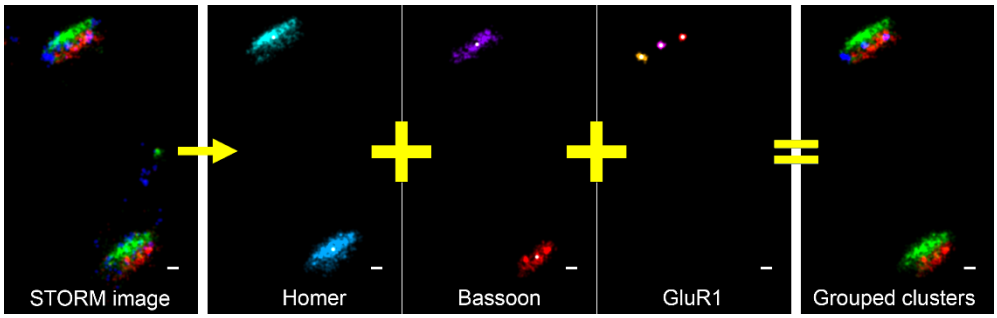

Figure 4.5 Cluster analysis workflow. *After the localizations reconstruction (left), the Matlab program was run separately for each channel to group localizations to individual clusters for Homer, Bassoon and the protein of interest, GluR1 in this example (middle). After that, another Matlab program selected the clusters that were belonging to the same synapse and grouped them into one unit of analysis. The clusters that were not considered to belong to synapses were excluded, therefore, some synapses did not contain any cluster of the 3rd protein. Scale bar: 100 nm.*

Several parameters were extracted from each synapse including the number of protein clusters, the number of localizations per protein cluster, the relative distance of protein cluster to Homer and Bassoon and the nearest neighbor distances between Homer and Bassoon (see below).

4.2.1 Individual synapse analysis

To determine the synaptic localization of the proteins within the LGI1 complex, we imaged LGI1, ADAM22, ADAM23, Kv1.1 and GluR1. The most abundant protein in

synapses was GluR1, with 69 % of the synapses containing at least one cluster of localizations belonging to this protein (**Figure 4.6**). ADAM23 and LGI1 were also abundant with 58 % and 59 % of synapses containing ADAM23 and LGI1, respectively (**Figure 4.6**). Kv1.1 and ADAM22 were less abundant than these other proteins, only 34 % and 38 % of synapses contained Kv1.1 and ADAM22, respectively (**Figure 4.6**). These results suggest that only a small percentage of synapses likely contain all 5 proteins and ADAM22 and Kv1.1 are the limiting proteins of the entire complex.

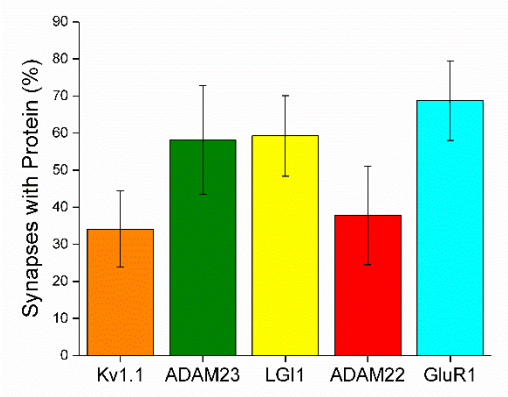

Figure 4.6: Percentage of synapses containing proteins of the LGI1 complex. *Kv1.1: 34.1+/-10.3% (n = 261), ADAM23: 58.1+/-14.6% (n = 198), LGI1: 59.2+/-10.87% (n = 287), ADAM22: 37.8+/-13.3% (n = 127), GluR1: 68.8+/-10.7% (n = 96). The whiskers correspond to the standard deviation.*

We next determined the nanoscale organization of each protein within the synapse. We noticed that most proteins were arranged as nano-sized clusters in the synapse and in some cases more than one nano-cluster was present in each synapse. Our cluster segmentation algorithm allowed us to group together localizations that were in close proximity and formed a nano-cluster. We could therefore determine the number of nano-clusters per synapse for the 5 different proteins that we imaged (**Figure 4.7**).

Most proteins formed on average one or two nano-clusters with the exception of GluR1, which organized into on average 2.7 nano-clusters per synapse. These results

are consistent with previous studies that revealed that AMPA receptors are organized in nanodomains in the synapse (Nair et al., 2013).

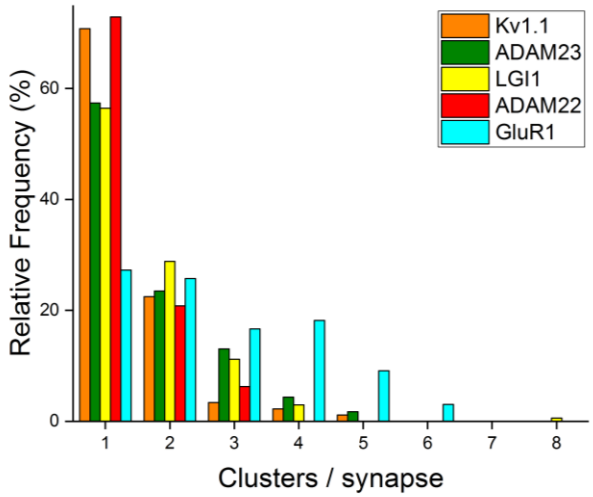

Figure 4.7: Relative frequency of clusters per synapse. *Kv1.1: 70.8% with 1 cluster, 22.5% with 2 clusters, 3.4% with 3 clusters, 2.2% with 4 clusters 1.1% with 5 clusters out of 89 synapses. ADAM23: 57.4% with 1 cluster, 23.5% with 2 clusters, 13.0 with 3 clusters, 4.3% with 4 clusters and 1.7% with 5 clusters, out of 115 synapses. LGI1: 56.5% with 1 cluster, 28.8% with 2 clusters, 11.2% with 3 clusters, 2.9 with 4 clusters and 0.6% with 8 clusters out of 170 synapses. ADAM22: 72.9% with 1 cluster, 20.8% with 2 clusters and 6.3% with 3 clusters out of 48 synapses. GluR1: 27.3% with 1 cluster, 25.8% with 2 clusters, 16.7% with 3 clusters, 18.2% with 4 clusters, 9.1% with 5 clusters and 3.0% with 6 clusters out of 66 synapses.*

We next characterized the number of localizations in each of these clusters (**Figure 4.8**). The number of localizations is proportional to the number of proteins in the cluster.

The number of localizations was similar among the three central proteins of the complex: ADAM23, LGI1 and ADAM22 suggesting that they are likely present in a one-to-one stoichiometry (Median+/- SD: $Median_{ADAM23}$ = 46.5 +/- 73.9, $Median_{LGI1}$ = 55 +/- 84.6 and $Median_{ADAM22}$ = 63 +/- 50.4). Kv1.1 clusters had a lower number of localizations ($Median_{Kv1.1}$ = 34 +/- 26.7), potentially due to a low presence of these subunits in synapses, although we cannot exclude low labeling efficiency with the Kv1.1 antibody. On the contrary, GluR1 clusters were composed of much higher

number of localizations ($Median_{GluR1}$ = 205 +/- 129.7) suggesting the high abundance of these receptors.

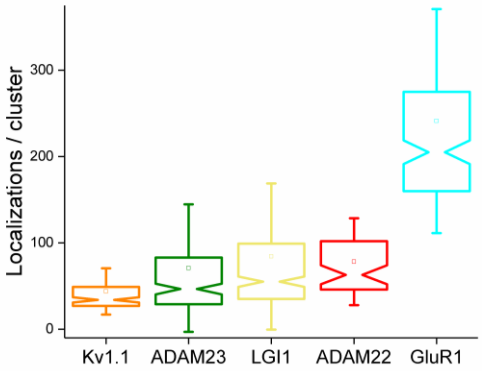

Figure 4.8. Number of localizations per cluster. *The notched distribution shows the IQR (box), the notch (95% confidence interval of the median), the median (center of the notch) and the mean (dot). The whiskers represent the standard deviation. Median/IQR: Kv1.1: 34/22 (n = 125). ADAM23: 46.5/54 (n = 192). LGI1: 55/64 (n = 279). ADAM22: 63/56 (n = 64). GluR1: 205/115 (n = 175).*

Finally, we analyzed the relative position of the different proteins with respect to Homer and Bassoon. To this end, we aligned the long axis of Homer and Bassoon images with the y-axis and projected the localizations onto the x-axis. We then plotted a histogram of the localizations along the x-axis and fitted them to Gaussian distributions. The peak of these fits was taken to be the position of the three proteins and the peak-to-peak distance was calculated to determine the distance from one protein to the others (**Figure 4.9**).

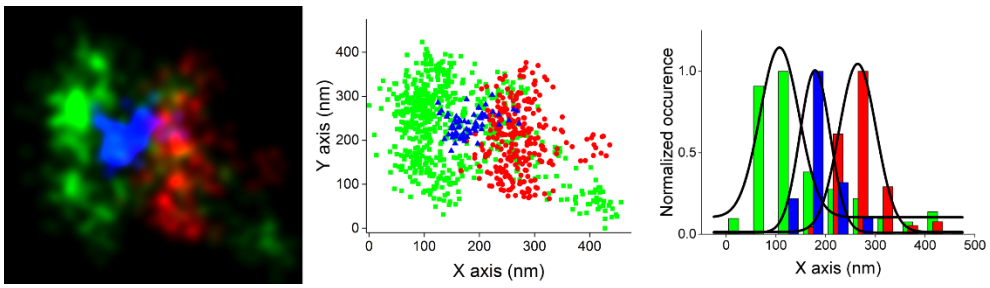

Figure 4.9. Analysis for the relative distance. *The super-resolved reconstructions of images of synapses containing Homer (green), Bassoon (red) and the protein of interest (blue) (left) were used to identify and rotate their localizations into one of the axis (middle). The projections of these localizations into the other axis were plotted in histograms (right). These histograms were fitted into Gaussian distributions to find the central peak for each of the 3 channels. The histograms have been normalized to simplify the visualization.*

We manually selected synapses that were roughly parallel to the imaging plane, nonetheless there is a variability in the Homer-to-Bassoon distances arising from some synapses that might be tilted with respect to the imaging plane and biological variability among different synapses (**Figure 4.10**).

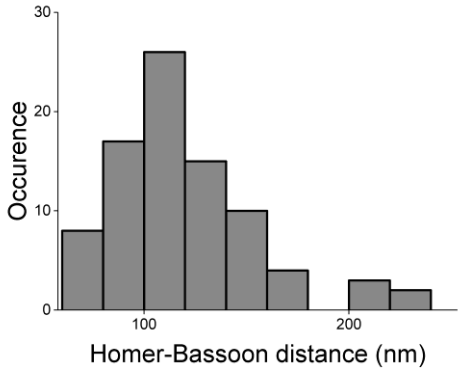

Figure 4.10 Homer-Bassoon distance distribution. *Homer-Bassoon distances distributions for treated data. Histogram of the distribution of distances between the centers of mass of the Homer and Bassoon clusters for synapses containing at least one cluster of LGI1 within them.*

To overcome this heterogeneity, for each synapse, we normalized the distance between the protein of interest (LGI1, ADAM22, ADAM23, Kv1.1 or GluR1) and Bassoon to the distance between Homer and Bassoon. This normalization allowed us to obtain a relative distance between the protein of interest and Homer or Bassoon. **Figure 4.11** shows the relative distances for the 5 different proteins imaged, in which Homer is at position 0 and Bassoon at position 1.

As expected, all the pre-synaptic proteins (ADAM23 and Kv1.1) were closer to Bassoon whereas all the postsynaptic proteins (ADAM22 and GluR1) were closer to Homer validating our approach. LGI1 position showed a broad distribution likely reflecting the polyclonal nature of the LGI1 autoantibody, which was used for the labeling. Alternatively, the broad distribution may be due to a mixed orientation of the LGI1 proteins within the synaptic cleft. Despite the broad distribution, on average the position of LGI1 was found to be between ADAM22 and ADAM23 positions, confirming its trans-synaptic localization.

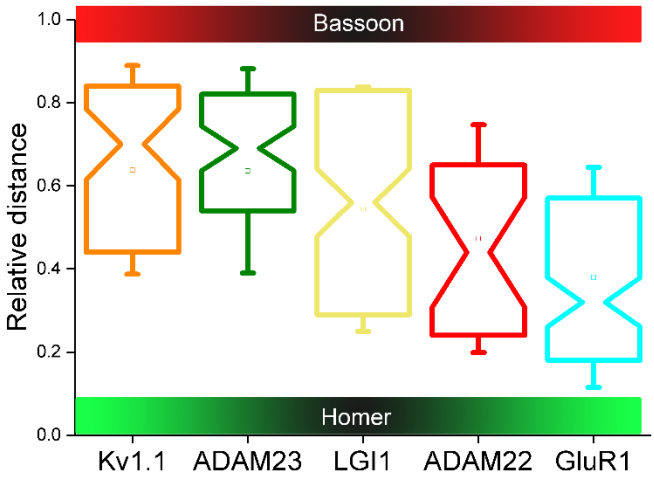

Figure 4.11. Relative distance distributions of the LGI1 complex proteins. *The notched distribution shows the IQR (box), the notch (95% confidence interval of the median), the median (center of the notch) and the mean (dot). The whiskers represent the standard deviation. The Medians/IQRs are: Kv1.1: 0.70/0.40 (n = 55), ADAM23: 0.69/0.28 (n = 69), LGI1: 0.56/0.54 (n = 111), ADAM22: 0.44/0.41 (n = 24), GluR1: 0.32/0.39 (n = 111).*

4.2.2 "Super-synapse" analysis

As we performed 2D images, it was possible that the orientation of the synapses was not totally parallel to the image plane. Even though we particularly took the ones oriented in the correct direction and excluded the ones that looked misaligned, a small portion of synapses might not have been completely well oriented. In order to correct for this error, we performed another analysis to validate our previous results. We analyzed a sub-population of synapses that fulfilled two criteria: containing at least one cluster of the protein of interest between Homer and Bassoon and having a distance between Homer and Bassoon in a range of 60-200 nm. The different localizations from each synapse were aligned taking the center of mass of the cluster corresponding to Homer to be the position at 0. We then merged all the localizations of all these synapses in one single "super-synapse" (**Figure 4.12**-left). This type of analysis, in which multiple images of a given complex are aligned and averaged is typical in cryo-EM and has previously been applied to super-

resolution images of nuclear pore complex subunits, where they developed a single particle averaging routine that allowed them to combine information from localizations of thousands of pores (Szymborska et al., 2013). We then extracted the relative position of the various proteins following the same approach described in the previous section and measuring the distance between the peaks of the Gaussian distributions (**Figure 4.12**- right).

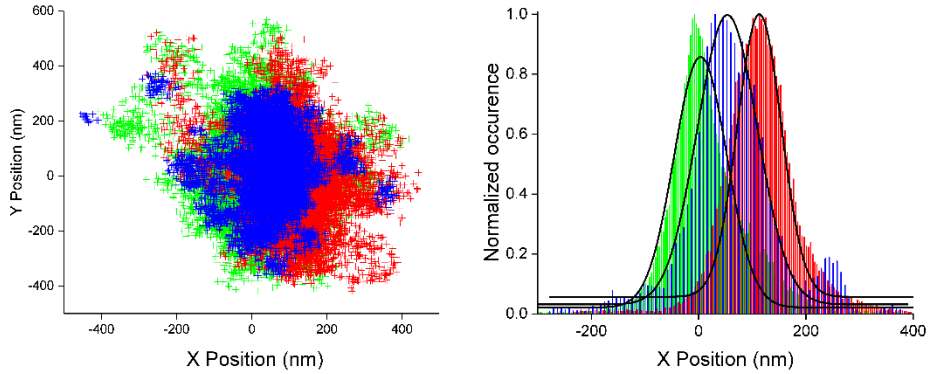

Figure 4.12. LGI1 super-synapse. *Reconstruction of the super-synapse of LGI1 with localizations from a merger of n = 83 synapses (left) and a normalized histogram of the projection of the localizations in the x axis (right) showing Homer (green), Bassoon (red) and LGI1 (blue) and their Gaussian fits (black lines).*

In this case, since the distributions contained many more points than in the case of individual synapses (above), the Gaussian fitting was less noisy and hence the position of the protein could be determined more precisely. Taking the peak-to-peak distance of the centers of the Homer and Bassoon Gaussian fittings, we then could establish a relative distance of the protein of interest with respect to Homer as we have done before. **Figure 4.13** shows a comparison of the relative distance distributions obtained using the single-synapse analysis (box plots) and the relative position extracted from the super-synapse analysis (black bars with SE).

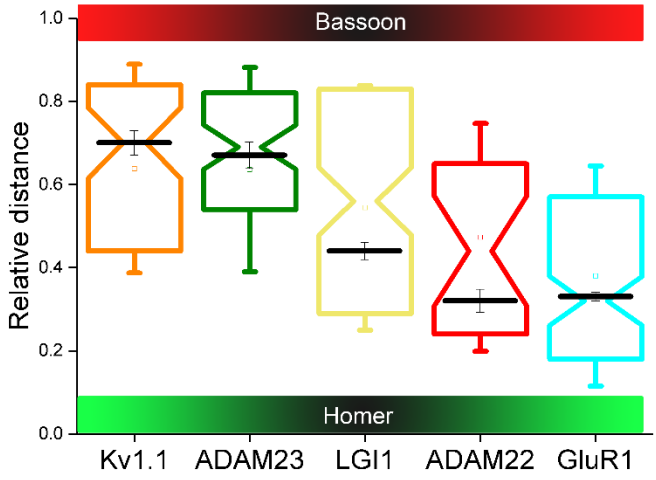

Figure 4.13: Comparison of the individual synapse analysis with the super-synapse analysis. *The values of the relative distance extracted from the super-synapses are represented by the black line with the black whiskers being the standard error. Kv1.1: 0.72+/-0.03 (n = 49), ADAM23: 0.69+/-0.03 (n = 59), LGI1: 0.46+/- =0.02 (n = 83), ADAM22: 0.34+/-0.03 (n = 25) and GluR1: 0.35+/-0.01 (n = 50).*

The results obtained with the super-synapse analysis were in high accordance with the results coming from the analysis of individual synapses. In both cases, and especially with the "super-synapse" analysis, LGI1 appeared closer to the post-synaptic protein ADAM22, potentially suggesting that LGI1 may associate more closely with the post- than the pre-synapse.

In conclusion, our results reveal the localization of the main proteins within the LGI1 complex in single synapses.

4.3 LGI1 complex in neurons treated with LGI1 autoantibodies

We next aimed to characterize the organization of LGI1 complex in neurons treated with cerebrospinal fluid (CSF) from patients that tested positive for LGI1 autoimmune encephalitis and hence containing LGI1 autoantibodies (CSF+), whose

reactivity was previously tested by our collaborators (see Methods). After 3 days of treatment with CSF+, we fixed the neurons, labeled and imaged the various proteins within the LGI1 complex as before. As a negative control, we also treated neurons with CSF from patients that tested negative for all the autoimmune encephalitis identified targets (CSF-). We analyzed the images as described above.

After treatment with CSF+, the percentage of synapses that contained the different proteins within the LGI1 complex did not change (**Figure 4.14**), suggesting that antibodies did not lead to internalization of the receptors or did not interfere with the secretion of LGI1.

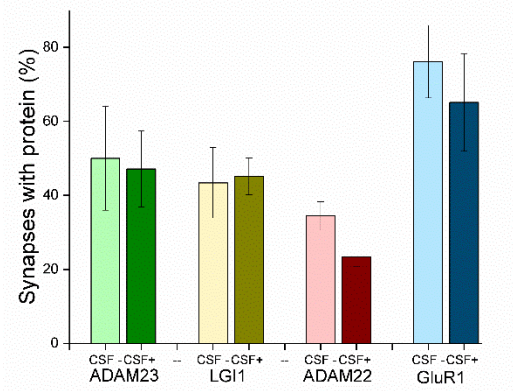

Figure 4.14. Percentage of synapses containing proteins of the LGI1 complex in control and treated conditions. *For CSF negative (**CSF -**): ADAM23: 50.0+/-14.0% (n = 200), LGI1: 43.4+/-9.5% (n = 355), ADAM22: 34.4+/-3.8% (n = 244), GluR1: 76.1+/-9.8% (n = 201). CSF Positive (**CSF +**): ADAM23: 47.1+/-10.2% (n = 244), LGI1: 45.2+/-4.9% (n = 423), ADAM22: 23.5+/-2.6% (n = 426), GluR1: 65.1+/-13.2% (n = 192). The whiskers correspond to the standard deviation.*

We also determined the number of clusters of the proteins of interest in each synapse and compared CSF positive and negative treatments (**Figure 4.15**).

There was a tendency for the synapses to have an increase in the number of ADAM 23 clusters. Even though the majority of synapses still had mostly one cluster (between 65-70 % of the synapses), synapses having 3, 4 or even 5 clusters were more frequent. For all other proteins, the number of clusters per synapse did not change significantly with antibody treatment. The number of localizations per cluster also did not change after CSF positive treatment (**Figure 4.16**). Overall, these

results suggest that the autoantibodies do not significantly impact the stoichiometry and copy number of various proteins in the synapse.

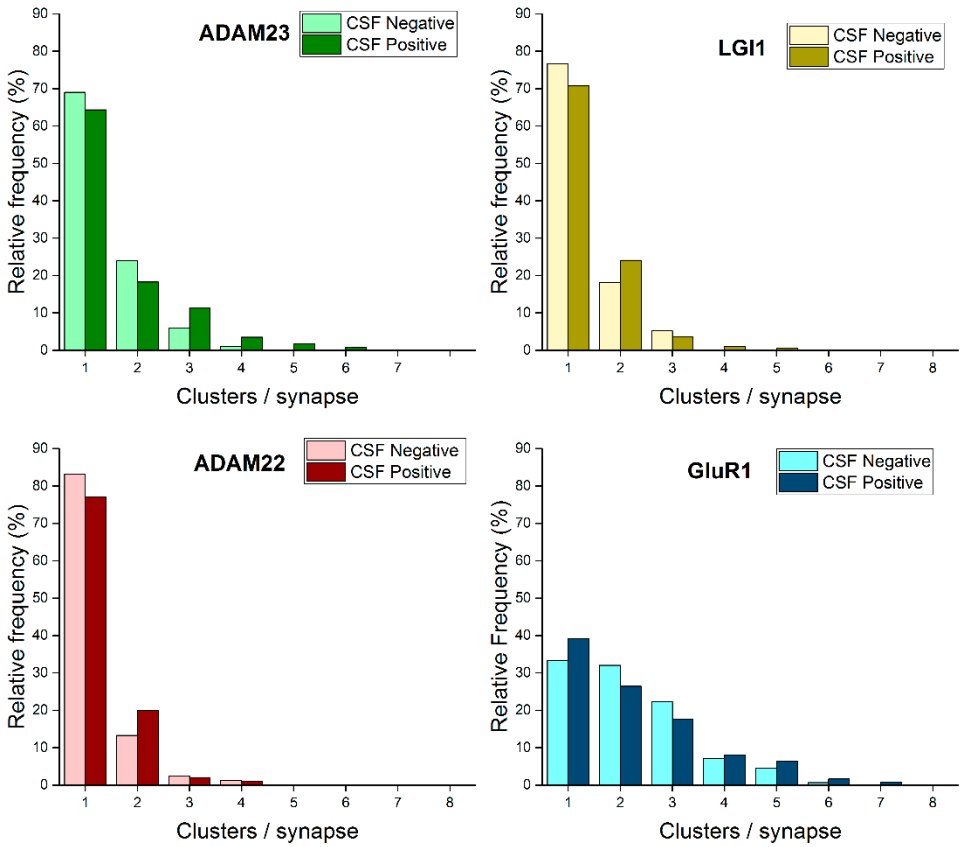

Figure 4.15. Relative frequency of clusters per synapse in control and treated conditions. For CSF negative data. *ADAM23: 69.0% with 1 cluster, 24.0% with 2 clusters, 6.0 with 3 clusters and 1.0% with 4 clusters, out of 100 synapses. LGI1: 76.6% with 1 cluster, 18.1% with 2 clusters and 5.2% with 3 clusters out of 154 synapses. ADAM22: 83.3% with 1 cluster, 13.1% with 2 clusters and 2.4% with 3 clusters and 1.2 with 4 clusters out of 84 synapses. GluR1: 33.3% with 1 cluster, 32.0% with 2 clusters, 22.2% with 3 clusters, 7.2% with 4 clusters, 4.6% with 5 clusters and 0.7% with 6 clusters out of 153 synapses. For CSF Positive data: ADAM23: 64.4% with 1 cluster, 18.3% with 2 clusters, 11.3 with 3 clusters, 3.5% with 4 clusters, 1.7% with 5 clusters and 0.87 with 6 clusters, out of 115 synapses. LGI1: 70.7% with 1 cluster, 24.1% with 2 clusters, 3.7% with 3 clusters, 1.0% with 4 clusters and 0.5% with 5 clusters out of 191 synapses. ADAM22: 77.0% with 1 cluster, 20.0% with 2 clusters, 2.0% with 3 clusters and 1.0% with 4 clusters out of 100 synapses. GluR1: 39.2% with 1 cluster, 26.4% with 3 clusters, 17.6% with 3 clusters, 8.0% with4 clusters, 6.4% with 5 clusters, 1.6% with 6 clusters and 0.8% with 7 clusters out of 125 synapses.*

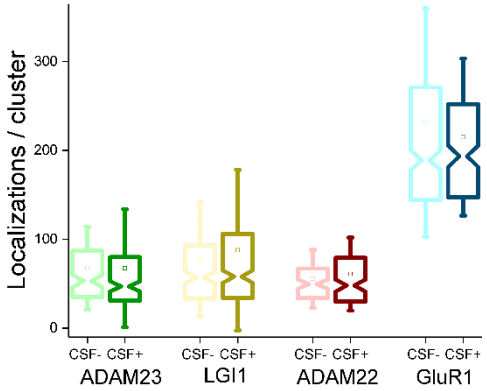

Figure 4.16. Number of localizations per cluster in control and treated conditions. *The notched distribution shows the IQR (box), the notch (95% confidence interval of the median), the median (center of the notch) and the mean (dot). The whiskers represent the standard deviation. For CSF Negative (**CSF -**) data (Median/IQR): ADAM23: 53/52 (n = 139). LGI1: 57/60 (n = 198). ADAM22: 49.5/33 (n = 102). GluR1: 189/127 (n = 336). For CSF positive (**CSF +**) (Median/IQR): ADAM23: 47/49 (n = 187). LGI1: 58/72 (n = 261). ADAM22: 48/49 (n = 127). GluR1: 193.5/105 (n = 186).*

Finally, we determined the organization of the main proteins in the LGI1 complex after treatment with LGI1 autoantibodies. The position of the various proteins within the synapse was similar for negative control (CSF-) and no treatment (**Figures 4.17** and **4.13**).

Interestingly, after treatment, the position of the pre-synaptic protein ADAM23 significantly changed while all the other proteins maintained their synaptic localization. The change in ADAM23 position was not due to a change in the synapse structure since Homer and Bassoon had a similar distance distribution in treated and control neurons (**Figure 4.18**).

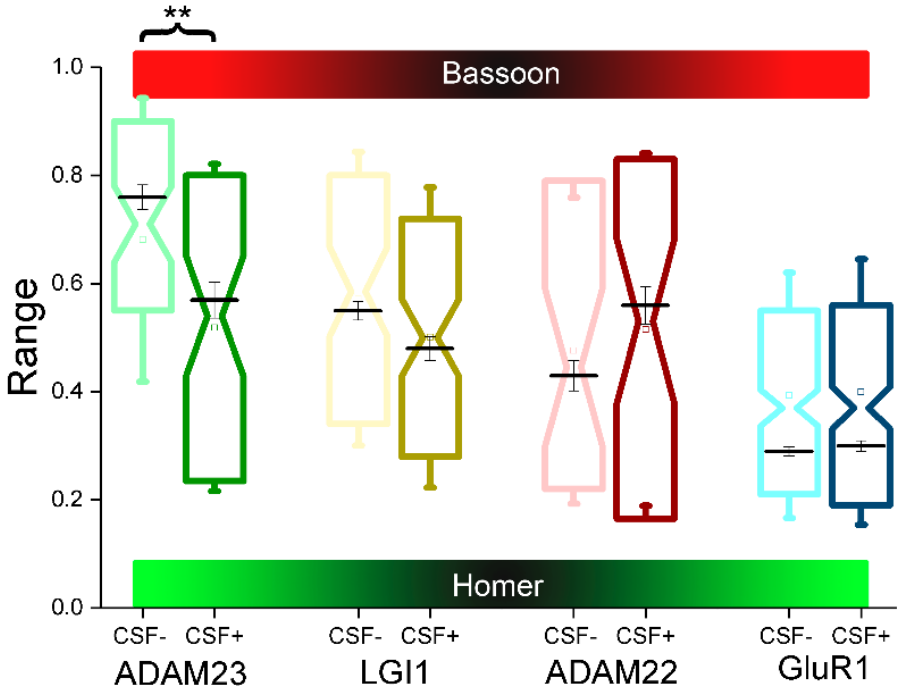

Figure 4.17. Relative distance distributions of the LGI1 complex proteins in control and treated conditions. *The notched distribution shows the IQR (box), the notch (95% confidence interval of the median), the median (center of the notch) and the mean (dot). The colored whiskers represent the standard deviation. The Medians/IQRs are: For CSF negative (CSF -): ADAM23: 0.71/0.35 (n = 61), LGI1: 0.59/ 0.46 (n = 78), ADAM22: 0.45/0.57 (n = 38), GluR1: 0.37/0.34 (n = 258). For CSF positive (CSF+): ADAM23: 0.54/0.57 (n = 64), LGI1: 0.50/0.44 (n = 93), ADAM22: 0.53/0.67 (n = 48), GluR1: 0.37/0.37 (n = 229) and comparison of the individual synapse analysis with the super-synapse analysis in control and treated conditions. The values of the relative distance extracted from the super-synapses are represented by the black line with the whiskers being the standard error. For CSF negative data (CSF-), the values are: ADAM23: 0.76+/-0.02 (n = 52), LGI1: 0.55+/-=0.02 (n = 71), ADAM22: 0.43+/-0.03 (n = 35), GluR1: 0.29+/-0.01 (n = 154). For CSF positive data (CSF+), the values are: ADAM23: 0.57+/-0.03 (n = 54), LGI1: 0.48+/-0.02 (n = 81), ADAM22: 0.56+/-0.04 (n = 46), GluR1: 0.3+/-0.01 (n = 136).*

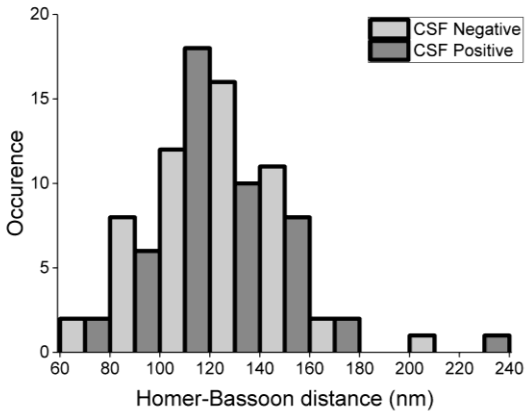

Figure 4.18. Homer-Bassoon distances distributions for control and treated data. *Histogram of the distribution of distances between the centers of mass of the Homer and Bassoon clusters for synapses containing at least one cluster of LGI1 within them in the case of CSF negative (light gray) and CSF positive (dark gray). The distributions do not show a visible change.*

It is possible that LGI1 acts as a spacer between ADAM22 and ADAM23. The LGI1 autoantibodies may interfere more strongly with the binding of LGI1 to the pre-synaptic ADAM23 leading to its mis-localization within the pre-synapse. The stronger effect of LGI1 on the pre-synapse is further supported by results from our collaborator's lab (Josep Dalmau) showing that LGI1 autoantibodies also effect the nanoscale organization of Kv1.1.

In conclusion, the analysis of the relative distances revealed a significant change in the presynaptic side, particularly in ADAM23 position after treatment with LGI1 autoantibodies.

These results were further supported by the super-synapse analysis in which localizations from all synapses were merged together prior to determining the protein positions and ADAM23 showed a significant change in its distribution in the synapse (**Figure 4.19**). On the contrary, the distributions of LGI1, ADAM22 and GluR1 did not show a significant change, as it was already found in the case of the individual synapses. With this analysis, we validated again the results obtained by taking the distributions of individual synapses.

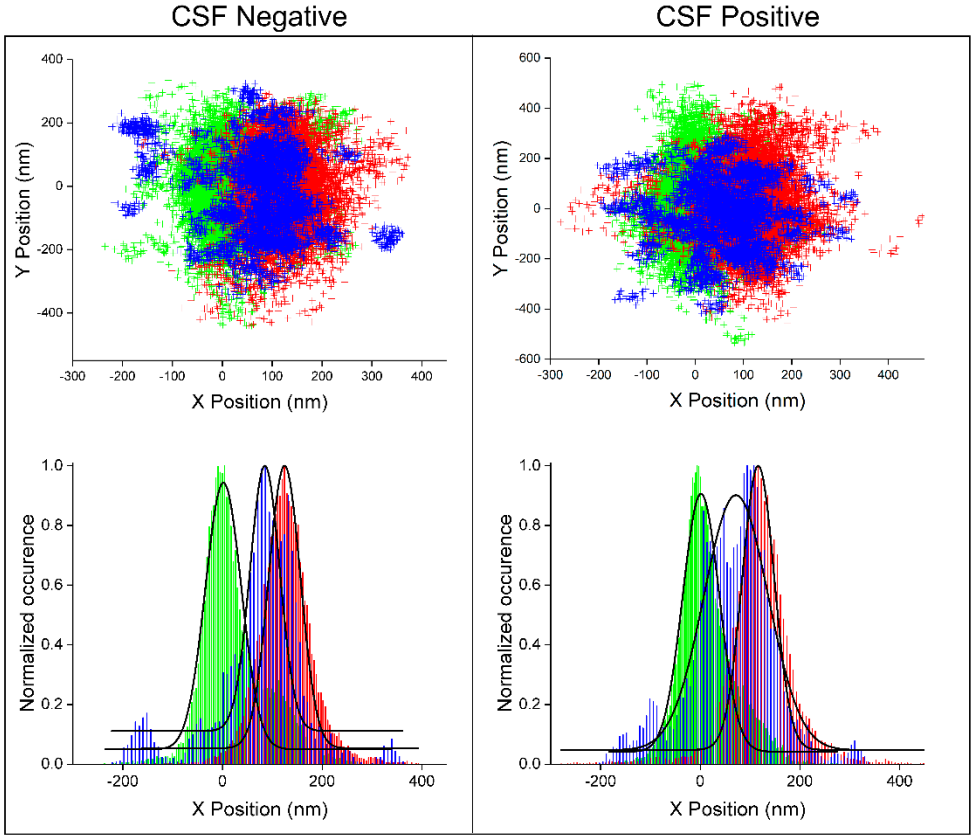

Figure 4.19. ADAM23 super-synapse in control and treated conditions. *Reconstruction of the super-synapse of ADAM23 in CSF negative data (top-left) with a merger of n = 52 synapses and histogram of the projection of the localizations in the x axis (bottom-left) and in CSF positive data (top-right) with a merger of n = 54 synapses and histogram of the projection of the localizations in the x axis (bottom-right) showing Homer (green), Bassoon (red) and ADAM23 (blue).*

4.4. Discussion and conclusions

The organization of the LGI1 complex has not been visualized in individual synapses before. Biochemical methods lack spatial context and cannot be used to study the sub-cellular distribution and synaptic localization of proteins. These methods also cannot capture the heterogeneity of individual synapses and may mask subtle effects of autoantibodies at the synaptic level. To overcome these challenges, here

we visualized 5 different proteins within the LGI1 complex using super-resolution microscopy. We determined the nanoscale organization and localization of these proteins with respect to synaptic reference proteins Homer and Bassoon.

Our results showed that only a small subset of synapses likely contain all 5 proteins of the LGI1 complex. Most proteins organize as small nano-sized clusters within the synapse and in most cases, all the protein is localized inside a single or at most two nano-clusters. An exception to this was GluR1 subunit of AMPA receptor, which organized into several nano-clusters in synapses. Similar organization of AMPA receptors in such nano-domains was previously observed using super-resolution microscopy. The nano-clusters of most proteins contained a similar number of localizations corresponding likely to similar amount of protein within the nanoclusters.

Interestingly, treatment with LGI1 autoantibodies had very small effects on the nano-cluster organization of the various proteins in the LGI1 complex. The most severe effect was observed as a change in the localization of the pre-synaptic ADAM23 protein with respect to Homer and Bassoon. ADAM23 was mis-localized further away from the Bassoon protein after treatment with LGI1 autoantibodies. Surprisingly, none of the post-synaptic proteins were affected by LGI1 autoantibodies. Hence, our results suggest that autoantibodies likely have a stronger effect in the interaction of LGI1 with the pre-synaptic proteins.

Methods

Neuronal culture

E18 Wistar rats were used for the extraction of neurons. The rats were dissected after 18 days of pregnancy under standard ethically proved conditions using CO^2. Primary hippocampal neurons were extracted. The disaggregation was performed mechanically and with 0.20 % tripsin in Hanks' Balanced Salt Solution (HBSS) buffer (Sigma-Aldrich, St Louis, MO) for 15 min at 37°C, washed twice in HBSS buffer for 5min and mechanically disaggregated by pipette suction in high glucose DMEM medium (complemented with 10% Horse Serum, 10 % Fetal Bovine Serum, 1 % L-Glutamine, 1 % Penicillin-Streptomycin and 1% Sodium Pyruvate) (Sigma-Aldrich). Neurons were plated at 120 000 cells per Corning 35 mm (P35) dishes (Sigma-Aldrich) in Neurobasal medium supplemented with B-27 Supplement (Thermo-Fisher, Waltham, MA) on poly-L-lysine-coated (Sigma-Aldrich) coverslips. Neurons were cultured in an incubator for 14 days at 37ºC and 5 % of CO^2.

Immunostaining and Imaging

After the incubation, the neurons were fixed using 4 % paraformaldehyde (PFA) in PBS for 5min at 4ºC. Immunostaining of antibodies from transmembrane proteins, such as ADAM22 and 23, Kv1.1 and the secreted protein LGI1 was performed before the permeabilization of the cells. 1 % of bovine serum albumin in PBS was used as the buffer for the antibody immunostaining at room temperature for 1h, except for the immunostaining of antiLGI1, which was done overnight at 4ºC due to the particularity of the Ab.

v/v Triton X-100 (Sigma-Aldrich) in PBS was used to permeabilize the neurons for 10min at room temperature. After that, neurons were incubated for 1h at room temperature with the antibodies against intracellular proteins, namely GluR1,

Homer1 and Bassoon. Finally, a custom built secondary antibody was added. Table 4.1 shows a summary of the primary antibodies used in the immunostaining, with each of the targeted proteins, its corresponding species and the concentration used with respect to the original batch.

Targeted protein	Kv1.1	ADAM23	LGI1	ADAM22	GluR1
Species	mouse	rabbit	human	rabbit	rabbit
Company	MERCK	AbCam	NA	AbCam	AbCam
Concentration	1/10	1/200	1/50	1/50	1/800

Targeted protein	Homer1	Homer1b,c	Bassoon	Bassoon
Species	guinea pig	rabbit	mouse	guinea pig
Company	Synaptic Systems	Thermo Scientific Pierce	ENZO	Synaptic Systems
Concentration	1/200	1/200	1/400	1/800

Table 4.1. Antibodies used for immunostaining.

Due to the problems with cross-talk, we tried 3 different methods:

1. Different labeling strategy - In this method, Homer and Bassoon were imaged with organic dye-pairs (Cy3/AF647 and AF405/AF647) and the third protein was labeled with Atto488, a green fluorescent dye. However, this dye did not perform in an optimal way for STORM. The imaging showed a very poor blinking rate and the reconstructed image had a very low localization precision. This can be due to the fact that the imaging buffer was optimized for the emission and blinking of AF647 and not for Atto488. As mentioned in Chapter 2, it has been proven that optimization of the imaging buffer for each individual dye is crucial for an acceptable performance in STORM, giving a precise localization of the image (Dempsey

et al., 2011, Olivier et al., 2013, Nahidiazar et al., 2016). Therefore, we looked for another method.

2. Sequential labeling and imaging strategy - Following the method developed in the lab (Tam et al., 2014), we started with a STORM image of LGI1 with the AF405-AF647 dye pair and then, we applied a reducing agent (sodium borohydride) to quench the remaining fluorescent dyes and immunostained the sample again directly in the stage with antibodies against Homer and Bassoon with two dye pairs, Cy3-AF647 and AF405-AF647. However, the quenching seemed to cause a disturbance on the sample because the image of Bassoon was always highly deteriorated, so we also discarded to go forward with this method.
3. Sequential imaging strategy – In that case, we decided to separate the STORM imaging in two sequences. The first STORM sequence was to image Homer and Bassoon with Cy3-AF647 and Cy2-AF647, respectively. After that, a STORM image of the protein of the complex was taken using AF405-AF647. By carefully tuning the powers of the activation lasers we were able to obtain an image of the 3 different proteins without overlap or bleaching of any of them. Some minimal cross-talk remained between Homer and Bassoon but could be corrected later on in the data analysis. Fiduciary markers were used to overlap the two separated sequences into a reconstructed image containing the localizations of the 3 channels.

To visualize Kv1.1, ADAM23, LGI1, ADAM22 and GluR1, the secondary included the dye pair AF405/AF647 with 4-5 dyes to 1 ratio. To visualize Homer and Bassoon, Cy3/AF647 and Cy2/AF647 dye pairs were used, with ratios of 4-5 dyes to 1 and 2-3 dyes to 1, respectively.

In order to be able to merge sequential images, we added fiduciary markers such as nile-red beads of 110 nm diameter at concentration 1/5000 in PBS right after the immunostaining and we let the samples to chill for at least 2h.

Imaging was performed using a previously described imaging buffer (Cysteamine MEA [Sigma-Aldrich, #30070-50G], Glox Solution: 0.5 mg/ml glucose oxidase, 40 mg/ml catalase [all Sigma-Aldrich], 10 % Glucose in PBS) (Bates et al., 2007).

Images were acquired in a commercial Nikon Ti-E NSTORM with a 100x 1.49 NA oil-immersion objective, filtered by an emission filter (ET705/72m), and imaged onto an Andor electron multiplying charge coupled device (EMCCD) camera at an exposure time of 20 ms per frame. The excitation was given by an Argilent laser box fiber coupled to the back focal plane of the microscope. Sequential imaging was used in order to avoid cross-talk from Cy2 into the AF405 imaging. First of all, STORM images of Homer and Bassoon were collected with a sequence of 1 activator frame for 560 laser and 4 reporter frames for 647 laser followed by 1 activator frame for 488 laser and 4 reporter frames for 647 laser. Each frame had a duration of 20ms. Cycles of these sequence were repeated until 15 000 to 20 000 frames were reached. 647 was kept at a constant power of 55 mW all the time, while 560 and 488 were increased stepwise from 0.002 to 0.5mW. After that, a STORM image of the protein of interest, being Kv1.1, ADAM23, LGI1, ADAM22 or GluR1, was acquired using 405 nm laser light in stepwise increments of power from 0.006 to 0.13 mW. In this case, the cycle only consisted of 1 activator frame of 405 and 4 reporter frames of 647 laser.

Data Reconstruction

The image reconstruction was obtained using a custom-built STORM analysis program (Insight3) kindly provided by Dr Bo Huang. Gaussian fitting of the PSF coming from the dyes attached to the protein provided the localizations of the 3 different channels. The localizations of the 2 different sequences were merged in Insight3 program. In the cases were the drift correction was not enough, we transformed the localizations of the second image using the localizations of the

fiduciary markers and a custom-built plugin in ImageJ by means of a first order polynomial affine transformation.

Individual synapse data analysis

Once the reconstruction of the 3 channels, Homer, Bassoon and the protein of interest was set, we manually selected the ROIs corresponding to individual synapses with a plugin in ImageJ. We then used a custom-built cluster analysis software written in our lab (Ricci et al., 2015) to extract individual clusters for each of the channels. For Homer and Bassoon, we took a minimum of 80 localizations to be considered a cluster, whereas for Kv1.1, ADAM23, LGI1 and ADAM22, only 20 localizations were enough. On the contrary, GluR1 is much more abundant in synapses and the minimum was set to 120 localizations in this case. Another custom-built program written in Matlab code allowed us to group the clusters of the three channels that were nearby to treat them as individual synapses. These grouped clusters were considered as single "objects" for further analysis. We selected the synapses that were having the center of mass of the cluster of Homer and the cluster of Bassoon between 60 nm and 250 nm of distance and the clusters of the protein of interest not further than 300 nm distance and did not contain Homer and Bassoon clusters highly overlapped with each other to rule out synapses not being parallel to the image plane. We also calculated the number of localizations per cluster, the number of clusters of the protein of interest in each "synapse-object". After that, we rotated these objects, so that they would all be parallel to one reference axis. We projected the localizations of the 3 channels into histograms perpendicular to this reference axis of the synapse and fitted the histograms into Gaussian distributions. The number of bins was set to be the square root of the number of total data points. In order to discard remaining cross-talk, we fitted the data into

single, double or triple Gaussian distributions and took the one that matched the best. Then, we chose the highest peak of the fitting to be the one considered for data analysis. By measuring the peak-to-peak distance of the Gaussian fittings in the 3 channels, we extracted the Homer-Bassoon distance and the Homer-Protein distance for each of the clusters. In order for the analysis not to be influenced by the different widths of the synapses, we divided the Homer-Protein distance by the Homer-Bassoon distance to normalize these different widths. We then obtained a relative distance of the different proteins with respect to Homer (in position 0) and Bassoon (in position 1). From these individual objects, we also extracted the number of clusters of the protein of interest per synapse, the Homer-Bassoon distance, the Homer-Protein distance and the number of localizations per cluster of the 3rd protein.

"Super-synapse" data analysis

In order to correct for synapses that were not completely parallel to the image plane and user error rotations, we performed a second analysis. We first selected the individual synapses that satisfied two conditions: their distance between the centers of mass of Homer and Bassoon clusters was within the range 60-200 nm and they contained at least one cluster of the protein of interest between the peaks of the histograms of Homer and Bassoon. We then took the localizations coming from the 3 channels and merged them together in what we called a "super-synapse". By this means we could average all clusters into 3, each of them corresponding to a different channel, Homer, Bassoon and the 3rd protein. Using all the localizations we could project them again into 3 histograms and measure the peak-to-peak relative distance and its error using error propagation. We performed this analysis for the 5 proteins considered in the LGI1 complex in non-treated conditions as well as in treated conditions except for the case of Kv1.1.

CSF samples and treatments

For treated data, samples of CSF from patients with high titer of LGI1 antibodies (CSF+) were used. The reactivity of the LGI1 autoantibodies contained in the CSF+ was tested by our collaborators using 3 methods: 1) cell base assays (CBA) using Hek cells expressing LGI1 and immunostaining with patient LGI1 antibody and commercial antibody confirmed their colocalization in confocal imaging, 2) the use of immunohistochemistry of the LGI1 antibody from patients in brain tissue of rat and mice showed a specific pattern and 3) experiments in live neurons showed that the LGI1 autoantibody binds extracellularly.

The neuronal cultures were treated with CSF+ for 14 days to determine the effects of the patients' antibodies. Samples of CSF from subjects lacking antibodies that target LGI1 were used as controls (CSF-). The treatment consisted in adding 40 µl of patients' or control CSF to the cultured hippocampal neurons P35 plates containing 1 ml of Neurobasal medium supplemented with B-27 Supplement (Thermo-Fisher). After 14 days of incubation, three dishes were selected for experiments. In one petri dish, the conditions were not altered. In a second dish, neurons were treated with a CSF that was tested negative against all the 16 proteins identified in the encephalitis associated with antibodies, as used in previous studies (Planagumà et al., 2015). Finally, in the third dish, the cells were treated with the CSF against LGI1. All three dishes were kept for three days in the incubator at 37ºC under these conditions. After this time, all the cells were fixed with 4 % PFA for 5 min at 4ºC, like in the case of the healthy conditions. The immunostaining was also performed following exactly the same procedure, as well as the imaging. Once the treatment was completed, cultures were washed with phosphate buffered saline (PBS). Written consent for studies was obtained from patients or from families if patients were judged unable to give consent. Studies were approved by the institutional review board of Hospital Clínic and Institut d'Investigacions Biomèdiques August Pi i Sunyer (IDIBAPS), Universitat de Barcelona.

References

Ariño, H., Armangué, T., Petit-Pedrol, M., Sabater, L., Martinez-Hernandez, E., Hara, M., Lancaster, E., Saiz, A., Dalmau, J. and Graus, F. (2016) 'Anti-LGI1-associated cognitive impairment: Presentation and long-term outcome', *Neurology,* 87(8), pp. 759-65.

Bates, M., Huang, B., Dempsey, G. T. and Zhuang, X. (2007) 'Multicolor super-resolution imaging with photo-switchable fluorescent probes', *Science,* 317(5845), pp. 1749-53.

Chabrol, E., Navarro, V., Provenzano, G., Cohen, I., Dinocourt, C., Rivaud-Péchoux, S., Fricker, D., Baulac, M., Miles, R., Leguern, E. and Baulac, S. (2010) 'Electroclinical characterization of epileptic seizures in leucine-rich, glioma-inactivated 1-deficient mice', *Brain,* 133(9), pp. 2749-62.

Chen, L., Chetkovich, D. M., Petralia, R. S., Sweeney, N. T., Kawasaki, Y., Wenthold, R. J., Bredt, D. S. and Nicoll, R. A. (2000) 'Stargazin regulates synaptic targeting of AMPA receptors by two distinct mechanisms', *Nature,* 408(6815), pp. 936-43.

Chernova, O. B., Somerville, R. P. and Cowell, J. K. (1998) 'A novel gene, LGI1, from 10q24 is rearranged and downregulated in malignant brain tumors', *Oncogene,* 17(22), pp. 2873-81.

Dalmau, J., Geis, C. and Graus, F. (2017) 'Autoantibodies to Synaptic Receptors and Neuronal Cell Surface Proteins in Autoimmune Diseases of the Central Nervous System', *Physiol Rev,* 97(2), pp. 839-887.

Dalmau, J., Tüzün, E., Wu, H. Y., Masjuan, J., Rossi, J. E., Voloschin, A., Baehring, J. M., Shimazaki, H., Koide, R., King, D., Mason, W., Sansing, L. H., Dichter, M. A., Rosenfeld, M. R. and Lynch, D. R. (2007) 'Paraneoplastic anti-N-methyl-D-aspartate receptor encephalitis associated with ovarian teratoma', *Ann Neurol,* 61(1), pp. 25-36.

Dani, A., Huang, B., Bergan, J., Dulac, C. and Zhuang, X. (2010) 'Superresolution imaging of chemical synapses in the brain', *Neuron,* 68(5), pp. 843-56.

de Bellescize, J., Boutry, N., Chabrol, E., André-Obadia, N., Arzimanoglou, A., Leguern, E., Baulac, S., Calender, A., Ryvlin, P. and Lesca, G. (2009) 'A novel three base-pair LGI1 deletion leading to loss of function in a family with autosomal dominant lateral temporal epilepsy and migraine-like episodes', *Epilepsy Res,* 85(1), pp. 118-22.

Dempsey, G. T., Vaughan, J. C., Chen, K. H., Bates, M. and Zhuang, X. (2011) 'Evaluation of fluorophores for optimal performance in localization-based super-resolution imaging', *Nat Methods,* 8(12), pp. 1027-36.

Di Bonaventura, C., Operto, F. F., Busolin, G., Egeo, G., D'Aniello, A., Vitello, L., Smaniotto, G., Furlan, S., Diani, E., Michelucci, R., Giallonardo, A. T., Coppola, G. and Nobile, C. (2011) 'Low penetrance and effect on protein

secretion of LGI1 mutations causing autosomal dominant lateral temporal epilepsy', *Epilepsia,* 52(7), pp. 1258-64.

Fukata, Y., Adesnik, H., Iwanaga, T., Bredt, D. S., Nicoll, R. A. and Fukata, M. (2006) 'Epilepsy-related ligand/receptor complex LGI1 and ADAM22 regulate synaptic transmission', *Science,* 313(5794), pp. 1792-5.

Fukata, Y., Lovero, K. L., Iwanaga, T., Watanabe, A., Yokoi, N., Tabuchi, K., Shigemoto, R., Nicoll, R. A. and Fukata, M. (2010) 'Disruption of LGI1-linked synaptic complex causes abnormal synaptic transmission and epilepsy', *Proc Natl Acad Sci U S A,* 107(8), pp. 3799-804.

Graus, F., Titulaer, M. J., Balu, R., Benseler, S., Bien, C. G., Cellucci, T., Cortese, I., Dale, R. C., Gelfand, J. M., Geschwind, M., Glaser, C. A., Honnorat, J., Höftberger, R., Iizuka, T., Irani, S. R., Lancaster, E., Leypoldt, F., Prüss, H., Rae-Grant, A., Reindl, M., Rosenfeld, M. R., Rostásy, K., Saiz, A., Venkatesan, A., Vincent, A., Wandinger, K. P., Waters, P. and Dalmau, J. (2016) 'A clinical approach to diagnosis of autoimmune encephalitis', *Lancet Neurol,* 15(4), pp. 391-404.

Hutchinson, M., Waters, P., McHugh, J., Gorman, G., O'Riordan, S., Connolly, S., Hager, H., Yu, P., Becker, C. M. and Vincent, A. (2008) 'Progressive encephalomyelitis, rigidity, and myoclonus: a novel glycine receptor antibody', *Neurology,* 71(16), pp. 1291-2.

Kalachikov, S., Evgrafov, O., Ross, B., Winawer, M., Barker-Cummings, C., Martinelli Boneschi, F., Choi, C., Morozov, P., Das, K., Teplitskaya, E., Yu, A., Cayanis, E., Penchaszadeh, G., Kottmann, A. H., Pedley, T. A., Hauser, W. A., Ottman, R. and Gilliam, T. C. (2002) 'Mutations in LGI1 cause autosomal-dominant partial epilepsy with auditory features', *Nat Genet,* 30(3), pp. 335-41.

Kobe, B. and Kajava, A. V. (2001) 'The leucine-rich repeat as a protein recognition motif', *Curr Opin Struct Biol,* 11(6), pp. 725-32.

Lai, M., Hughes, E. G., Peng, X., Zhou, L., Gleichman, A. J., Shu, H., Matà, S., Kremens, D., Vitaliani, R., Geschwind, M. D., Bataller, L., Kalb, R. G., Davis, R., Graus, F., Lynch, D. R., Balice-Gordon, R. and Dalmau, J. (2009) 'AMPA receptor antibodies in limbic encephalitis alter synaptic receptor location', *Ann Neurol,* 65(4), pp. 424-34.

Lai, M., Huijbers, M. G., Lancaster, E., Graus, F., Bataller, L., Balice-Gordon, R., Cowell, J. K. and Dalmau, J. (2010) 'Investigation of LGI1 as the antigen in limbic encephalitis previously attributed to potassium channels: a case series', *Lancet Neurol,* 9(8), pp. 776-85.

Lancaster, E. and Dalmau, J. (2012) 'Neuronal autoantigens--pathogenesis, associated disorders and antibody testing', *Nat Rev Neurol,* 8(7), pp. 380-90.

Lancaster, E., Lai, M., Peng, X., Hughes, E., Constantinescu, R., Raizer, J., Friedman, D., Skeen, M. B., Grisold, W., Kimura, A., Ohta, K., Iizuka, T., Guzman, M., Graus, F., Moss, S. J., Balice-Gordon, R. and Dalmau, J. (2010) 'Antibodies

to the GABA(B) receptor in limbic encephalitis with seizures: case series and characterisation of the antigen', *Lancet Neurol,* 9(1), pp. 67-76.

Lancaster, E., Martinez-Hernandez, E. and Dalmau, J. (2011) 'Encephalitis and antibodies to synaptic and neuronal cell surface proteins', *Neurology,* 77(2), pp. 179-89.

Lau, C. G. and Zukin, R. S. (2007) 'NMDA receptor trafficking in synaptic plasticity and neuropsychiatric disorders', *Nat Rev Neurosci,* 8(6), pp. 413-26.

Morante-Redolat, J. M., Gorostidi-Pagola, A., Piquer-Sirerol, S., Sáenz, A., Poza, J. J., Galán, J., Gesk, S., Sarafidou, T., Mautner, V. F., Binelli, S., Staub, E., Hinzmann, B., French, L., Prud'homme, J. F., Passarelli, D., Scannapieco, P., Tassinari, C. A., Avanzini, G., Martí-Massó, J. F., Kluwe, L., Deloukas, P., Moschonas, N. K., Michelucci, R., Siebert, R., Nobile, C., Pérez-Tur, J. and López de Munain, A. (2002) 'Mutations in the LGI1/Epitempin gene on 10q24 cause autosomal dominant lateral temporal epilepsy', *Hum Mol Genet,* 11(9), pp. 1119-28.

Nahidiazar, L., Agronskaia, A. V., Broertjes, J., van den Broek, B. and Jalink, K. (2016) 'Optimizing Imaging Conditions for Demanding Multi-Color Super Resolution Localization Microscopy', *PLOS ONE,* 11(7), pp. e0158884.

Nair, D., Hosy, E., Petersen, J. D., Constals, A., Giannone, G., Choquet, D. and Sibarita, J. B. (2013) 'Super-resolution imaging reveals that AMPA receptors inside synapses are dynamically organized in nanodomains regulated by PSD95', *J Neurosci,* 33(32), pp. 13204-24.

Navarro, V., Kas, A., Apartis, E., Chami, L., Rogemond, V., Levy, P., Psimaras, D., Habert, M. O., Baulac, M., Delattre, J. Y., Honnorat, J. and collaborators (2016) 'Motor cortex and hippocampus are the two main cortical targets in LGI1-antibody encephalitis', *Brain,* 139(Pt 4), pp. 1079-93.

Nicoll, R. A., Tomita, S. and Bredt, D. S. (2006) 'Auxiliary subunits assist AMPA-type glutamate receptors', *Science,* 311(5765), pp. 1253-6.

Nobile, C., Michelucci, R., Andreazza, S., Pasini, E., Tosatto, S. C. and Striano, P. (2009) 'LGI1 mutations in autosomal dominant and sporadic lateral temporal epilepsy', *Hum Mutat,* 30(4), pp. 530-6.

Ohkawa, T., Fukata, Y., Yamasaki, M., Miyazaki, T., Yokoi, N., Takashima, H., Watanabe, M., Watanabe, O. and Fukata, M. (2013) 'Autoantibodies to epilepsy-related LGI1 in limbic encephalitis neutralize LGI1-ADAM22 interaction and reduce synaptic AMPA receptors', *J Neurosci,* 33(46), pp. 18161-74.

Olivier, N., Keller, D., Gönczy, P. and Manley, S. (2013) 'Resolution doubling in 3D-STORM imaging through improved buffers', *PLoS One,* 8(7), pp. e69004.

Owuor, K., Harel, N. Y., Englot, D. J., Hisama, F., Blumenfeld, H. and Strittmatter, S. M. (2009) 'LGI1-associated epilepsy through altered ADAM23-dependent neuronal morphology', *Mol Cell Neurosci,* 42(4), pp. 448-57.

Planagumà, J., Leypoldt, F., Mannara, F., Gutiérrez-Cuesta, J., Martín-García, E., Aguilar, E., Titulaer, M. J., Petit-Pedrol, M., Jain, A., Balice-Gordon, R.,

Lakadamyali, M., Graus, F., Maldonado, R. and Dalmau, J. (2015) 'Human N-methyl D-aspartate receptor antibodies alter memory and behaviour in mice', *Brain,* 138(Pt 1), pp. 94-109.

Ricci, M. A., Manzo, C., García-Parajo, M. F., Lakadamyali, M. and Cosma, M. P. (2015) 'Chromatin fibers are formed by heterogeneous groups of nucleosomes in vivo', *Cell,* 160(6), pp. 1145-58.

Sagane, K., Hayakawa, K., Kai, J., Hirohashi, T., Takahashi, E., Miyamoto, N., Ino, M., Oki, T., Yamazaki, K. and Nagasu, T. (2005) 'Ataxia and peripheral nerve hypomyelination in ADAM22-deficient mice', *BMC Neurosci,* 6, pp. 33.

Scheel, H., Tomiuk, S. and Hofmann, K. (2002) 'A common protein interaction domain links two recently identified epilepsy genes', *Hum Mol Genet,* 11(15), pp. 1757-62.

Schulte, U., Thumfart, J. O., Klöcker, N., Sailer, C. A., Bildl, W., Biniossek, M., Dehn, D., Deller, T., Eble, S., Abbass, K., Wangler, T., Knaus, H. G. and Fakler, B. (2006) 'The epilepsy-linked Lgi1 protein assembles into presynaptic Kv1 channels and inhibits inactivation by Kvbeta1', *Neuron,* 49(5), pp. 697-706.

Senechal, K. R., Thaller, C. and Noebels, J. L. (2005) 'ADPEAF mutations reduce levels of secreted LGI1, a putative tumor suppressor protein linked to epilepsy', *Hum Mol Genet,* 14(12), pp. 1613-20.

Shepherd, J. D. and Huganir, R. L. (2007) 'The cell biology of synaptic plasticity: AMPA receptor trafficking', *Annu Rev Cell Dev Biol,* 23, pp. 613-43.

Staub, E., Pérez-Tur, J., Siebert, R., Nobile, C., Moschonas, N. K., Deloukas, P. and Hinzmann, B. (2002) 'The novel EPTP repeat defines a superfamily of proteins implicated in epileptic disorders', *Trends Biochem Sci,* 27(9), pp. 441-4.

Striano, P., Busolin, G., Santulli, L., Leonardi, E., Coppola, A., Vitiello, L., Rigon, L., Michelucci, R., Tosatto, S. C., Striano, S. and Nobile, C. (2011) 'Familial temporal lobe epilepsy with psychic auras associated with a novel LGI1 mutation', *Neurology,* 76(13), pp. 1173-6.

Szymborska, A., de Marco, A., Daigle, N., Cordes, V. C., Briggs, J. A. and Ellenberg, J. (2013) 'Nuclear pore scaffold structure analyzed by super-resolution microscopy and particle averaging', *Science,* 341(6146), pp. 655-8.

Tam, J., Cordier, G. A., Borbely, J. S., Sandoval Álvarez, A. and Lakadamyali, M. (2014) 'Cross-talk-free multi-color STORM imaging using a single fluorophore', *PLoS One,* 9(7), pp. e101772.

Tomita, S., Adesnik, H., Sekiguchi, M., Zhang, W., Wada, K., Howe, J. R., Nicoll, R. A. and Bredt, D. S. (2005) 'Stargazin modulates AMPA receptor gating and trafficking by distinct domains', *Nature,* 435(7045), pp. 1052-8.

van Sonderen, A., Thijs, R. D., Coenders, E. C., Jiskoot, L. C., Sanchez, E., de Bruijn, M. A., van Coevorden-Hameete, M. H., Wirtz, P. W., Schreurs, M. W., Sillevis Smitt, P. A. and Titulaer, M. J. (2016) 'Anti-LGI1 encephalitis: Clinical syndrome and long-term follow-up', *Neurology,* 87(14), pp. 1449-1456.

Yu, Y. E., Wen, L., Silva, J., Li, Z., Head, K., Sossey-Alaoui, K., Pao, A., Mei, L. and Cowell, J. K. (2010) 'Lgi1 null mutant mice exhibit myoclonic seizures and CA1 neuronal hyperexcitability', *Hum Mol Genet,* 19(9), pp. 1702-11.

Chapter 5

Conclusions and future perspectives

The field of neuroscience covers a very wide range of research areas. From studies of the whole nervous system to single-protein measurements, neuroscientists try to understand the mechanisms that drive neuronal transmission, brain function and disease mechanisms. Despite the enormous amount of progress that has been achieved, there is still a remarkable number of unresolved questions.

Many of the signaling processes in neurons happen at the molecular level, therefore, developing methods and techniques that enable studies at the molecular level have been at the top of the research aims in neuroscience. Over a century, researchers have tried to look at the smallest level possible, but it was not until the advent of electron microscopy that the nanometric level was achieved. Since then, this imaging technique has become routine for neuroscience.

Nevertheless, the fundamental unit of neuron-to-neuron communication is the synapses, a highly dense ensemble of proteins completely packed in a small area. Electron microscopy lacks the molecular specificity necessary to distinguish the identity of the many proteins found at the synapse, making it challenging to visualize its molecular composition and organization. Therefore, it was necessary to develop more specific techniques without losing the resolution in order to perform measurements at the multi-molecular level. With the arrival of fluorescence super-resolution techniques (Hell, 2007, Huang et al., 2010, Lippincott-Schwartz and Patterson, 2009), this limitation was overcome. These nanoscopic techniques opened the window to visualizing the organization of protein assemblies with high spatial resolution and specificity. Multiple examples of fluorescence super-resolution imaging in neuronal cultures were developed in only fixed (Xu et al., 2013) or fixed and live samples (Specht et al., 2013, Nair et al., 2013), as well as in fixed brain slices (Dani et al., 2010) or living tissue (Testa et al., 2012, Urban et al., 2011). With the new developments to visualize the neuronal nanostructures, a higher interest in quantitative measurements at this level has come along.

New tools for quantification at the single-molecule level

With the advent of single-molecule localization super-resolution microscopy, new imaging methods with different capabilities (3D, multi- color) and new analysis methods to reconstruct super-resolution images from raw data and extract quantitative information have been developed. However, due to the complex photophysics of the different fluorescent probes, it still remains quite challenging to count absolute numbers of molecules. While the photophysical properties of the probes, labeling and imaging strategies make image analysis complex, with adequate care, it is possible to measure protein stoichiometry (multimeric, dimeric or oligomeric) (Nan et al., 2013) (Renz et al., 2012), count protein numbers (Lee et al., 2012, Gunzenhäuser et al., 2012, Puchner et al., 2013, Lehmann et al., 2011, Lando et al., 2012, Zanacchi et al., 2017) and characterize the spatial nano-organization of proteins (Sengupta et al., 2013, Scarselli et al., 2012).

For determining absolute protein stoichiometry and sub-cellular protein distribution, the use of fluorescent proteins tagging the protein of interest may be preferable. Whereas antibodies are prone to miscounting due to their tendency to overlabel the targeted proteins in the case of polyclonal ones or to underlabel due to steric hindrance, fluorescent proteins ensure more easily a one-to-one ratio labeling. The special characteristics of the irreversible photoswitchable fluorescent proteins can be used as an advantage for counting in more dense samples, where the separation in time of the detected signal might be necessary for proper counting. However, even some of the irreversible fluorescent proteins can blink multiple times during the imaging (Annibale et al., 2010), giving rise to over-counting if this effect is not previously calibrated. Furthermore, the opposite effect can also happen if the photoactivation efficiency of the fluorescent protein is not characterized. A number of recent papers have used calibration standards to calculate the percentage of successful photoactivation during super-resolution imaging for a number of fluorescent proteins (Nan et al., 2013, Puchner et al., 2013),

but a more complete and thorough analysis regarding the photophysics of these probes was missing.

In this thesis, we developed a new method that allowed us direct counting of targeted molecules calibrating eight fluorescent proteins typically used in PALM imaging: mEos2 and its derivatives, mEos3.1 and 3.2, Dendra2, mClavGR2, mMaple, PAGFP and PA-mCherry. We measured the photoactivation efficiency of these probes *in vivo*, in *Xenopus* oocytes, using the glycine receptor as our template with known stoichiometry. Two approaches were used to characterize the photoactivation efficiency. Firstly, we used single-step photobleaching to determine the percentage of molecules that switched from one fluorescent state to another (either from dark to bright or from two spectrally different states). Additionally, we performed single molecule counting-PALM to validate the results obtained with the first method (**Figure 5.1**).

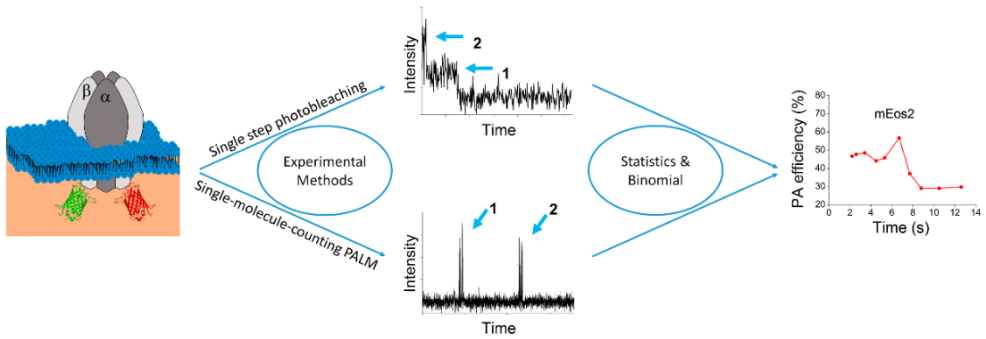

Figure 5.1. Characterization of the fluorescent protein photoactivation efficiency. *The human glycine receptor (GlyR) with fluorescent protein tagged β-subunit and untagged α-subunit expressed in* Xenopus *oocyte membrane is used as nanotemplate. The green fluorescent protein refers to the native form of a photoconvertible fluorescent protein (e.g. mEos2) and the red fluorescent protein refers to the photoconverted form. Single step-photobleaching intensity-time traces can be obtained after photoconversion of the fluorescent proteins. Alternatively, the fluorescent proteins can be imaged with PALM to generate intensity-time traces containing peaks. Steps or peaks in intensity-time traces are counted; sufficient statistics are built and fit to the binomial distribution to obtain the photoactivation efficiency. Shown is the photoactivation efficiency of mEos2 (red line) as a function of the 405-nm illumination exposure.*

The measured photoactivation efficiency of the fluorescent proteins, after the binomial fitting of the counted steps in the case of single-step photobleaching or peaks in the case of single-molecule-counting PALM, was between 50-60 %, depending on the protein. We also confirmed the reactivation of some of them, like mEos2, previously reported by the group of Aleksandra Radenovic (Annibale et al., 2010, Annibale et al., 2011). This photoconvertible protein showed a partial reactivation after photobleaching. This could be due to the fact that the molecule may go to a longer-lived dark state, but the specific reasons still remain unknown. We also showed that there is a fraction of mEos2 and Dendra2 unable to photoconvert that is still fluorescently active possibly due to the unlikely protonation of the native form. Moreover, we detected that the laser light used for PA-GFP imaging also induces photoactivation, making quantitative measurements using this protein very challenging. As a conclusion, we stated that due to their moderate photoactivation and almost non-existent reactivation, PA-mCherry and Dendra2 are the most suitable photoswitchable fluorescent proteins to be used for protein quantification using fluorescence techniques, however, if better photoswitchable fluorescent proteins are developed in the future, our method can be a good way to test their photoactivation efficiency of the new protein and calibrate it for quantitative methods.

With the presented method, it should be possible to measure the number of counted proteins of an unknown complex and measure its stoichiometry with the calibrated probes. However, when the system to study may have more than 6 proteins to be counted, single-step photobleaching may not be very reliable to extract the exact copy number due to the complexity to distinguish single steps. Another limitation would be in the case of using photoswitchable fluorescent proteins with reasonably low photoactivation efficiency, such as 30-40% or lower. In such case, the characterization of the photophysics of the probe would probably not be accurate enough, leading to under-counting of the target protein.

An interesting future outlook would be to study the effects of pH in the photoactivation efficiency of the fluorescent proteins. As mentioned before, oocytes self-regulate their pH, but in our experiments, after removing their membrane we could still observe fluorescent proteins attached to GlyRs. Then, it was easy to modify the pH of the buffer and measure the brightness of the fluorescent proteins under different pH conditions. Our preliminary studies showed a tendency to lower photon count but higher photoactivation efficiency in more acidic media. Precise results of the photoactivation efficiency remained unclear but we could clearly observe an effect, therefore, further experiments in this direction would help to clarify the effects on pH changes. In the case of neurons, synaptic vesicles tend to have a more acidic medium than in the outer medium of the cells. Additionally, synaptic key players such as glutamate receptors or voltage-gated calcium channels show strong pH dependence and effects of pH gradients on synaptic processes are well known. Therefore, the change of pH can be of extreme relevance in the study of neuroreceptor transport or release using fluorescent proteins.

Protein complex organization revealed in super-resolution

Single-molecule localization microscopy has already led to breakthrough discoveries in the molecular architecture of neurons. The combination of 3D conformation with multi-color STORM imaging was used to determine the position of multiple synaptic proteins (Dani et al., 2010). This method was later used to reveal the periodical structure of actin and spectrin in axons (Xu et al., 2013). Following these examples, we aimed to reveal the organization of the LGI1 protein complex in synapses at the nanometer scale.

We started using the same method of 3-color STORM imaging used by Dani et al. (Dani et al., 2010). We took the Homer and Bassoon proteins as our synaptic

references and imaged them together with the proteins of interest of the LGI1 complex (LGI1, ADAM22 and 23, GluR1 and Kv1.1), each one at a time. We encountered important issues regarding color cross-talk and low signal density that made us modify the imaging method to overcome these problems. Instead of imaging the three proteins at once, we separated the imaging in two sequences. Firstly, we imaged the synaptic reference proteins, because of their higher signal density, but without reaching the maximum of laser intensity to prevent bleaching from the protein of interest. After that, we imaged the 3rd protein without reaching the highest power laser light again so that the remaining signal of the active dyes attached to Homer and Bassoon would not become a significant addition to the signal of the protein of interest. This method enabled us to be sure that the signal detected was coming from the expected proteins. Despite this adaptation, cross-talk correction between Homer and Bassoon was still necessary, but due to the fact that they show well-defined structures, the correction was easy to implement.

With the proper data analysis, we were able to extract the molecular organization in super-resolution of the five main proteins of the LGI1 complex in the synapse. Kv1.1 and ADAM23 appeared to be in the presynaptic side whereas ADAM22 and GluR1 were at postsynaptic position, in accordance to the literature. LGI1 appeared to be present in a wide range of the synaptic cleft, possibly validating the bispecific nature of the autoantibody.

Counting the percentage of synapses that contained at least one cluster of the different proteins under study showed us the fact that the LGI1 complex as a whole is very rare in synapses. The most abundant protein is GluR1, the subunit of AMPA receptors, in accordance to the multiple roles associated to this neuroreceptor. This protein showed clearly higher number of clusters per synapse and number of localizations per cluster than any of the other members of the LGI1 complex. From the central proteins of the complex, we found that LGI1 and ADAM23 are present in a similar number of synapses. However, ADAM22 seems to be at one third of the

total synapses. On the contrary, the number of clusters per synapse and localizations per cluster is pretty similar among the three proteins, suggesting a one-to-one stoichiometry between these proteins when all three of them are present in a synapse. Kv1.1 showed a very low presence in synapses and a similar number of localizations and clusters as the ADAMs and LGI1.

Once all the information of the organization was extracted for all the proteins of the LGI1 complex, we proceeded with the treatment of neurons with cerebrospinal fluid (CSF) from patients that tested positive for autoimmune limbic encephalitis against LGI1. As a control, we used CSF from patients that were also examined but tested negative for all the known autoimmune limbic encephalitis. The same exact experiments were performed with the treated conditions for four out of five of the proteins of the LGI1 complex. The data analysis revealed a very significant change in the position of the presynaptic ADAM23, indicating a possible disruption of the ensemble of proteins in the axonal side of the synapse and a tendency of ADAM23 to move towards the center of the synaptic cleft (**Figure 5.2**). On the contrary, this effect was not visible in the postsynaptic side, leading to the suggestion that the binding of LGI1 to the postsynaptic ADAM22 may be more stable than in the case of ADAM23. Additionally, the other extracted parameters such as the number of clusters and localizations did not show a significant change.

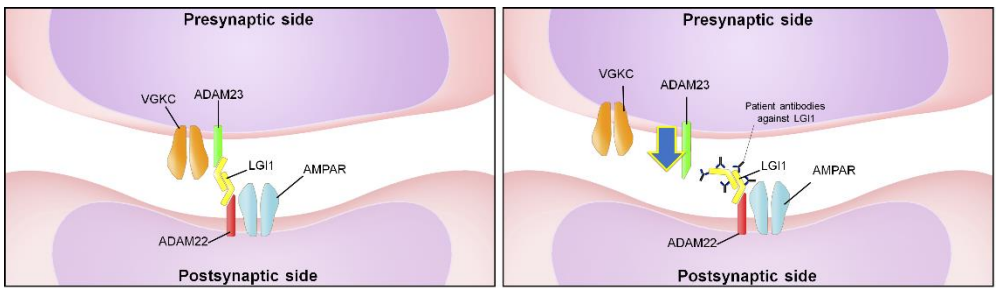

Figure 5.2. Effects of the autoantibodies against LGI1. *On the left side, the synaptic position of the LGI1 protein complex in physiological conditions is presented as indicated by our super-resolution results. On the right side, an interpretation of the effects of the antibodies against LGI1 is given, showing a disruption of the complex, especially in the ADAM23 configuration. Our results show a change in the distribution, going towards the center, probably caused by the disruption of the interaction between ADAM23 and LGI1.*

Our results on the position of the proteins of the LGI1 complex in the synapse were validated with another approach. We took the STORM images of the individual synapses and merged their localizations into what we called a “super-synapse” to give an averaged image of the synaptic distribution. In the case of the treated conditions, the changes in the distribution of ADAM23 along the synaptic cleft were clearly observable, confirming the disruption in the presynaptic side due to the autoantibodies against LGI1. Interestingly, the distribution showed the appearance of a second peak closer to the postsynaptic side, which was not so clearly observed in the individual synapse analysis. Despite that further studies are necessary to explain in more detail what is the machinery that leads to the disruption, this can give an initial idea of what happens at the super-resolution level.

Before achieving these results, we encountered a remarkable number of constrains, mainly associated to regular multi-color imaging issues. The two major limitations have been the low signal density of the targeted proteins and the high cross-talk of the imaging method. The first one was especially important in the case of the main protein of interest under study, LGI1. Commercial primary antibodies were tested unsuccessfully to be imaged for our methods. Only the use of purified autoantibodies from patients tested positive for autoimmune limbic encephalitis gave enough imaging density for reproducible results. The case of ADAM22 and Kv1.1 antibodies was similar, however, despite the low density of signal in STORM experiments, the repeated experiments gave consistent results. Due to these limitations, it would be recommendable to use an alternative method for future quantitative experiments of such proteins. One possibility would be to transiently transfect a plasmid of the protein under study tagged with a fluorescent protein and perform PALM imaging.

Moreover, the cross-talk observed in the first experiments obliged us to look for alternatives before reaching the optimal imaging strategy. As explained in the Methods section of Chapter 4, two different approaches were tested as an

alternative to the method developed by Dani et al. (Dani et al., 2010). On one hand, due to the particular photophysics of the organic dyes, highly dependent on the buffer, we discarded the use of Atto488 combined with the dye pair Cy3-AF647 and AF405-AF647. On the other hand, multi-color imaging done with fully sequential imaging was also discarded because the quenching reagent disrupted the sample. The final successful strategy was the partial sequential STORM imaging, where Homer and Bassoon were imaged before, and the protein of interest right after. This method causes some loss of the localization density because the complete photobleaching is never reached, however, it gains specificity in multiple-color configuration. It particularly works for multi-labeling where the structure of part of the targets is known, like in the case of Homer and Bassoon, which give a very clear image and cross-talk can easily be corrected. Even with low density signal of the 3rd protein, such as LGI1, ADAM22 and Kv1.1, 3-color images were extracted with clear structures for the three channels. However, in cases where all the protein structures are unknown, it can be quite challenging to separate, especially if the sample is not very dense.

In conclusion, this thesis shows that using 3-color STORM imaging, it was possible to unravel the molecular organization of the LGI1 protein complex, not visualized up to date. Furthermore, the same organization was also examined in neurons treated with antibodies targeting LGI1, coming from patients suffering a neurological disorder affecting particularly this complex.

In the future, it would be interesting to look at the copy number of the different proteins of the complex. One possibility would be to combine the method developed in Chapter 3 to perform single-step photobleaching or PALM experiments using fluorescent proteins and correcting the extracted number to the photoactivation efficiency of the fluorescent protein under use. Another possibility would be to determine the counting number with nanobodies, which allow more stoichiometric labeling compared to antibodies. An alternative could be a novel

method developed in the lab characterized the blinking of organic dyes bound to antibodies (Zanacchi et al., 2017). A possible approach would be to transfect neurons with a plasmid of the proteins of the LGI1 complex together with a well-characterized fluorescent protein, GFP for example, and then immunostain it with antibodies containing the previously calibrated organic dye. Adjusting the acquired counting to the calibration, direct protein copy numbers could be extracted.

These methods would allow us to determine the stoichiometry of the complex and the difference between not treated and treated neurons to obtain a closer approach to the causes of the disruption in the synapse produced by the autoantibodies against LGI1.

Additionally, it would also be interesting to determine the effects of the autoantibodies in the direct interaction between the proteins of the complex, such as ADAM23-LGI1 or LGI1-ADAM22 interactions. One idea could be the use of techniques that allow the visualization of effects in very close distances, such as Förster resonance energy transfer (FRET). This method could help us understand more clearly whether there is a disruption in the binding of proteins or a rearrangement of the conformation.

Summary

In this thesis, I have shown a novel application of super-resolution fluorescence microscopy to study molecular organization of synaptic proteins. We demonstrated how it is possible to characterize the molecular organization and stoichiometry, two critical points in neuronal transmission, using this nanoscopic methods.

On one hand, we presented an innovative method, published in Nature Methods (Durisic et al., 2014), to determine the photophysics of photoswitchable fluorescent proteins used in quantitative methods. Characterizing the photoactivation efficiency of such probes would be crucial for the study of protein stoichiometry.

On the other hand, by means of multi-color STORM, we disclosed the molecular organization of the LGI1 complex, a synaptic protein complex that is central in the machinery of autoimmune limbic encephalitis, a severe epilepsy-related disorder where patients produce antibodies against LGI1. We characterized the protein organization of the complex, both in neuronal cultures in physiological conditions and under treatment of cultures with autoantibodies against LGI1 from human patients at the nanometric range.

I am confident that this thesis presents tools to help researchers, especially neuroscientists, to study the protein organization and stoichiometry of different synaptic complexes and particularly puts a starting point for further studies of the autoimmune limbic encephalitis in super-resolution. Unraveling the effects of neurological disorders at the single-molecule level can open a window to understand the causes of such disorders and can thus cause a big impact in the development of therapies of an uncountable number of neuropathies.

References

Annibale, P., Scarselli, M., Kodiyan, A. and Radenovic, A. (2010) 'Photoactivatable Fluorescent Protein mEos2 Displays Repeated Photoactivation after a Long-Lived Dark State in the Red Photoconverted Form', *The Journal of Physical Chemistry Letters,* 1(9), pp. 1506-1510.

Annibale, P., Vanni, S., Scarselli, M., Rothlisberger, U. and Radenovic, A. (2011) 'Quantitative photo activated localization microscopy: unraveling the effects of photoblinking', *PLoS One,* 6(7), pp. e22678.

Dani, A., Huang, B., Bergan, J., Dulac, C. and Zhuang, X. (2010) 'Superresolution imaging of chemical synapses in the brain', *Neuron,* 68(5), pp. 843-56.

Durisic, N., Laparra-Cuervo, L., Sandoval-Álvarez, A., Borbely, J. S. and Lakadamyali, M. (2014) 'Single-molecule evaluation of fluorescent protein photoactivation efficiency using an in vivo nanotemplate', *Nat Methods*.

Gunzenhäuser, J., Olivier, N., Pengo, T. and Manley, S. (2012) 'Quantitative super-resolution imaging reveals protein stoichiometry and nanoscale morphology of assembling HIV-Gag virions', *Nano Lett,* 12(9), pp. 4705-10.

Hell, S. W. (2007) 'Far-field optical nanoscopy', *Science,* 316.

Huang, B., Babcock, H. and Zhuang, X. (2010) 'Breaking the diffraction barrier: super-resolution imaging of cells', *Cell,* 143(7), pp. 1047-58.

Lando, D., Endesfelder, U., Berger, H., Subramanian, L., Dunne, P. D., McColl, J., Klenerman, D., Carr, A. M., Sauer, M., Allshire, R. C., Heilemann, M. and Laue, E. D. (2012) 'Quantitative single-molecule microscopy reveals that CENP-A(Cnp1) deposition occurs during G2 in fission yeast', *Open Biol,* 2(7), pp. 120078.

Lee, S. H., Shin, J. Y., Lee, A. and Bustamante, C. (2012) 'Counting single photoactivatable fluorescent molecules by photoactivated localization microscopy (PALM)', *Proc Natl Acad Sci U S A,* 109(43), pp. 17436-41.

Lehmann, M., Rocha, S., Mangeat, B., Blanchet, F., Uji, I. H., Hofkens, J. and Piguet, V. (2011) 'Quantitative multicolor super-resolution microscopy reveals tetherin HIV-1 interaction', *PLoS Pathog,* 7.

Lippincott-Schwartz, J. and Patterson, G. H. (2009) 'Photoactivatable fluorescent proteins for diffraction-limited and super-resolution imaging', *Trends Cell Biol,* 19(11), pp. 555-65.

Nair, D., Hosy, E., Petersen, J. D., Constals, A., Giannone, G., Choquet, D. and Sibarita, J. B. (2013) 'Super-resolution imaging reveals that AMPA receptors inside synapses are dynamically organized in nanodomains regulated by PSD95', *J Neurosci,* 33(32), pp. 13204-24.

Nan, X., Collisson, E. A., Lewis, S., Huang, J., Tamguney, T. M., Liphardt, J. T., McCormick, F., Gray, J. W. and Chu, S. (2013) 'Single-molecule superresolution imaging allows quantitative analysis of RAF multimer formation and signaling', *Proc Natl Acad Sci U S A,* 110(46), pp. 18519-24.

Puchner, E. M., Walter, J. M., Kasper, R., Huang, B. and Lim, W. A. (2013) 'Counting molecules in single organelles with superresolution microscopy allows

tracking of the endosome maturation trajectory', *Proc Natl Acad Sci U S A,* 110(40), pp. 16015-20.

Renz, M., Daniels, B. R., Vámosi, G., Arias, I. M. and Lippincott-Schwartz, J. (2012) 'Plasticity of the asialoglycoprotein receptor deciphered by ensemble FRET imaging and single-molecule counting PALM imaging', *Proc Natl Acad Sci U S A,* 109(44), pp. E2989-97.

Scarselli, M., Annibale, P. and Radenovic, A. (2012) 'Cell Type-specific beta 2-Adrenergic Receptor Clusters Identified Using Photoactivated Localization Microscopy Are Not Lipid Raft Related, but Depend on Actin Cytoskeleton Integrity', *J Biol Chem,* 287.

Sengupta, P., Jovanovic-Talisman, T. and Lippincott-Schwartz, J. (2013) 'Quantifying spatial organization in point-localization superresolution images using pair correlation analysis', *Nat Protoc,* 8(2), pp. 345-54.

Specht, C. G., Izeddin, I., Rodriguez, P. C., El Beheiry, M., Rostaing, P., Darzacq, X., Dahan, M. and Triller, A. (2013) 'Quantitative nanoscopy of inhibitory synapses: counting gephyrin molecules and receptor binding sites', *Neuron,* 79(2), pp. 308-21.

Testa, I., Urban, Nicolai T., Jakobs, S., Eggeling, C., Willig, Katrin I. and Hell, Stefan W. (2012) 'Nanoscopy of Living Brain Slices with Low Light Levels', *Neuron,* 75(6), pp. 992-1000.

Urban, Nicolai T., Willig, Katrin I., Hell, Stefan W. and Nägerl, U. V. (2011) 'STED Nanoscopy of Actin Dynamics in Synapses Deep Inside Living Brain Slices', *Biophysical Journal,* 101(5), pp. 1277-1284.

Xu, K., Zhong, G. and Zhuang, X. (2013) 'Actin, spectrin, and associated proteins form a periodic cytoskeletal structure in axons', *Science,* 339(6118), pp. 452-6.

Zanacchi, F. C., Manzo, C., Alvarez, A. S., Derr, N. D., Garcia-Parajo, M. F. and Lakadamyali, M. (2017) 'A DNA origami platform for quantifying protein copy number in super-resolution', *Nature Methods,* 14, pp. 789.

List of Publications

Durisic, N., Laparra-Cuervo, L., Sandoval-Álvarez, A., Borbely, J. S. and Lakadamyali., M. 2014. "Single-molecule evaluation of fluorescent protein photoactivation efficiency using an in vivo nanotemplate." Nat Methods. doi: 10.1038/nmeth.2784.

Durisic, N., Laparra Cuervo, L. and Lakadamyali., M. 2014. "Quantitative super-resolution microscopy: pitfalls and strategies for image analysis." Curr Opin Chem Biol 20C:22-28. doi: 10.1016/j.cbpa.2014.04.005.

Gaitán-Peñas, H., Gradogna, A., Laparra-Cuervo, L., Solsona, C., Fernández-Dueñas, V., Barrallo-Gimeno, A., Ciruela, F., Lakadamyali, M., Pusch, M. and Estévez., R. 2016. "Investigation of LRRC8-Mediated Volume-Regulated Anion Currents in Xenopus Oocytes." Biophys J 111 (7):1429-1443. doi: 10.1016/j.bpj.2016.08.030.

Ladépêche, L., Planagumà, J., Thakur, S., Suárez, I., Hara, M., Borbely, J.S., Sandoval, A., Laparra-Cuervo, L., Dalmau, J. and Lakadamyali, M. “Anti-NMDA receptor encephalitis antibodies lead to a subunit specific nanoscale redistribution of NMDA receptors.” Cell Reports. Under review.

Laparra-Cuervo, L., Ladépêche, L., Planagumà, J., Borbely, J.S., Sandoval, A., Dalmau, J. and Lakadamyali, M. “Multi-color STORM in neurons reveals molecular organization of the LGI1 synaptic complex”. Under preparation.

List of Figures